UNIVERSIDADE DE LISBOA
FACULDADE DE CIÊNCIAS
DEPARTAMENTO DE FÍSICA

Comparison of Two ^{177}Lu-DOTATATE Quantification Methods for Patient Personalized Dosimetry in Therapy of Neuroendocrine Tumors

Cristiana Magalhães Correia Rodrigues

Mestrado Integrado em Engenharia Biomédica e Biofísica
Perfil em Radiações em Diagnóstico e Terapia

Dissertação orientada por:
Dr. Paulo Ferreira
Prof. Dr. Luís Peralta

2021

Aknowlegments

Upon the conclusion of my master's dissertation, I would like to express my gratitude to everybody that, directly or indirectly, contributed for me to reach this moment.

First, I want to express my deepest appreciation to my supervisors for their valuable advice and constant belief in my abilities. I am deeply grateful to Dr. Paulo Ferreira, for giving me the freedom to define my every step during this project, sharing his extensive knowledge and for the encouragement during these 9 months. A profound thanks to Prof. Dr. Luís Peralta for the guidance, motivation and support throughout this project, and for being always available to answer even the most senseless questions.

A word of gratitude to Prof. Dr. Durval Costa and Prof. Dr. Francisco Oliveira for the great opportunity of doing the internship at the Nuclear Medicine – Radiopharmacology (NM-Rf) Department at the Champalimaud Centre for the Unknown, Champalimaud Foundation. Thank you for all the insightful suggestions and constructive criticism provided throughout the project.

I also wish to give a special thanks to the nuclear medicine physicians, Dr. Ângelo Silva, without whom this study would not be possible, Dr. Carla Oliveira, Dr. Sofia Vaz and Dr. Joana Castanheira, for generously welcoming and sharing their work space with me.

I must also extend my gratitude to the technical team and medical collaborators of the Department. In particular, thank you Marisa Machado, Juliana Correia and Sónia Teixeira for, during this pandemic, giving your time to help me with the experiments. Also, thank you Rui Parafita and Mauro Costa for helping me whenever I needed, for giving your invaluable insight about the work and letting me join you on lunch breaks.

The completion of my dissertation would have not been possible without Filipe, who took the time to help me learn a new coding language and overcome endless obstacles. Thank you for the immensurable patience, for reading and commenting every single sentence that I wrote and for always being there when I needed the most.

Finally, I cannot begin to express my gratitude to my family, my parents, grandparents and little sisters, for the unwavering great emotional support, encouragement, for their love, patience and counsel. Thank you for believing in me during this 5-year journey. Meant more than you will ever know.

Abstract

Peptide receptor radionuclide therapy (PRRT) with ^{177}Lu-DOTATATE is remarkably effective in the treatment of neuroendocrine tumors (NETs) over-expressing somatostatin receptors. Besides potential renal and/or hematological toxicity, the significant response inter-patient variability requires individual treatment planning. Several methods have been used to quantify tissue absorbed dose. The aim of this study was to compare the dosimetry calculated by two computational methods on a retrospective analysis of ^{177}Lu-DOTATATE PRRT clinical cases. Furthermore, we investigated toxicity and the feasibility of pre-treatment dosimetry with ^{68}Ga-DOTANOC PET/CT scans to estimate the optimal radiation activity to each patient.

Twenty-four treatments from six patients with histologically confirmed inoperable and/or metastatic NETs over-expressing somatostatin receptors were analyzed (4 cycles/patient). A mean activity of 7.2 ± 0.5 GBq/cycle of ^{177}Lu-DOTATATE was injected, after which patients underwent acquisition of serial whole-body planar images, and abdominal SPECT and CT scans. After processing, pre- and post-therapeutic scans were used for patient-specific voxel-wise absorbed dose quantification. Dosimetry with pre-calculated voxel S-values (VSVs) was performed with an in-house program. Monte Carlo (MC) dosimetry was performed with TOPAS (Geant4) MC tool. Cumulative dose-volume histograms (cDVHs) were generated and mean absorbed dose was compared using the intraclass correlation coefficient (ICC) and relative difference (RD).

MC dosimetry entailed a simulation time of around 2 days/simulation while the VSV method took less than 1 minute/computation, in the same workstation. Good agreement (ICC > 0.80) was found for organ and NETs absorbed dose distribution obtained with both methods, with similar cDVHs. According to both post-treatment SPECT and pre-treatment PET data, the highest median RD of -3.6% (min = -25.6%, max = 3.8%) and -8.3% (-30.8%, 2.5%) were seen, respectively, for the bone marrow (ICC = 0.999) and spleen (ICC = 0.846). Differences are presumably due to patient morphology considerations in MC simulations. Patient-specific dosimetry revealed that in half of the patients the bone marrow was the absorbed dose limiting organ. Lastly, significant deviations, from -83.1% up to 358.5%, were found between the absorbed dose data estimated with the pre- and post-therapeutic scans, which are possibly related with the different kinetics and binding profile of the two tracers.

This study reveals identical patient-specific 3D absorbed dose distributions for both methods, in the abdominal region. Thus, the VSV approach appears to be a suitable option for routine clinical dosimetry in ^{177}Lu-DOTATATE PRRT patients, considering the short computation time and accuracy. Data suggests that half of the patients had a bone marrow absorbed dose superior to the maximum value recommended, which could have been avoided if personalized dosimetry had been performed for each cycle/treatment. However, we cannot conclude about the treatment efficacy if that reduction had been implemented. Unfortunately, results do not support the possibility of treatment planning with a pre-therapeutic ^{68}Ga-DOTANOC PET/CT scan. Despite the small patient cohort, we hope that our results contribute to the development of a standard dosimetry protocol for PRRT.

Key-words: Neuroendocrine Tumors, ^{177}Lu-DOTATATE PRRT, Internal Dosimetry, Monte Carlo, Voxel S-values.

Resumo

Tumores neuroendócrinos (NETs) são neoplasias heterogéneas bem diferenciadas que podem surgir em qualquer região do corpo, frequentemente no trato digestivo e pulmões, devido a uma elevada taxa de proliferação das células neuroendócrinas. Até recentemente, eram considerados raros. Contudo, dados atuais sugerem mais casos do que o previsto, com uma incidência crescente nas últimas décadas possivelmente associada a uma maior sensibilidade e diagnóstico precoce. A expressão aumentada dos recetores de somatostatina (SSTR) é uma característica particular de NETs metastáticos bem diferenciados, que permite o diagnóstico e terapia com análogos sintéticos de somatostatina (SSA). Atualmente existem várias terapêuticas disponíveis, porém, a taxa de sobrevivência não aumentou. Nos últimos anos, surgiu um grande interesse em *peptide receptor radionuclide therapy* (PRRT) para o tratamento de NETs inoperáveis e/ou metastáticos com expressão aumentada de SSTR. Esta terapêutica consiste na irradiação das células tumorais via ligação de um péptido (i.e., SSA) acoplado a um emissor-β aos SSTR. A abordagem atual com ^{177}Lu-DOTATATE provou ser eficaz em vários ensaios clínicos com regressão tumoral, alívio de sintomas e baixo perfil toxicológico. A natureza dual do ^{177}Lu torna-o um bom agente teranóstico, pois as partículas emitidas viabilizam a ação terapêutica (i.e., morte celular), enquanto que a emissão de fotões permite a obtenção de imagens da biodistribuição do radiofármaco. Apesar da eficácia desta terapêutica, a toxicidade renal e/ou hematológica é a maior preocupação descrita na literatura. Contrariamente ao que se verifica em radioterapia externa, em PRRT é geralmente administrada uma atividade fixa, o que resulta numa grande variabilidade na resposta dos doentes devido a diferenças na cinética do radiofármaco e biologia tumoral. Isto evidencia a necessidade do planeamento individual do tratamento, o que requer a quantificação da dose absorvida pelos tecidos. Contudo, a carência de avaliações dosimétricas após PRRT é uma questão que inclui várias instituições clínicas, principalmente devido à ausência de um protocolo de dosimetria padrão e ao elevado custo dos exames de imagem em medicina nuclear.

Vários métodos têm sido utilizados para quantificar a exposição dos tecidos à radiação ionizante. Dosimetria ao nível do vóxel permite a obtenção de mapas de dose 3D, considerando a distribuição não uniforme da atividade no corpo facultada por imagens funcionais (e.g., SPECT e PET). Atualmente, o cálculo de dose por simulações de Monte Carlo (MC) é considerado o mais preciso, ao permitir também a inclusão de informação morfológica do doente (i.e., características dos tecidos) fornecida por imagens estruturais (e.g., CT). Todavia, devido aos grandes recursos computacionais que exige, a implementação de técnicas de MC na rotina clínica permanece um desafio. O cálculo de dose com *voxel S-values* (VSV) pré-calculados é uma alternativa computacionalmente muito mais rápida. No entanto, a sua aplicação pressupõe a uniformidade do tecido da região irradiada, o que poderá comprometer a sua precisão. Assim, ao longo dos últimos anos tem sido discutido qual será a abordagem dosimétrica mais adequada a nível de recursos e precisão para ser implementada na prática clínica. O objetivo principal deste projeto foi comparar a dosimetria calculada por dois métodos computacionais, VSV versus MC, numa análise retrospetiva de casos clínicos de PRRT com ^{177}Lu-DOTATATE. Ainda, foi investigada a potencial ocorrência de toxicidade bem como a viabilidade de dosimetria pré-tratamento com imagens PET/CT de ^{68}Ga-DOTANOC.

Foram analisados, retrospetivamente, vinte e quatro tratamentos de seis doentes diagnosticados com NETs metastáticos e/ou inoperáveis com expressão aumentada de SSTR (4 ciclos/doente). Após a administração de 7.2 ± 0.5 GBq/ciclo de ^{177}Lu-DOTATATE, os doentes realizaram aquisição de imagens planares de corpo inteiro, e imagens SPECT e CT da região abdominal. As imagens SPECT

foram reconstruídas e corrigidas para a atenuação e dispersão dos fotões, resposta do colimador e tempo morto do detetor. As imagens SPECT processadas, originalmente em contagens por vóxel, foram convertidas para atividade usando um fator de calibração previamente determinado. Nenhuma correção foi aplicada às imagens planares. A distribuição da atividade no corpo dos doentes e a retenção do radiofármaco foram estudadas utilizando informação quantitativa dada pela série de imagens planares. Dosimetria serviu-se apenas das imagens SPECT e PET. O cálculo de dose com VSV pré-calculados foi efetuado usando uma rotina dedicada, sob o pressuposto de meio uniforme. Esta abordagem consiste na convolução do *kernel* dos VSV do ^{177}Lu, calculados para vóxeis cúbicos de 2.21 mm de tecido mole, com a distribuição da atividade acumulada determinada com base nas imagens SPECT ou PET. Simulações de MC foram realizadas com o *software* TOPAS (Geant4) MC, utilizando 100 milhões de eventos (i.e., decaimentos). Até à data, não se identificaram estudos que reportassem o uso do TOPAS-MC para dosimetria em terapias com radionuclídeos. A dose absorvida média no fígado, rins, baço, medula óssea e tumores foi determinada para ambos os métodos e comparada, tomando o MC como referência. Adicionalmente, histogramas dose-volume cumulativos (cDVHs) foram gerados para se estudar a uniformidade da deposição da dose em cada região. A estimação da dose absorvida com base nas imagens pré-terapêuticas PET/CT de ^{68}Ga-DOTANOC foi efetuada considerando nas simulações de MC o ^{177}Lu como o radionuclídeo emissor e na convolução utilizando os respetivos VSV. Analogamente, a dose absorvida média nos órgãos e NETs foi investigada e comparada com o valor real obtido após o primeiro ciclo de PRRT.

As simulações de MC levaram cerca de 2 dias/simulação enquanto que o método VSV levou menos de 1 minuto/cálculo, no mesmo equipamento. As distribuições de dose absorvida nos órgãos e NETs obtidas com ambos os métodos, utilizando as imagens SPECT pós-terapêuticas, apresentaram uma boa concordância em regiões com pequenas variações de densidade (ICC > 0.90), apresentando uma distribuição muito idêntica dada pelos cDVHs. A maior diferença relativa de -25.6% foi registada para a medula óssea (ICC = 0.999), possivelmente devido à inclusão de informação morfológica do doente nas simulações. Contudo, não se verificaram diferenças significativas entre os dois métodos para os órgãos e NETs estudados. Resultados semelhantes foram obtidos com as imagens PET pré-terapêuticas, com diferenças negligiveis. No entanto, a maior diferença relativa de -30.8% foi observada para o baço (ICC = 0.846). Ainda, os dados demostraram que, em metade dos doentes, a medula óssea foi o órgão limitador da dose absorvida, com valores a exceder o máximo recomendado de 2 Gy no final do tratamento. Relativamente à dosimetria pré-tratamento, contrariamente ao previsto, a dose absorvida média exibiu diferenças estatisticamente significativas em todos os órgãos e NETs, desde -83.1% até 358.5%, entre ^{177}Lu-DOTATATE e ^{68}Ga-DOTANOC, com exceção do fígado e medula óssea. Estas discrepâncias poderão estar relacionadas com um diferente perfil biocinético dos radiofármacos e com a limitação de ter sido utilizada apenas uma imagem pré-tratamento para o cálculo de dose absorvida.

Em geral, os dois métodos de dosimetria implementados produziram mapas de dose absorvida muito semelhantes na região abdominal, com o método da convolução a exibir valores ligeiramente inferiores ao MC. Assim, o método VSV aparenta ser uma escolha adequada para dosimetria clínica em doentes submetidos a PRRT com ^{177}Lu-DOTATATE, atendendo ao reduzido tempo de cálculo e precisão das estimativas. Ainda, considerando apenas a dose máxima recomendada para os órgãos críticos, é possível concluir que em metade dos doentes a atividade injetada foi superior ao desejado, o que poderia ter sido evitado se dosimetria personalizada fosse realizada para cada ciclo/tratamento. Contudo, nada se pode concluir sobre a possível perda de eficácia do tratamento. Por fim, os resultados indicam que o planeamento dosimétrico do tratamento com imagens PET/CT de ^{68}Ga-DOTANOC não é adequado pois não se identificou qualquer correlação entre a distribuição de dose absorvida determinada com as imagens pré- e pós-terapêuticas. Não obstante, acredita-se que este estudo proporcionou um maior entendimento nesta área. Apesar do reduzido número de doentes estudados e das limitações existentes,

espera-se que este trabalho reforce a importância da dosimetria em terapias com radionuclídeos e auxilie o desenvolvimento futuro de um protocolo de dosimetria padrão para PRRT.

Palavras-Chave: Tumores Neuroendócrinos, ^{177}Lu-DOTATATE PRRT, Internal Dosimetry, Monte Carlo, Voxel S-values.

List of Contents

List of Figures

List of Tables

List of Acronyms

2D	Two-Dimensional
3D	Three-Dimensional
CCC	Champalimaud Clinical Centre
CDR	Collimator-Detector Response
cDVH	cumulative Dose-Volume Histogram
CF	Calibration Factor
DNA	Desoxyribonucleic Acid
cps	counts per second
CT	Computed Tomography
DEW	Dual-Energy Window
DICOM	Digital Imaging and Communications in Medicine
EANM	European Association of Nuclear Medicine
EBRT	External Beam Radiation Therapy
EC	Electron Capture
EMA	European Medicines Agency
ENSDF	Evaluated Nuclear Structure Data File
FDA	Food and Drug Administration
FOV	Field-of-View
HU	Hounsfield Units
IA	Injected Activity
IAEA	International Atomic Energy Agency
ICC	Intraclass Correlation Coefficient
ICRP	Internal Commission on Radiological Protection
ICRU	International Commission on Radiation Units and Measurements
IQ	Interquartile
MC	Monte Carlo
MEGP	Medium Energy General Purpose
MIRD	Medical Internal Radiation Dose
MRI	Magnetic Resonance Imaging

NCA	No Carrier Added
NEMA	National Electrical Manufacturers Association
NET	Neuroendocrine Tumor
NIFTI	Neuroimaging Informatics Technology Initiative
NM	Nuclear Medicine
OSEM	Ordered-Subset Expectation Maximization
PET	Positron Emission Tomography
PI	Post-Injection
PIXE	Particle Induced X-ray Emission
PMT	Photomultiplier Tube
PRRT	Peptide Receptor Radionuclide Therapy
PVE	Partial Volume Effect
RD	Relative Difference
ROI	Region of Interest
SD	Standard Deviation
SEER	Surveillance, Epidemiology and End Results
SI	International System of Units
SNMMI	Society of Nuclear Medicine and Molecular Imaging
SPECT	Single-Photon Emission Computed Tomography
SSA	Synthetic Somatostatin Analogue
SSTR	Somatostatin Receptors
SUV	Standardized Uptake Value
TAC	Time-Activity Curve
TEW	Triple Energy Window
TOPAS	TOol for PArticle Simulation
TRT	Targeted Radionuclide Therapy
VOI	Volume of Interest
VSV	Voxel S-value
WB	Whole-body
XCAT	Extended Cardiac-Torso

Chapter 1

Introduction

In this chapter, a brief overview on the background of this dissertation is presented as well as the motivation behind the project. Additionally, the main goals are described and the outline of the document's structure closes the chapter.

1.1. Background

Ionizing radiation has been effectively used in medicine for over 100 years. The use of radionuclides for the treatment of several medical conditions is not a novelty, as their ability to induce apoptosis (i.e., programmed cell death) is well known. The interaction of radiation with the cells activates different pathways that lead to substantial DNA (i.e., desoxyribonucleic acid) damage. Remarkable advances have been made in the field of radionuclide therapies, particularly in their usage for cancer treatments. Around 75 years ago, the first reports of successful therapies with Iodine-131 (^{131}I) for thyroid carcinomas emerged [1]. This was one of the most promising developments in nuclear medicine (NM), called targeted radionuclide therapy (TRT). The concept was first envisioned over a century ago by Paul Ehrlich, who was awarded the Nobel Prize of Medicine in 1908. The aim was to use an agent to treat a specific condition without harming the body [2]. Over time, this notion evolved and was applied to cancer therapy, by means of a molecular carrier (e.g., monoclonal antibody or peptide), labelled with a radionuclide, to specifically target neoplastic cells. This minimizes irradiation of normal tissues, thereby presenting fewer side-effects than conventional external beam radiotherapy (EBRT) [3]. Currently, TRT is a very promising tool for the treatment of metastatic and primary cancers.

In ancient Roman religion, Janus was the god of change and was often depicted as having two faces looking in opposite ways, towards the future and past. Theranostics, a concept introduced for the first time in 1998 by John Funkhouser, defines the use of a single agent for diagnostic and therapy purposes. Therefore, it can be considered the Janus of modern medicine [4]. TRT offers the possibility to detect and treat tumors with specific biomarkers using isotopes with both particle and photon emissions. Peptide receptor radionuclide therapy (PRRT) is the most recent type of TRT that avails of this feature. Regarding the therapeutic action for cancer treatment, multiple advantages were found in the use of β-emitters (i.e., electron emitters), such as Yttrium-90 (^{90}Y) and Lutetium-177 (^{177}Lu), for being ionizing particles that enhance reactive oxygen species mediated DNA damage and direct DNA impairment [1]. Nowadays, α-emitters (i.e., two protons and two neutrons, identical to the nucleus of Helium-4) such as Bismuth-213 (^{213}Bi) and Actinium-225 (^{225}Ac) are emerging as potential useful radionuclides [4].

Several clinical trials [6][7] have shown the effectiveness of PRRT with ^{177}Lu-DOTATATE in the treatment of neuroendocrine tumors (NETs). However, bone marrow and kidney toxicity may represent a major limitation of this therapy. Unlike in EBRT, where patient-specific absorbed doses (i.e., mean energy imparted per unit mass) are routinely planned, using sophisticated treatment planning software and state-of-the-art imaging modalities, treatments in NM are often based on a fixed or weight-based

activity regimen [5]. The "one-size-fits-all" approach results in a significant inter-patient variability in absorbed dose, due to different tracer kinetics or receptor density in organs and tumors [8]. The European Council Directive 2013/59/EURATOM [9] states that an effort must be made to ensure that treatments result in maximum radiation absorption by tumor cells, sparing adjacent normal tissues. This requires absorbed dose quantification (i.e., dosimetry), which is not currently conducted in clinical routine at all institutions, mainly due to the absence of a standard dosimetry protocol for TRT, reliable dose thresholds for critical organs and great financial burden related with imaging studies [10]. In addition, dosimetry in TRT is performed according to information about the tracer kinetics, isotope, anatomical geometry, etc. Thus, values estimated from EBRT treatment planning cannot be directly applied to TRT [11].

Hence, there is an evident need to evaluate the absorbed dose after TRT, through individualized image-based dosimetry, to improve future treatment plans and avoid critical organ toxicity, through the modulation of treatment doses. The paradigm in internal dosimetry has been evolving over the years to find techniques that allow an increasingly accurate dose estimation. Multiple methods have been used to predict and quantify tissue exposure to ionizing radiation, each with its advantages and drawbacks. The main goal of this work was to investigate the patient-specific absorbed dose estimated by two computational methods to determine which is the most suitable for clinical applications to optimize treatment plans and personalize care. In this regard, using pre- and post-therapeutic 3D molecular scans, voxel S-values (VSVs) dosimetry and Monte Carlo (MC) simulations with TOPAS (Geant4) MC code were implemented to quantify the absorbed dose in ^{177}Lu-DOTATATE PRRT patients. To accomplish this goal, several secondary objectives were established:

a) Determination of the gamma camera's dead time, to account for count losses, and calibration factor (CF), used to convert the image's tracer uptake (i.e., counts) into activity values (i.e., Bq), for the specific single-photon emission computed tomography (SPECT) acquisition configuration used in ^{177}Lu-DOTATATE PRRT patient studies.

b) Biokinetic analysis (i.e., retention and effective half-life determination) of the tracer in the whole-body, critical organs and NETs using post-therapeutic planar imaging.

c) Computation of VSVs using TOPAS-MC and analysis of the influence of voxel size, tissue composition and particle's energy in the calculation.

In addition, we aimed to perform a retrospective analysis of the occurrence of possible toxicity and evaluate the potential of pre-treatment dosimetry with ^{68}Ga-DOTANOC positron emission tomography (PET)/computed tomography (CT) scans to estimate the optimal radiation activity to each patient.

1.2. Contributions of the Thesis

The preliminary results from this thesis were presented in the:

European Association of Nuclear Medicine (EANM'20) conference abstract (Appendix A): Rodrigues, C., Ferreira, P., Oliveira, F. P. M., Silva, Â., Peralta, L., Costa, D. C. (2020). ^{177}Lu-DOTATATE quantification for patient personalised dosimetry in therapy of neuroendocrine tumours. *Eur J Nucl Med Mol Imaging*, 47, S656.

European Association of Nuclear Medicine (EANM'21) conference abstract (Appendix B): Rodrigues, C., Ferreira, P., Oliveira, F. P. M., Silva, Â., Peralta, L., Costa, D. C. (2021). Comparison of Voxel S-values and Monte Carlo Simulation in [^{177}Lu]Lu-DOTA-TATE Quantification for Patient-Specific Dosimetry. *Eur J Nucl Med Mol Imaging*, 48, S75.

1.3. Thesis Outline

This dissertation comprises seven chapters that describe the work conducted at the NM-Rf Department of the Champalimaud Centre for the Unknown, Champalimaud Foundation, Lisbon. A brief description of each chapter is given below.

Chapter 2: Clinical Background

This chapter regards the clinical aspects of this work. The characteristics and incidence of NETs as well as a brief overview on the history of PRRT and current approaches, particularly focused on ^{177}Lu-DOTATATE, are discussed.

Chapter 3: Physical Background

In this chapter, the main physical concepts that were used in this project, namely radioactive decay and interactions of radiation with human tissues, are described. The major notions regarding the gamma camera's imaging acquisition system and the most significant issues related with quantitative imaging are discussed. In addition, an overview on the most commonly used internal dosimetry methods, with emphasis on the approaches that were implemented in this study, is also presented. A brief review of other work in this research area closes the chapter.

Chapter 4: Materials and Methodology

This chapter begins with a description of the therapy/imaging acquisition protocols used in the Champalimaud Clinical Centre (CCC) where the practical research work for this dissertation was conducted. A detailed explanation of the steps followed in a retrospective investigation of ^{177}Lu-DOTATATE PRRT patient studies is provided. Patient data was selected from the NM-Rf Department of the CCC. Image processing methods are reported as well as the phantom experiments that were conducted to determine correction factors for dead time and the system's CF. Moreover, the MC computation of specific VSVs for various radionuclides (^{177}Lu and ^{68}Ga), voxel sizes (2.21 and 4.42 cubic voxels) and tissues (soft tissue and bone) and their application for voxel-based dosimetry is depicted. Pre- and post-treatment VSV and MC dosimetry calculations using 3D patient-specific data are also thoroughly described.

Chapter 5: Results

This chapter reports the results obtained in this research study (i.e., data processing, quantification and dosimetry), following the methodology described in the previous chapter.

Chapter 6: Discussion

A detailed discussion of the findings of this study is given in this section. A thorough analysis of the influence of dead time in ^{177}Lu SPECT scans is presented. In addition, patient-specific biokinetic data collected from 2D scans, and the computed VSVs used in the absorbed dose calculation were compared with published data. The results of the comparative study between the dosimetry calculated with the VSV method and MC simulations are discussed as well as the occurrence of possible critical organ toxicity in the investigated patient cohort. Furthermore, the potential of pre-treatment dosimetry with ^{68}Ga-DOTANOC PET/CT scans is also debated. A brief listing of the limitations encountered in this project closes the chapter.

Chapter 7: Conclusion

In this chapter, the main conclusions drawn from this study are reported, as well as suggestions for future work in this field of research to improve the accuracy of patient-specific voxel-wise clinical dosimetry in ^{177}Lu-DOTATATE PRRT.

Appendix

This last chapter musters all additional data and results obtained in this project. Additional tables and figures that were not presented in the results section of this document can be found here.

Chapter 2

Clinical Background

In this chapter, the characteristics and current incidence of NETs in the world population are presented. A brief overview of the history and basic concepts (e.g., eligibility, pharmacokinetics) related with PRRT, particularly focused on ^{177}Lu-DOTATATE, are also provided.

2.1. Neuroendocrine Tumors

NETs are heterogeneous neoplasms that arise when hormone-producing cells present an abnormally high proliferation rate. They can appear anywhere in the body but are most frequent in the gastrointestinal tract (around 70%) and lungs (around 30%) [12][13] (Figure 2.1). Of all subtypes, gastroenteropancreatic NETs are one of the most common digestive system neoplasms, ranking second behind colorectal cancer [14]. For the rest of this document, no distinction will be made, and the general term NETs will be used to refer all neuroendocrine tumors.

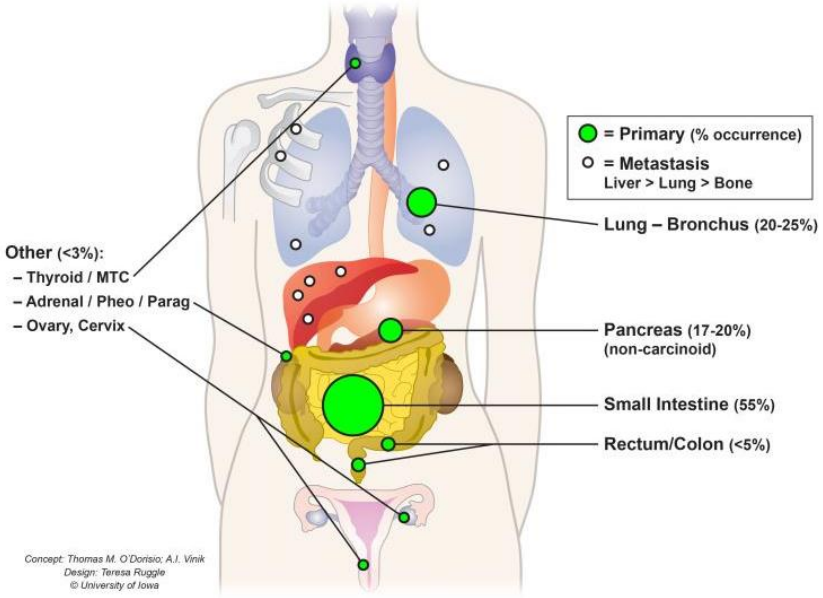

Figure 2.1. Typical anatomical distribution of NETs. Adapted from [15].

Until a few years ago, NETs were considered a group of rare tumors, representing approximately 0.5% of all newly diagnosed malignancies and 2% of all malignant conditions of the gastrointestinal tract [16]. However, current data suggests a higher prevalence than previously reported. The incidence of this condition has been increasing over the years, possibly due to increased awareness and early-stage detection, with a more than six-fold increase between 1973 to 2012 (Figure 2.2), according to the Surveillance, Epidemiology and End Results (SEER) cancer registry. In the United States, it is estimated that more than 170 000 people are currently living with the disease [17][16]. Recent studies

conducted in Western European and Asian countries also show an increasing incidence of NETs in the last few years [18]-[20].

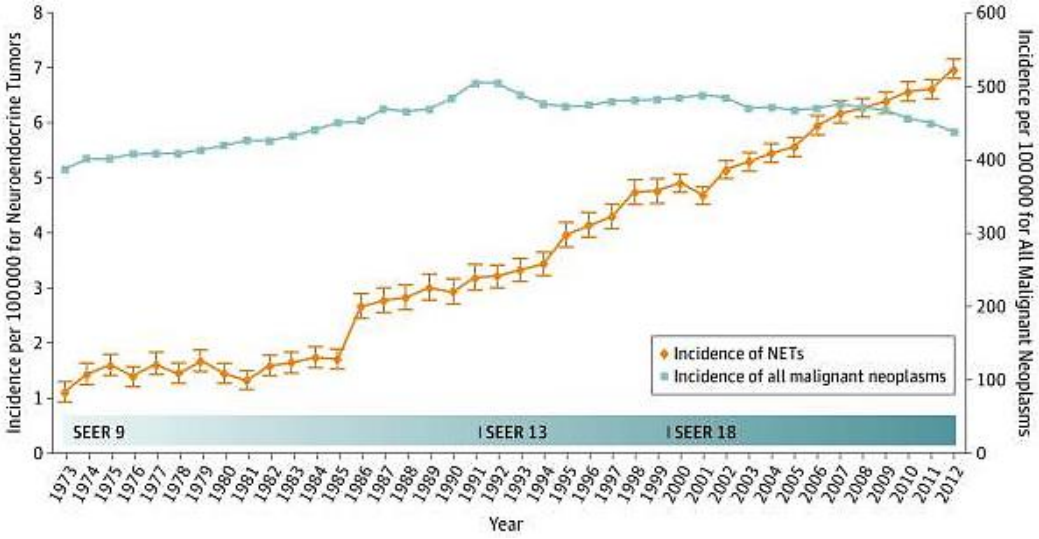

Figure 2.2. Incidence trend of NETs and all malignant neoplasms, from 1973 to 2012, according to the SEER cancer registry. The incidence of this condition has been increasing over the years with a rise from 1.09 to 6.98, per 100 000 people, in the considered period. Adapted from [17].

NETs are extremely heterogeneous regarding their molecular biology, clinical behavior and response to therapy [17]. Upon diagnosis, around 12% to 22% of patients exhibit metastases, more commonly found in the liver. NETs are categorized according to the mitotic index (i.e., measure of cellular proliferation and differentiation) into G1, G2 and G3 which are, respectively, well-, moderately- and poorly differentiated[1] tumors. Moreover, NETs are classified into functioning or non-functioning tumors [4][17]. Functioning NETs produce multiple hormones (e.g., insulin, gastrin, serotonin, etc.) and can, therefore, lead to carcinoid syndromes [6]. The overexpression of somatostatin receptors (SSTR) is a common feature of well-differentiated metastatic NETs (> 80%). Somatostatin is a neurotransmitter that inhibits cell proliferation and hormone secretion (e.g., growth hormone, thyroid stimulating hormone, insulin), whose function is mediated by the SSTR [12]. Currently, five subtypes of human SSTR have been identified, namely SSTR1 – SSTR5, which are expressed in different degrees by different tissues. However, SSTR2 and SSTR5 are overexpressed on the cell surface of most NETs [21]. This is the rationale behind the use of radiolabeled synthetic somatostatin analogue (SSA)-based diagnosis and therapy of these tumors [22]. There are several treatments available, such as inteferon-α, cytotoxic chemotherapy, surgical intervention and PRRT [23]. Surgery is the only curative approach, but is not always feasible due to the advanced stage of the disease when detected [4]. Thus, due its reported great results, special attention is currently being given to PRRT. However, despite recent efforts, overall NETs survival has not improved [14].

2.2. Peptide Receptor Radionuclide Therapy

The interest in PRRT has been increasing in the last decades, for the treatment of well-differentiated, metastatic and inoperable NETs, being an option for patients in whom conventional therapies (e.g., chemotherapy) have failed [24]. PRRT consists on the irradiation of target cells via direct binding of a peptide, combined with a β-emitter (i.e., electron emitter), to the SSTR overexpressed on the cell membrane of primary tumors and metastases [12]. Following cellular internalization of the tracer, the

[1] Well-differentiated cancer cells are similar to normal cells, with slower proliferation than poorly differentiated tumors.

interaction of the β-particles leads to desired cell death through DNA damage (see Section 3.6.1). The radiolabeled SSAs are administered systemically, with a fractional dose, and in sequential cycles. The most common radioisotopes in PRRT are ^{111}In, ^{90}Y and ^{177}Lu, which combined with SSAs proved to be an efficient therapy for NETs, with tumoral responses based on radiological assessments [25]. The peptides (i.e., SSAs) more commonly used are DOTATATE (DOTA,Tyr3-octreotate), DOTATOC (DOTA0,Tyr3-octreotide) and DOTANOC (DOTA,1-NaI(3)-octreotide), marked via DOTA chelator to the radionuclide to create a cancer specific radiopharmaceutical, also called tracer [24]. The different SSAs have different affinity to the known SSTR subtypes. Thus, their biokinetic profile depends on the SSTR subtype density in the target tissues. For instance, octreotate is a modified form of octreotide with enhanced affinity to SSTR2, which results in higher intra-tumoral absorbed dose when compared with other SSAs, and similar uptake in normal organs such as kidneys, spleen and liver [26].

^{111}In-DTPA-octreotide was the first tracer designed for PRRT in NETs. Since ^{111}In emits both Auger electrons and gamma (γ) photons (see Section 3.1), it was particularly interesting for theranostic purposes [27]. However, the first clinical experiences were conducted with ^{90}Y-DOTATOC [4]. Unlike ^{111}In, ^{90}Y is a pure β-emitter and imaging was performed using bremsstrahlung radiation or another γ-emitter radionuclide, such as ^{99m}Tc, which is not ideal [27]. The current PRRT approach using ^{177}Lu-DOTATATE, which is the focus of this thesis, seems promising, with a higher survival rate and rarely exhibiting side effects compared to other isotopes [25].

2.2.1. Eligibility

Accurate diagnosis of the primary tumor and extent of the disease is essential for deciding which therapeutic approach is more suitable. Until a few years ago, this evaluation was performed using conventional imaging modalities such as CT and magnetic resonance image (MRI), which offer exceptional anatomical information. However, NETs are typically small and go often unnoticed in these scans [8][28]. Nowadays, diagnosis and patient's eligibility to PRRT are usually evaluated through ^{68}Ga-DOTA-peptide PET scans (Figure 2.3).

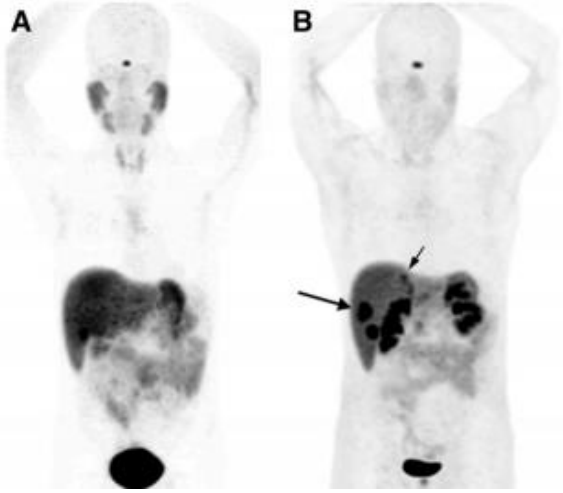

Figure 2.3. Typical whole-body ^{68}Ga-DOTATATE (A) and ^{68}Ga-DOTANOC (B) PET scans used to assess the eligibility of a patient to PRRT. ^{68}Ga-DOTANOC PET scan shows focused lesions in right liver lobe, which are not so evident in the ^{68}Ga-DOTATATE PET scans. Adapted from [29].

Among all ^{68}Ga-labeled peptides, ^{68}Ga-DOTANOC has proved to be more successful in detecting and staging both primary and well-differentiated metastatic NETs, with lower organ absorbed dose, due to its broader SSTR subtype affinity (i.e., it primarily targets SSTR2, SSTR3 and SSTR5) [30][31].

2.2.2. Lutathera®

Around four years ago, ^{177}Lu-DOTATATE (Lutathera®, Advanced Accelerator Applications, France) was approved by the Food and Drugs Administration (FDA) and European Medicines Agency (EMA) for the treatment of well-differentiated, inoperable and/or metastatic NETs of the midgut. This approval followed a considerable number of clinical trials that proved the efficacy of ^{177}Lu-DOTATATE [25][32]. One of the most significant studies was the phase III multicenter NETTER-1 clinical trial, whose results were recently published. It showed that ^{177}Lu-DOTATATE resulted in a higher overall survival, compared to SSAs-only therapy (octreotide long-acting repeatable), along with a higher response rate and significant improvement in life quality [6].

Biodistribution studies show that ^{177}Lu-DOTATATE has a rapid blood clearance of approximately 3.5 hours with fast uptake in the liver, kidneys, spleen, NETs and, in some patients, also in the pituitary and thyroid glands a few hours after injection. Since hematotoxicity can lead to myelosuppression, the bone marrow is considered a dose-limiting organ in PRRT. Moreover, according to the Erasmus and NETTER-1 studies around 60% of the compound is eliminated via urine (i.e., primary pathway of clearance) within 24 h, which can lead to nephrotoxicity due to proximal tubular reabsorption in the kidneys. Since this compound does not undergo significant hepatic metabolism, considering the physical half-life of ^{177}Lu, more than 95% of the drug will be eliminated within 30 days [32]. Therefore, the kidneys are also considered critical organs. The co-injection of positively charged amino acids has been found to reduce tubular reabsorption and mean absorbed dose to the kidneys by 47% [33]. Nonetheless, the use of ^{177}Lu revealed a low toxicological profile with a significantly lower risk of long-term nephrotoxicity when compared to ^{90}Y, without severe acute bone marrow toxicity with partial/complete responses and tumor regression [7][34].

2.2.3. Lutetium (^{177}Lu)

^{177}Lu has a physical half-life (see Section 3.1) of 6.647 days [35], a period long enough to ensure energy deposition in the tissues before biological elimination [36]. This radionuclide disintegrates via β^- decay (more information in Section 3.1.1) to three excited states of ^{177}Hf (Figure 2.4).

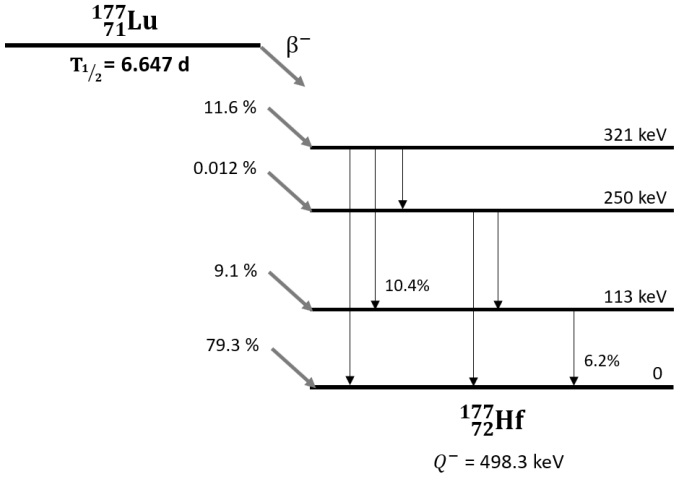

Figure 2.4. Simplified ^{177}Lu decay scheme. Adapted from [35].

The transition from the excited to the ground state occurs with the emission of six γ-photons (see Section 3.1.2). The two most abundant have energies of 112.9 (113 keV in Figure 2.4) and 208.4 keV (321 – 113 = 208 keV in Figure 2.4) with an emission probability of 6.2% and 10.4%, respectively. The most abundant β^--particles have a maximum kinetic energy of 177, 385 and 498 keV, with a probability

of 11.6%, 9.1% and 79.3%, respectively [22][35][37]. The mean kinetic energy of all β-particles, considering all transitions, is 134 keV (i.e., mean kinetic energy of the β-particles emitted in each decay times its probability). The emission of Auger and internal conversion electrons also occurs (see Section 3.2.1). When these are considered, the mean kinetic energy of the emitted particles rises to 147 keV [37]. The emission of Bremsstrahlung X-rays due to the interaction of β^--particles with tissues is also present (see Section 3.2.1).

The dual nature of ^{177}Lu renders it an excellent theranostic agent. From the imaging perspective, the abundance of photons is small. However, images of ^{177}Lu's biodistribution can be obtained via gamma camera imaging, enabling dose quantification. Additionally, the range of the β^--particles (see Section 3.2.1) emitted by ^{177}Lu is very short (Table 2.1), which allows better irradiation of small volumes with limited damage to adjacent normal tissues when compared to ^{90}Y, which provides uniform irradiation in a large tumor volume [12][38][39].

Table 2.1. Summary of physical properties of the radionuclides more commonly used in TRT of NETs. Mean and maximum particle range (R_β) are presented for soft tissue. Data from [35][40]-[42].

Radionuclide (PubChem CID)	**Half life (day)**	**Decay mode**	**Mean E_β (keV)**	**Max. E_β (keV)**	**E_γ (keV)**	**Mean R_β (mm)**	**Max. R_β (mm)**
^{68}Ga* (5488452)	0.047	β^+ EC	836.0	1899 (87.68%)	-----	-----	-----
^{90}Y** (104760)	2.668	β^-	926.7	2279 (99.98%)	None	3.9	11
^{177}Lu** (161046)	6.647	β^-	134	177 (11.6%), 385 (9.1%) 498 (79.3%)	112.9 (6.2%) **208.4** (10.4%)	0.27	1.7

* Diagnosis; ** Therapy
β = β-decay. EC = Electron Capture
Photopeak γ-energy typically used in imaging studies is indicated in boldface.

^{177}Lu can be produced in a nuclear reactor, by neutron activation, using two different methods: directly irradiating a ^{176}Lu sample with a high degree of purity (^{176}Lu(n,γ)^{177}Lu), or irradiating a ^{176}Yb sample, turning it into ^{177}Yb (half-life of 1.9 hours), which decays to ^{177}Lu. The latter approach is preferable since the product has no carrier added (NCA) and does not produce the long-lived isomer ^{177m}Lu (half-life of 160 days), which causes an issue of storage and disposal of radioactive waste. Furthermore, NCA ^{177}Lu requires lower levels of DOTATATE to label the required active amount of tracer for therapy [24][38][39][43].

Chapter 3

Physics and Instruments

This chapter begins with the description of the main physical concepts used in this work, namely radioactive decay and interactions of radiation (i.e., electrons and photons) with human body tissues, which are critical to understand the process behind the therapeutic action and NM imaging acquisition using radionuclides. Furthermore, major notions about the imaging acquisition system, namely hardware and image formation, are discussed as well as the most common issues related with quantitative SPECT studies. An overview on the most commonly used image-based internal dosimetry methods is also presented, particularly those implemented in this study. A brief review of other work related to quantitative PRRT assessments with ^{177}Lu-DOTATATE closes the chapter.

3.1. Radioactive Decay

Radioactive decay is a stochastic process governed by the laws of quantum physics [12][36]. It is characterized by the change of an unstable nucleus that may lead to a new stable daughter nuclide, with the emission of electromagnetic radiation [44], such as X-rays and γ-photons, and/or particles, such as electrons. The rate at which a decay process occurs is proportional to the number of radioactive nuclei, N, in the sample at a given time (t), and is given by

$$\frac{dN}{dt} = -\lambda N \tag{3.1}$$

where λ, is the decay probability of an unstable nucleus per unit time. For a sample with N radioactive nuclei at a time t, the quantity λN is called activity (A) and is expressed in Becquerel (Bq) [45]. A parameter commonly used to characterize the radioactive decay of a nucleus is the half-life, $T_{1/2}$, which is defined as the time required for half of the unstable nuclei to disintegrate (Eq. (3.2)) [44]. This parameter $T_{1/2}$ can be found by doing A/A0 = $e^{-\lambda t}$ = ½,

$$T_{1/2} = \frac{ln2}{\lambda}. \tag{3.2}$$

It is often introduced the concept of biological half-life, T_{bio}, which expresses the time required for half of the nuclei to be excreted only by physiological pathways (e.g., renal clearance, hepatic metabolism, bowel function) [36]. Hence, by depending of the pharmacokinetics of the isotope, the biological half-life can differ significantly between individuals. The effective half-life, T_{eff}, of the nuclide embodies both the physical and biological half-lives and is given by

$$\frac{1}{T_{ef}} = \frac{1}{T_{1/2}} + \frac{1}{T_{bio}}. \tag{3.3}$$

The most common decay processes are alpha, beta and gamma decays, each with its particular features. Since this work was focused on the ^{177}Lu and ^{68}Ga nuclides, only the β- and γ-decays will be addressed.

3.1.1. β-decay

The β-decay is a weak process characterized by the disintegration of an unstable nuclei with excess neutrons or protons, with the emission of β-particles (i.e., β^- or electrons and β^+ or positrons). In the case of β^--decay, a neutron is converted into a proton resulting in the simultaneous emission of an electron and an anti-neutrino which share the energy released in the reaction,

$$ {}^{A}_{Z}X \longrightarrow {}^{A}_{Z+1}Y + e^- + \bar{\nu}\,. \tag{3.4} $$

In the case of β^+-decay, a proton of the parent nucleus is converted into a neutron, resulting in the emission of a positron and a neutrino [45],

$$ {}^{A}_{Z}X \longrightarrow {}^{A}_{Z-1}Y + e^+ + \nu\,. \tag{3.5} $$

Within a small period of time, the positron will encounter an electron, and both will be annihilated. From this reaction, two γ-photons with an energy of 511 keV/photon are emitted in opposite directions [47]. In both processes, the emitted β-particles have a continuous kinetic energy spectrum that spans from zero to the maximum energy released in the decay.

Electron capture is an alternative process to the β^+-decay. The parent nucleus absorbs an inner shell electron to convert the proton into a neutron, and causes the simultaneous emission of a neutrino. The atomic vacancy is occupied by an electron from an outer shell, which results in the emission of characteristic X-rays or Auger electrons (see Section 3.2.1). Similar to the β^+-decay, the atomic number decreases by one unit and the atomic mass number remains unchanged [44][46].

3.1.2. γ-decay

When a nucleus is left in an excited state, following an α- or β-decay, the transition to the ground state or a lower energy state can occur, with the emission of gamma radiation with energy (almost) equal to the energy difference between the two nuclear states involved in the transition. The isomeric transition is a process that occurs when the excited nucleus state is long-lived (metastable) and is characterized by the emission of γ-photons and conversion electrons. When a nucleus deexcites via γ-decay, its atomic number and atomic mass number remain unchanged [45][46],

$$ {}^{A}_{Z}X^* \longrightarrow {}^{A}_{Z}X + \gamma\,. \tag{3.6} $$

The excited nucleus can also transfer its excess energy to an orbital electron, which is ejected. This is called internal conversion, an alternative process to the γ-decay. The ejected electron carries a well-defined kinetic energy distinctive from β-particles, which have a continuous energy spectrum [46].

3.2. Interaction of Radiation with Matter

There are several processes by which ionizing radiation can interact with matter. The most important for this particular work are the interactions of electrons/positrons and photons with the human tissues, which will be further discussed in the next sections.

3.2.1. Interaction of β-particles with Matter

When propagating in matter, β-particles gradually lose their kinetic energy due to interactions with atomic electrons in the medium [44]. A β-particle can collide with an orbital electron, transferring a fraction of its energy to that electron. When the transferred energy is greater than the electron's binding energy, it will be ejected and the vacancy, in an inner orbital (e.g., K-shell), will be occupied by an

outer layer electron (e.g., L-shell) with lower binding energy. The energy difference of this transition results in the emission of characteristic X-rays or Auger electrons (Figure 3.1, panel (a)). This process is called ionization. Fast electrons produced by ionization that can create secondary ionizations are called δ-rays. Conversely, when the transferred energy causes the bound electron to rise to an excited state, the process is known as excitation (Figure 3.1, panel (b)) [12][44]. β-particles can also be decelerated and deflected from their original trajectory, due to the electric force exerted by a nucleus close to its path. The deceleration causes the loss of a fraction of the particle's energy, which results in the emission of bremsstrahlung X-ray radiation (Figure 3.1, panel (c)), with a continuous energy spectrum that can range from zero up to the maximum kinetic energy of the particle [45].

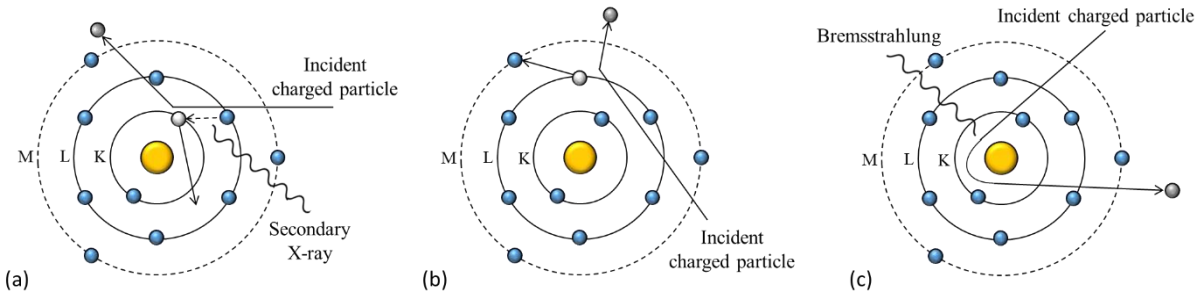

Figure 3.1. Schematic representation of the interactions of β-particles (or electrons) with matter: (a) ionization, (b) excitation and (c) bremsstrahlung. Adapted from [48].

The finite distance traveled by the particles (i.e., until they lose all kinetic energy) is called range. It depends on the initial energy of the particle and properties of the surrounding medium [44]. The total stopping power for electrons and positrons (i.e., energy lost per unit path length), due to these interactions has the contribution of two components, collisional and radiative (Eq. (3.7)). Ionization and excitation contribute as collisional energy losses, and bremsstrahlung as radiation energy losses.

$$\left(\frac{dE}{dx}\right)_{Tot} = \left(\frac{dE}{dx}\right)_{Rad} + \left(\frac{dE}{dx}\right)_{Col} \tag{3.7}$$

Radiation losses increase with the electron/positron energy and atomic number of the medium through which the particle travels. For the typical energies of the particles emitted by radionuclides used in cancer treatment, this component is a small fraction of the total energy loss [49].

3.2.2. Interaction of Photons with Matter

Unlike bremsstrahlung X-rays, characteristic X-rays and γ-rays emitted by atoms and nuclei are monoenergetic [44]. Photons emitted in the decay of ^{177}Lu interact with the medium mainly by three processes (Figure 3.2): Rayleigh scattering, photoelectric effect and Compton scattering.

In Rayleigh scattering, also known as coherent scattering, a photon interacts with an atom of the medium without ionizing or exciting it. The photon is scattered retaining its initial energy. This interaction has little importance for cancer treatment as no energy is transferred to the tissues [49][50]. However, it may impact imaging due to the photon deflection (see Section 3.4.1). This process is more probable for low photon energies [49].

In the photoelectric effect (Figure 3.3, panel (a)), an incident photon interacts with an atom of the medium. The photon transfers all its energy and is absorbed. As a result, the ejection of a photoelectron from one of its bound shells occurs and the atom is left in an excited state (i.e., the energy of the photon must be higher than the electron's binding energy). The vacancy is immediately occupied by an electron from an outer shell, with lower binding energy, leading to the emission of characteristic X-rays or Auger electrons that carry the atomic excitation energy. This process is dominant for low-energy photons [49].

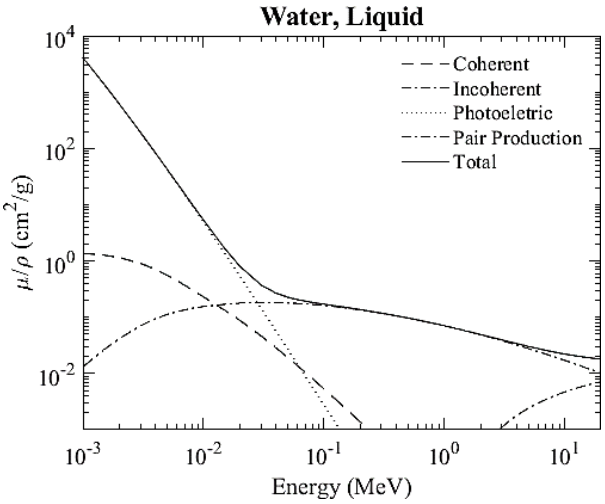

Figure 3.2. Partial (i.e., relative importance of coherent and incoherent scattering, photoelectric effect and pair production) and total mass attenuation coefficients of photons in water as functions of the energy. Adapted from [51].

Compton scattering (Figure 3.3, panel (b)) is characterized by the collision of a photon with an electron. From the collision results the ejection of the electron and a scattered photon with lower energy. The energy imparted to the electron can range from zero up to a large portion of the energy of the incident photon [50]. Compton scattering is dominant at intermediate energies and can also be associated with the emission of secondary particles, such as Auger electrons. At high energies, pair production is more likely to occur, in which the photon is converted into an electron-positron pair. This process requires that the photon energy exceeds twice the electron's mass [49], i.e., 1022 keV, which is what happens, for instance, in the radioactive decay of ^{90}Y. Since the photons emitted in the decay of ^{177}Lu do not meet this requirement, this interaction is not possible.

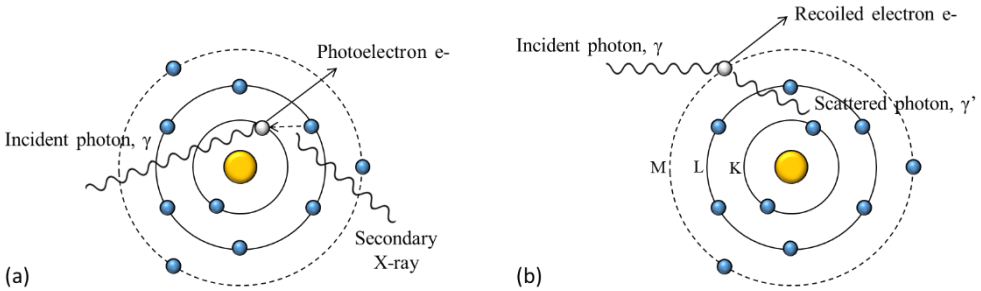

Figure 3.3. Schematic representation of the interactions of photons with matter, namely the (a) photoelectric effect and (b) Compton scattering. Adapted from [48].

All these interactions result in the attenuation and scattering of the photons as they travel through matter. Equation (3.8) translates the attenuation phenomenon, describing the exponential decrease in the beam's intensity, I (i.e., I_0 at the entrance of a tissue), on a material with thickness *x*,

$$I(x) = I_0 e^{-\mu x} \tag{3.8}$$

where μ is the attenuation coefficient. This coefficient depends on the beam's energy and the absorbing material properties (i.e., density). Tissues with higher density (i.e., higher atomic number) will cause a greater attenuation. Similarly, photons with higher energy will be less attenuated.

3.3. Gamma Camera Imaging

Common gamma cameras are equipped with two detector heads, which detect photons emitted from the source region in between them. This is described by a series of processes: collimation and photon

detection, conversion into an electrical pulse and signal amplification (Figure 3.4). The first task is performed by the collimators. These are usually lead structures with multiple holes designed to only allow the detection of photons within the angle of acceptance (i.e., travelling along the axis of each hole). Photons emitted in other directions are absorbed by the structures that separate the holes, called septa. Depending on their geometry, the collimators define the image's spatial resolution, that is, the ability to differentiate two adjacent points. The smaller the angle of acceptance, the higher is the image's resolution and detail. Contrary, collimators with larger holes allow the passage of more photons, leading to higher sensitivity at the cost of resolution. Collimators are also designed to filter the photons according to their energy. Thus, different collimators can be employed according to the radionuclide used in imaging. Photons that cross the collimator interact with and excite the scintillation crystal, typically made of sodium-iodine dopped with thallium. Upon relaxation, the crystal emits photons in the near ultraviolet and visible light range. These secondary photons are converted into photoelectrons (i.e., electrical signal) and are amplified by photomultiplier tubes (PMTs). PMTs closer to the interaction site generate the strongest electrical pulse as they receive a higher number of photons. The resulting electrical signal in each PMT is then processed by appropriate electronics and software to generate the final image of the radionuclide distribution [36][47][52], either planar, called scintigraphy (2D image), or tomographic (i.e., 3D image), called SPECT.

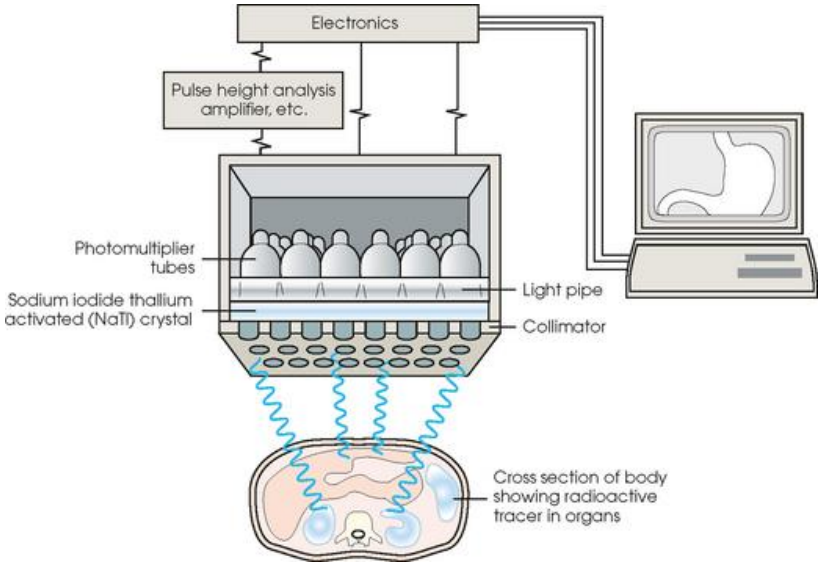

Figure 3.4. Typical disposition of a gamma camera system. Adapted from [53].

The configuration of a gamma camera for SPECT imaging is very similar to the one used in planar imaging, with the addition of a rotatable gantry that allows the motion of the camera heads around the patient. Multiple projections are acquired along several angular steps and are reconstructed to create a tomographic scan (i.e., a stack cross-sectional views). As planar imaging, SPECT relies on the use of γ-emitting radionuclides, such as ^{99m}Tc and ^{177}Lu [47][52]. Currently, images acquired with a gamma camera are not considered quantitative as they are reported in counts and not activity concentration, unlike PET scans. Furthermore, these scans suffer from multiple image degrading phenomena which hamper its direct use for quantification purposes.

3.4. Quantitative ^{177}Lu SPECT Imaging

In cancer imaging, although not trivial, quantification is particularly valuable to assess the therapeutic response and perform dosimetry calculations after radionuclide therapy [54]. Traditionally, SPECT has

been considered to be non-quantitative [55]. However, quantification using tomographic scans is thought to be superior to that with planar imaging as it does not encompass the issues related with organ overlap and provides more accurate information about non-uniform activity distribution [56]. As mentioned, ^{177}Lu decay has γ-emission which allows the acquisition of SPECT scans that, in turn, enable quantification. Physical interactions of photons with the tissues and limitations of the imaging system can contribute to image degradation and compromise quantification. Therefore, proper compensation for these factors is required. Since SPECT can be affected by several image degrading elements, only the most relevant for quantitative ^{177}Lu SPECT imaging will be briefly addressed, namely photon attenuation and scattering, bremsstrahlung, detector dead time, partial volume effect (PVE) and collimator-detector response (CDR). More information can be found in the paper by Bailey et al. [55].

3.4.1. Photon Attenuation and Scattering

The thickness of tissue-equivalent material required to reduce the kerma (i.e., kinetic energy released per unit mass) delivered by a 208 keV photon beam to half of its initial value at the entrance of the absorbing material (i.e., half value layer) is approximately 5 cm [37]. Thus, one of the most important factors to consider in ^{177}Lu imaging is photon attenuation in the tissues (Figure 3.5). When uncorrected, this results in an image with increased intensity in more superficial regions. Hybrid SPECT systems, by allowing the acquisition of both SPECT and CT images, enable the fast acquisition of a co-registered attenuation map, which complements SPECT data by providing information on tissue density [54][55].

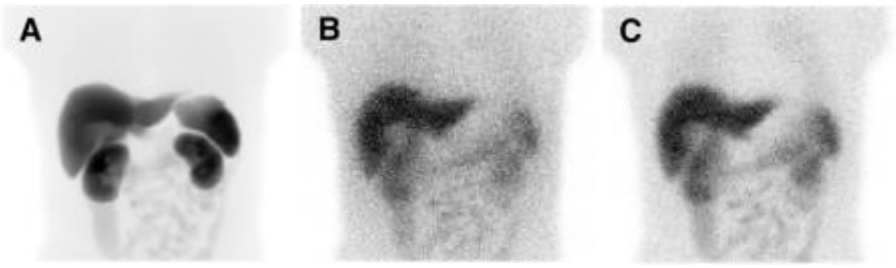

Figure 3.5. Simulated SPECT projections of an extended cardiac-torso (XCAT) phantom corresponding to the typical ^{177}Lu-DOTATATE biodistribution at 24 h post-injection. (A) Image simulated assuming ideal conditions: perfect spatial resolution, no scatter or attenuation in the phantom. This scan is representative of both 113 keV and 208 keV photopeaks. (B) and (C) panels show scans simulated using an energy window centered in the 113 keV and 208 keV photopeaks, respectively, including photon scatter and attenuation in the phantom as well as a realistic noise level. Adapted from [37].

Furthermore, photons that are not attenuated (i.e., by photoelectric interactions) can interact through Compton scattering, according to their energy (see Section 3.1). Deflected photons can be detected if their energy falls in the range of the selected energy window (i.e., downscatter). These lead to an overestimation of counts and contribute to a decreased image quality and resolution. Scatter correction in SPECT images is quite complex. There are some methods that are currently applied such as dual-energy window (DEW) and triple energy window (TEW) [57]. In recent years, major improvements have been made in this regard, including the incorporation of CT-based attenuation and scatter compensation in commercial software usually provided by the manufacturers of gamma cameras, that can be implemented during the iterative image reconstruction process [54].

3.4.2. Bremsstrahlung

Bremsstrahlung radiation produced by the interaction of the β^- particles of ^{177}Lu, although reduced, still contributes to the total absorbed dose in PRRT. For ^{177}Lu, the ratio between the detected bremsstrahlung and total number of emitted photons is 0.2%. This radiation is mostly attenuated inside the patient since 85% of these photons have energies below 50 keV. Therefore, the detection of bremsstrahlung radiation, unlike scattered photons, has no negative or significant effects in quantification [12]. Nevertheless,

some may contribute to the background counts registered in the low-energy portion of the ^{177}Lu spectrum and compensation is needed when using the 113 keV photopeak for imaging [37][58].

3.4.3. Dead Time

All electronic systems have some limitations regarding their performance. Due to the limited processing time of the gamma camera electronics, a poor photon detection occurs which results in a decreased image quality. This is particularly significant when high activities are used. After a certain number of photons reach the detector in a given time period, the system needs a recovery time (i.e., dead time) before the next pulse can be counted. Photons that reach the detector during this period are not processed [52]. Concerning this effect, most gamma cameras are described as paralyzable or non-paralyzable systems. In paralyzable systems any event that occurs during the recovery time is not counted and resets this period. In contrast, in non-paralyzable systems every event that occurs during the dead time period is not processed but does not add to the recovery time [49]. Therefore, dead time correction will depend on the system used. Moreover, in the so called "pileup effect", two or more photons reach the detector at approximately the same time and are counted as a single photon with an energy equal to the sum of the two incident photons. Thus, some signals will fall outside of the selected acquisition window, which leads to a decreased absolute count rate [59].

Unlike in conventional radionuclide imaging, where the effects of dead time can be significant, in ^{177}Lu imaging these are rather small, even when using high activities. This is mainly due to the very small bremsstrahlung contribution and low yield of γ-photons emitted in the decay. However, since the highest count rate in ^{177}Lu-DOTATATE PRRT is registered moments after the injection of the radiopharmaceutical, scans acquired shortly after injection will be the most affected by dead time losses. Hence, correction is necessary, particularly after therapy, when dosimetry is relevant, as it improves post-therapy imaging [37][54].

3.4.4. Partial Volume Effect

Another factor that impacts quantitative SPECT imaging is the PVE, a consequence of the limited spatial resolution and finite sampling of the imaging system. Structures with dimensions smaller than the spatial resolution will not have a well-defined shape and different tissues within the same voxel will not be distinguishable [36]. To quantify absorbed dose in the organs of interest in PRRT, their volumes are usually drawn from CT scans. However, due to the activity spill-out resulting from PVE, which causes activity blurring over a larger area than the actual source, quantification will be underestimated. Therefore, PVE compensation should be considered, particularly when assessing tumors with small dimensions. Currently, the most commonly used method to compensate PVE is the application of recovery coefficients derived from phantom experiments [37].

3.4.5. Collimator-Detector Response

In addition to septal penetration and scatter in the collimator, CDR also impairs the image's spatial resolution [37]. Photons emitted from a point-like source placed near the detector will pass through one or few collimator holes and generate a sharp signal when they reach the crystal (Figure 3.6). Contrary, point sources located further away emit photons that are within the angle of acceptance of several collimator holes. Since more photons will reach the detector, the signal will be broadened and the source will appear blurred in the image [52]. Therefore, the influence of CDR increases with source-to-detector distance. Most modern systems allow CDR compensation during the image reconstruction process. Besides improving spatial resolution, depth-dependent resolution recovery also changes noise texture (i.e., smoothing) and reduces the spill-out to some extent [37].

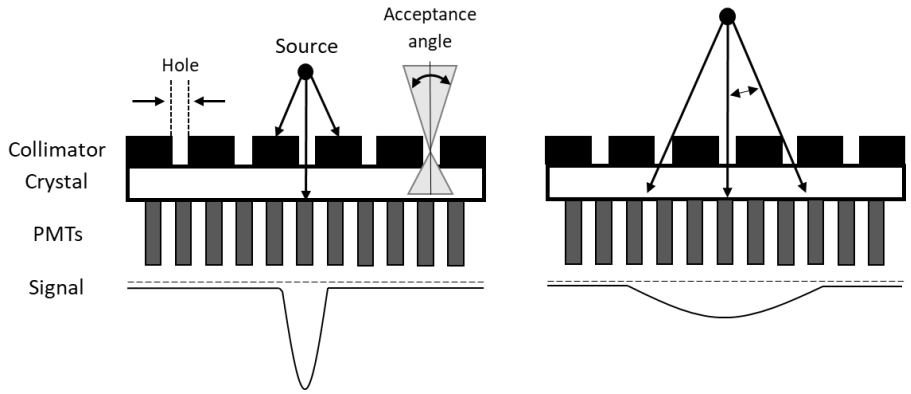

Figure 3.6. Schematic representation of the collimator-detector response effect. In the left, photons emitted from a point-like source near the detector pass through one collimator hole and generate a sharp signal. In the right, a point source further away from the detector emits photons that are within the angle of acceptance of several collimator holes, which results in a broadened signal. Adapted from [52].

The Medical Internal Radiation Dose Committee (MIRD) Pamphlets No. 23 [57] and No. 26 [37] provide guidelines for quantitative SPECT imaging, being the latter focused on ^{177}Lu quantification. However, these papers do not recommend unique or specific procedures, protocols or correction factors, such that different voxel counts can be encountered due to the use of different processing methods and not necessarily due to non-uniform tracer uptake [60]. Recently, optimization of acquisition parameters, iterative algorithms for image reconstruction, and sophisticated correction techniques have improved quantitative ^{177}Lu SPECT imaging for dosimetry assessments [22].

3.5. Quantitative ^{68}Ga-DOTA-peptide PET/CT Imaging

Nowadays, great interest has been taken in dosimetry prior to PRRT for treatment planning. Due to the high spatial resolution and quantitative nature, pre-therapeutic ^{68}Ga-DOTA-peptide PET/CT scans are very appealing for this purpose [61]. Despite the superiority of PET compared to SPECT, these scans suffer from the same image degrading phenomena previously mentioned. However, most contemporary PET scanners provide correction algorithms that can be easily applied during the image reconstruction process. Therefore, ^{68}Ga PET/CT scans enable the accurate tracer uptake quantification, expressed as standardized uptake values (SUVs), which can be used to assess response to therapy and treatment planning [62]. However, these are not the first choice for pre-treatment dosimetry due to the short half-life of ^{68}Ga compared to that of ^{177}Lu or ^{90}Y (see Table 2.1), which results in different pharmacokinetics [61]. Nonetheless, studies have investigated the possible correlation between the SUV of ^{68}Ga and the therapeutic counterpart. In fact, it has been reported that SSTR PET imaging could assist in the prediction of tumor absorbed dose after therapy and that higher SUVs were related with a higher positive response [63]. Moreover, when used for treatment planning in ^{177}Lu-DOTATATE PRRT, ^{68}Ga-DOTA-peptide PET scans are usually calibrated to the known injected activity of ^{177}Lu (i.e., the absolute values are not used, only the relative events distribution of ^{68}Ga) to estimate the tracer biodistribution after PRRT. However, there is lack of data regarding this application.

3.6. Internal Dosimetry

For over 50 years, absorbed dose assessments from common thyroid scans with radioactive iodine to prostate cancer treatments with radium have been of great concern to the scientific community and physicians [64]. The absorbed dose, which results from the interaction of ionizing radiation with matter, is defined as the mean energy, $d\varepsilon$, deposited per unit mass, dm,

$$D = \frac{d\varepsilon}{dm}. \tag{3.9}$$

In the Internal System of Units (SI), the absorbed dose is expressed in gray (Gy), which is equivalent to J/kg. Although not advised, the rad (1 rad = 0.01 Gy), a non-SI older unit, is still used to express the absorbed dose. This quantity is frequently used in radiation protection and radiology (e.g., cancer therapy) to quantify and control the harmful and beneficial effects of radiation.

3.6.1. Biological Effects of Radiation

The interaction of ionizing radiation with the tissues results in the deposition of energy that leads to substantial damage to the DNA structure [1]. Radiation induced DNA impairment can be due to direct or indirect action. In direct damage, the radiation interacts with the DNA itself. Indirect damage, by affecting the cell's molecular structure or non-structural contents, such as water (i.e., radiolysis), results in the creation of highly reactive free radicals that interact with and harm the DNA [65][66]. Both processes can cause changes in the DNA, which can lead to random mutations, or destroy its structure. When the DNA molecular structure is compromised, by single or double strand breaks, cellular repair mechanisms are stimulated. However, incorrect or incomplete damage repair can also lead to mutations. In addition, when the structural (i.e., chromosomal) damage is too severe, the cell becomes non-functional or expires [66]. Biological effects of radiation are divided in two categories: stochastic and deterministic effects. Stochastic effects are of probabilistic nature being, therefore, random and usually unpredictable. However, the likelihood of occurrence increases with the absorbed dose by the tissues and a dose interval can be given for a certain effect. The most common stochastic effects in the human population are cancer and heritable genetic mutations, that result from chronic exposure to low-dose radiation [65]. These effects are usually expressed years after exposure and their severity cannot be determined. In contrast, deterministic effects result from radiation induced unrepairable cell damage or extensive cell loss. These effects can manifest themselves within a few hours (e.g., skin injury) or years (e.g., cataracts) after exposure [66]. Determinist effects have a predictable nature and a causal relation with absorbed dose [65]. These are observable above a certain threshold and increase with absorbed dose [66]. Albeit commonly used to quantity tissue exposure to ionizing radiation, the absorbed dose does not describe the biological effects of the radiation in the tissues as it is only related to the physical process. Therefore, other quantities including biological effects like the equivalent and effective doses are often used to assess the potential radiation-induced risk of both effects in NM [67].

The European Directive 2013/59 EURATOM (Decree 108/2018) declares that treatments should be planned considering that irradiation of non-target tissues must be as low as reasonably achievable, while maintaining the radiotherapeutic purpose, to minimize undesirable effects in normal tissues [9][68]. Therefore, patient-specific dosimetry is paramount to optimize the treatment effectiveness and critical organ safety, as it allows the assessment of radiobiological effects. Multiple methods can be applied to estimate the absorbed dose in tissues, according to the situation and available resources. These have different levels of accuracy and can be differentiated depending on the level of detail of the patient-specific data [69][70]. In this work, only the most common dosimetry approaches will be mentioned.

3.6.2. Organ-Level Dosimetry

One of the most common methods of internal dosimetry currently applied in clinical routine to evaluate the absorbed dose in organs and tumors is based on simplified models, such as those derived by the MIRD formalism [71]. This schema was idealized by the Internal Dosimetry Committee of the United States Society of Nuclear Medicine and Molecular Imaging (SNMMI) and was later adopted by the International Commission on Radiological Protection (ICRP) and International Atomic Energy Agency

(IAEA) [72]. The traditional MIRD approach is based on organ-level dosimetry. It requires quantitative imaging at multiple time points post-injection to determine the accumulated activity (Ã) in an organ, which depends on the patient-specific tracer kinetics, and organ S-values, $S(r_T \leftarrow r_S)$. It is given by

$$D(r_T) = \sum_{r_{S'}} \tilde{A}(r_T)\, S(r_T \leftarrow r_{S'}) \tag{3.10}$$

where D stands for the mean absorbed dose in a target organ (r_T) due to irradiation from several source organs (r_S) (Figure 3.7). The accumulated activity is the total number of decays in the source that occur over a given time period and is determined as the integral of the tracer's time-activity curve (TAC). Organ specific S-values ($GyBq^{-1}s^{-1}$) represent the absorbed dose in a target organ per radioactive decay in the source organ. These contain information about the physical properties of the radionuclide as well as the distance and geometric relation between organs, being pre-calculated using standardized anthropomorphic phantoms [67][70]. The organ S-values are defined as

$$S(r_T \leftarrow r_S) = \sum_i \frac{n_i E_i \varphi_i(r_T \leftarrow r_S)}{m_T} \tag{3.11}$$

where m_T is the target's mass, n_i and E_i are the number of nuclear transitions and mean energy released for each radiation type *i* emitted per nuclear decay, respectively. $\varphi_i(r_T \leftarrow r_{S'})$ represents the absorbed fraction of energy emitted from the source organ and deposited in the target organ. Currently, the most commonly used organ S-values are available for specific organs and isotopes in software packages and free online databases, such as OpenDose [73] and RADAR [74].

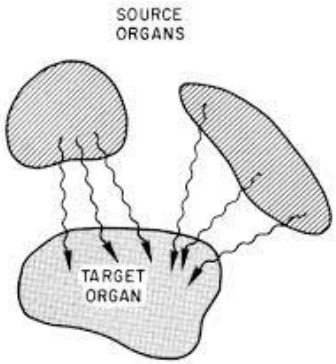

Figure 3.7. Schematic representation of the energy that is deposited in a target organ due to irradiation from several surrounding source organs. Adapted from [75].

The organ-level approach is not suitable for patient-specific dosimetry as it only allows to estimate the mean absorbed dose in a region and dismisses individual anatomical features, by assuming uniform activity distribution within an organ and relying on standard anatomical models [72][76]. The patient's organ mass can differ significantly from the phantom used for the calculation of S-values. Small variations in the anatomy can lead to significant differences in absorbed dose, not existing a standard model that can be used as reference for organ-level dosimetry studies [77]. Moreover, the absence of tumors in the model and the assumption of local deposition of β-radiation are other drawbacks. To account for these aspects, the MIRD formalism at the voxel level was proposed [71].

Other dosimetry approaches have emerged to help cope with the existing limitations and lead to more accurate absorbed dose estimates, as they have the potential to fully account for the patient-specific 3D features [70]. Voxel-based dosimetry, by providing 3D absorbed dose maps, allows treatment planning in terms of absorbed dose and volume constraints. Volumes of interest (VOIs) can be used to determine the mean absorbed dose in an organ or tumor [72]. Furthermore, unlike organ-level dosimetry, voxel-based dosimetry allows to obtain cumulative dose-volume histograms (cDVHs) and isodose lines, that

enable the study of non-uniform dose distribution within a tissue. Several computational methods are available, such as MC simulations and VSV dosimetry [71]. Although very different, both techniques account for the non-uniform activity distribution within the patient's body. In addition, the MC method also takes considers the heterogeneity (i.e., density) of organs and tumors, obtained by CT scans.

3.6.3. Monte Carlo Simulations

MC techniques are currently deemed the gold standard for internal dosimetry, since the simulations can perform full radiation transport (i.e., simulate all particle interactions), considering both non-uniform activity distribution and medium density. Using sophisticated mathematical models, MC simulations can reach a precision level not attainable by analytical methods [70][76]. Post-injection quantitative information regarding voxel-level activity distribution, provided by functional images, defines the emission probability distribution of the radiation source. A CT scan can be used to include patient-specific 3D information about the medium heterogeneity, scattering and attenuation behavior. Besides accounting for local energy deposition, MC simulations also consider the absorbed dose from cross-irradiation, which is particularly important when studying isotopes with γ-emission due to the longer path-length compared to α- and β-particles [78].

There are multiple MC codes currently available, such as EGS4 [79], MCNP [80], PENELOPE [81] and Geant4 [82]. Nowadays, Geant4, a software toolkit originally created for high energy physics applications, is considered by many the main reference of MC codes in the field of medical physics [83]. It is the most common choice for SPECT and PET areas, possibly due to its flexibility at describing complex geometries and accurate physics models [84]. However, Geant4 requires C++ programming skills, which restricts its manipulation to specialists. Attempts were made to bring the sophisticated and reliable tools of Geant4 into experimentally validated and intuitive MC codes, within the scope of every medical physicist. GATE [85], TOPAS [86], and GAMOS [87] are examples. Moreover, some codes that require extensive expertise to perform the simulations were incorporated into software packages, such as OLINDA/EXM [88], designed to allow a more user-friendly interface.

Several groups have applied MC techniques in the context of patient-personalized internal dosimetry and simulations in NM, using both patient data and modern computational phantoms. However, MC simulations are not free of limitations. This approach is not generally implemented in a clinical setting since it is computational demanding and time-consuming. The most common use of MC in PRRT is the validation of new faster algorithms for specific simplifications [78]. Nevertheless, this issue is being overcome by the modern technology, which allows fast data processing along with high performance computation [64]. Nowadays, research is being conducted to find the best compromise between accurate MC calculations and computational burden. In particular, force detection and variance reduction techniques are examples of methods developed to increase the simulation speed [89].

In this study, the TOPAS (TOol for PArticle Simulation) MC toolkit was used for internal dosimetry purposes. TOPAS is a breakthrough software project. Its primary goal was to implement accurate proton therapy simulations when no simple MC routines for clinical absorbed dose calculation existed in this medical field. By allowing the reduction of the uncertainty margin in treatment planning, this code became the benchmark for proton therapy. TOPAS' extension to radiobiology came years after its release in 2009. Recently, a brachytherapy module was included. TOPAS overcomes the issues related with the use of Geant4, by requiring little programming skills and providing great flexibility. All therapy features, such as geometry, particle source, fields, motion, scoring, graphical output and physical settings, are controlled by text-based parameter files (Figure 3.8).

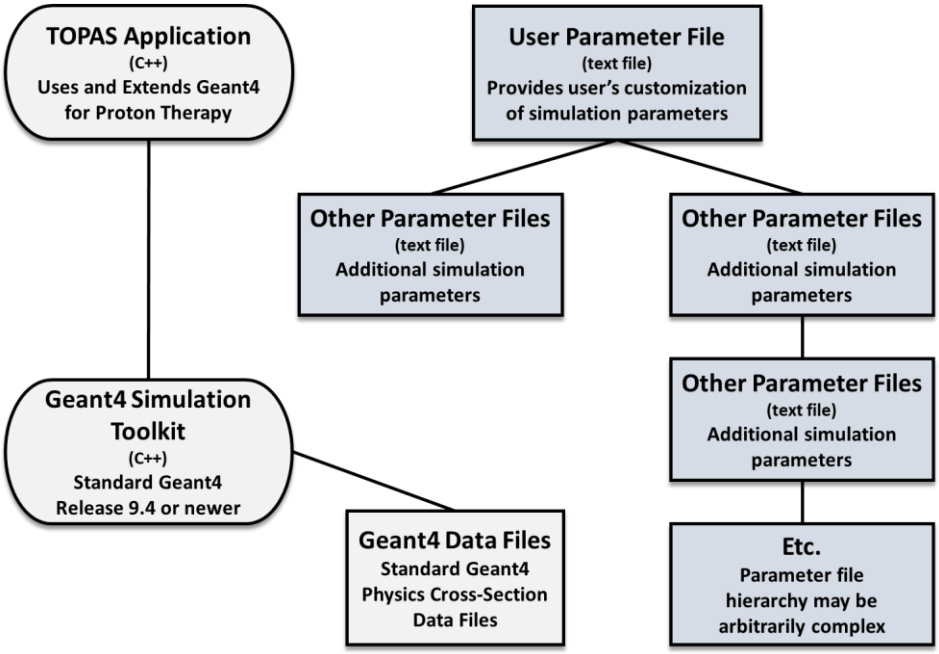

Figure 3.8. Overall operation of the TOPAS-MC code. Unlike Geant4 toolkit, which requires C++ programming experience, TOPAS uses a simple text file with the parameters to run the simulation. Adapted from [86].

The use of this toolkit, both in research centers and medical institutions, has been rapidly increasing as its advantages are recognized. As of September 2021, TOPAS counts with 1690 registered users at 498 institutions in 51 countries [86][90].

3.6.4. Voxel S-Value based Dosimetry

The VSV approach, the most common method to perform voxel-based dosimetry for therapeutic planning, follows the MIRD formalism [57], in which sources and targets are defined at the voxel-level. This is an analytical method where the 3D activity distribution, given by quantitative functional scans, is used to determine the absorbed dose. This calculation is performed through the convolution of pre-calculated VSVs with the patient-specific accumulated activity distribution (Eq. (3.12)) [12].

$$D(r_{TV}, T_D) = \sum_{r_{SV}} \int_0^{T_D} A(r_{SV}; t)\, S(r_{TV} \leftarrow r_{SV})\, dt \tag{3.12}$$

where T_D stands for the integration time and D for the mean absorbed dose in a target voxel (r_{TV}) due to its own irradiation (i.e., accumulated activity in that target voxel) and from several neighboring uniform source voxels (r_{SV}) (Figure 3.9). The conversion from activity to absorbed dose is based on the assumption that the energy emitted by the radioisotope will either all be deposited in the voxel itself or in the surrounding voxels, with uniform attenuation [72]. Although this is a more accurate approach than organ-based dosimetry, it is limited when applied to lesions in non-uniform tissues as it does not consider medium heterogeneity (by definition, VSVs are calculated for homogeneous tissues) [91]. However, the assumption of homogeneity at the voxel level can be acceptable for several body areas, such as the abdomen. Overall, this approach allows fast and simple 3D dosimetry with little constraints [92], that yields results comparable to MC simulations.

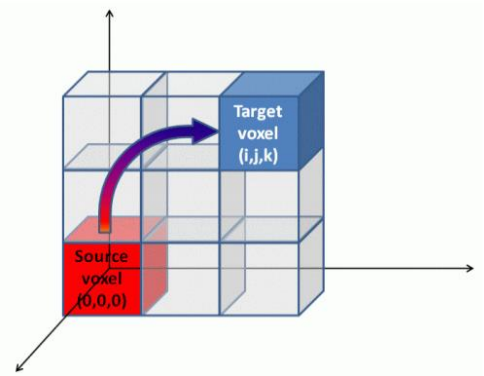

Figure 3.9. Schematic representation of the energy that is deposited in a generic target voxel (i,j,k) due to irradiation from a source voxel (0,0,0). Adapted from [93].

SPECT and PET devices currently used in clinical routine present several voxel dimensions depending on the acquisition field of view (FOV), reconstruction matrix and other factors [94]. Concerning dosimetry, there is a lack of radionuclide VSVs for all possible combinations of voxel dimensions, tissues and isotopes used in SPECT and PET studies. Several groups aimed to fill this gap by employing direct MC simulations [71][94] and performing calculations based on the convolution [95] or numerical integration [96] of dose point kernels (i.e., energy deposition kernels from point isotropic radioactive sources) to obtain new sets of VSVs. However, since these last methods are complex, VSVs are usually pre-calculated using MC simulations and are radionuclide-, tissue- and voxel size-specific [71]. For instance, using EGS4 MC code, Bolch et al. [71] calculated VSVs for five radionuclides and two cubic voxel sizes. This data was made available for the scientific community in the MIRD Pamphlet No 17. Free online databases of VSVs specific of different radioisotopes and voxel dimensions are currently available [94]. In this work, VSVs were computed with the TOPAS-MC toolkit and were compared with the published data from [94].

3.7. Dose Quantification in ^{177}Lu-DOTATATE PRRT

All clinical institutions worldwide follow the same therapy regimen, in which all patients are injected with the same 7.4 GBq therapeutic radiation activity in all four treatment cycles. The joint IAEA, EANM, and SNMMI practical guideline on PRRT states that personalized dosimetry calculations can provide valuable information to improve treatment outcome [42]. With the increasing implementation of ^{177}Lu-DOTATATE PRRT for the treatment of NETs so has increased the interest in the evaluation of the absorbed dose that can be tolerated by the patient, with minimal renal and hematological impairment [37]. Multiple studies highlight the importance of dosimetry in PRRT, reporting absorbed dose estimates, comparisons of 2D and 3D methods and response/absorbed dose correlations.

The threshold for the total absorbed dose in the bone marrow has been set at 2 Gy. Bone marrow dosimetry has been traditionally performed using both non-imaging and imaging approaches, such as sequential blood samples [97] and planar imaging [98]. Blood samples are used to estimate self-dose to the bone marrow considering blood kinetics, which is the main source of marrow irradiation [78]. However, since compounds labeled with ^{177}Lu have a fast blood clearance, the absorbed dose is underestimated when using blood-based methods [99]. Furthermore, there are cases where irradiation from the surrounding organs (e.g., spleen, liver and kidneys) and bone metastases can be significant, rendering quantitative imaging necessary [78]. In this context, Svensson et al. [98] developed a dosimetry protocol for ^{177}Lu-DOTATATE PRRT, using the MIRD schema and a series of post-therapeutic planar images. They found that a higher mean absorbed dose in the bone marrow was related

to a depletion of the marrow activity (i.e., decreased hemoglobin, white blood cell and platelet counts) and possible toxicity. Regarding the kidneys, the upper renal absorbed dose threshold has been currently set at 23 – 27 Gy, established according to EBRT studies as it corresponds to a 5% probability of nephrotoxicity five years after irradiation [78]. Multiple groups reported kidney absorbed dose based on 2D imaging. Gupta et al. [100] determined the absorbed dose in the kidneys, liver, spleen, pituitary gland and tumors using planar scans and the MIRD schema for organ-level dosimetry. Considering the renal absorbed dose limit, they reported that a maximum activity of 10 GBq/cycle could be safely injected to a patient. However, a significant inter-patient variability was seen, particularly in the tumor absorbed dose. Similarly, Sandstrom et al. [101] proposed an individualized dosimetry protocol in which patients were administered with a fixed radiation activity of 7.4 GBq/cycle, performing a variable number of cycles provided that the absorbed dose constrains to the critical organs were respected. In 99% of the patients, the kidneys were the dose-limiting organ. The optimal number of cycles was quite variable. Around 50% of the individuals could perform more than four treatment cycles, whereas 20% could not tolerate the standard regimen. Despite these results, pure 2D methods are not the most accurate for dosimetry as they do not consider anatomical variations, attenuation and tissue overlap.

With the introduction of spatial dosimetry and proof of its great accuracy, the conventional approaches were progressively replaced. Several suggestions on how to use 3D data to calculate ^{177}Lu-DOTATATE absorbed dose distribution in organs can be found extensively in the literature. One of the first studies regarding ^{177}Lu SPECT imaging was performed by Sanders et al. [102]. They validated a dosimetry protocol for quantitative ^{177}Lu SPECT/CT *in vivo*, using urine samples. The outcome was promising, showing that this was a viable approach for PRRT dosimetry but that could benefit from improved imaging reconstruction methods. Beauregard et al. [103] demonstrated the potential of serial quantitative SPECT imaging for assessing bone marrow toxicity in ^{177}Lu-DOTATATE PRRT as a less invasive method than blood sampling and more accurate than planar imaging, reducing patient burden and enabling the implementation of personalized dosimetry in a clinical setting. Moreover, recent studies [104][105] describe the use of sequential quantitative SPECT/CT images to perform voxel-based dosimetry to investigate individualized kidney tolerance for additional treatment cycles. Organ dosimetry performed using OLINDA/EXM software with an exponential clearance model was found to have good reproducibility across all cycles and kidney absorbed dose was below the established limits. Similar conclusions were drawn by Garske-Román et al. [106] in a recent prospective study, in which the relation between treatment response and critical organ absorbed dose was also investigated. Patients were administered multiple cycles at a fixed activity (7.4 GBq/cycle) of ^{177}Lu-DOTATATE until the absorbed dose limits were reached. In three to nine therapy cycles, around 62% of 200 patients with advanced metastatic NETs reached the maximum renal absorbed dose, and these presented longer overall survival. In addition, a positive response rate of around 31% was seen in these patients with no significant nephrotoxicity three years after therapy. This supports the hypothesis that the established renal threshold may not be suitable and that if the injected activity or number of cycles is based on this value, most patients end up being undertreated. Albeit their great accuracy, pure 3D protocols are not faultless as they have a substantially higher computational demand than planar-based dosimetry.

The compromise between accuracy and computational burden can only be managed by the chosen dosimetry approach or imaging protocol. That is why novel imaging-based methods continue to emerge, aiming to attain absorbed dose estimates with an appropriate degree of accuracy in a practical manner. Some groups investigated the possibility of accurate dosimetry in ^{177}Lu-DOTATATE PRRT using a single SPECT and multiple whole-body (WB) planar scans acquired after injection. This is called the hybrid approach as it combines both 2D and 3D quantitative information. Sundlov et al. [107] performed a prospective study where they developed an in-house software package for kidney dosimetry following this protocol. Kidney function was found to gradually decline after the treatment, without a specific

correlation with mean absorbed dose and with some patients completing up to eight treatment cycles without significant nephrotoxicity. Overall, the hybrid planar-SPECT/CT method for dosimetry in TRT has shown a better performance than planar-based methods, with comparable results to purely SPECT-based protocols. Therefore, despite not enabling voxel-level dose quantification, this approach is particularly interesting for situations where multiple SPECT imaging is not feasible [108].

These studies showed that individual treatment verification (i.e., post-treatment) in PRRT with ^{177}Lu-DOTATATE, based on dosimetry-guided protocols, is feasible and that the adjustment of the injected activity or number of cycles is essential to increase survival. However, there is a significant variability in individual absorbed dose estimates among the different groups [109], related to the use of different dosimetry techniques and imaging protocols. Nevertheless, the conclusions reported by most studies are very similar. In addition, several groups report a great inter-patient variability in the renal and tumor absorbed doses, which is due to variations in the tracer's metabolism and diversity of tumor biology [99]. This suggests that more studies are needed, with a detailed description of the followed dosimetry protocols, to assist in the establishment of a standard protocol that can be used in all institutions for the administration of personalized therapy.

Chapter 4

Materials and Methodology

In this chapter, a detailed description of the steps followed in a retrospective investigation of ^{177}Lu-DOTATATE PRRT patient studies is provided, namely therapy and imaging acquisition protocol, data processing, biokinetic analysis and VSVs computation. Furthermore, we present the dosimetry protocol currently followed in the CCC for patients undergoing ^{177}Lu-DOTATATE PRRT, based on sequential 3D imaging. Two different dosimetry analysis were conducted:

a) Post-treatment dosimetry using ^{177}Lu-DOTATATE SPECT scans. The aim was to compare the dosimetry calculated by VSVs and MC simulations, and assess possible critical organ toxicity.

b) Pre-treatment dosimetry using ^{68}Ga-DOTANOC PET/CT scans. The aim was to verify the potential of these scans to predict post-therapy dose distribution.

The chapter ends with an explanation of the statistical analysis of the computed data.

4.1. Therapy Protocol and Patient Data

Patients who had histologically confirmed inoperable and/or metastatic neuroendocrine neoplasia overexpressing somatostatin receptors, satisfactory glomerular function and hematological parameters, hepatic function not severely compromised, and life expectancy longer than six months were deemed eligible for therapy with ^{177}Lu-DOTATATE at the CCC. Individuals who did not meet these criteria were excluded, as well as pregnant, breastfeeding or pediatric patients.

Between August 2017 and January 2020, six individuals were administered, intravenously, with a therapeutic radiation activity of 7.2 ± 0.5 GBq/cycle of ^{177}Lu-[DOTA0,Tyr3]-octreotate (Lutathera®), every eight weeks, performing a total of four treatment cycles/patient. Patients' characteristics are summarized in Table 4.1. Since the radiopharmaceutical is primarily eliminated via kidneys, an infusion of negatively charged amino acids (l-lysine and l-arginine) was administered to each patient, 30 minutes before the injection of the radiopeptide, to prevent tubular reabsorption. The injected activity and residual activity in the vial were measured with the Capintec CRC-25R (Capintec, Inc.) dose calibrator, which has an uncertainty of 2.5 %, provided in the calibration datasheet.

Table 4.1. Characteristics of the patients with NETs.

Number of patients (n)	6
Gender, n (%)	
Male	4 (66 %)
Female	2 (33 %)
Mean Age at first therapy cycle (range)	61 (45 - 70)
Mean Weight (range)	68 (50 - 78)
Mean Height (range)	168 (150 - 185)

Age, weight and height expressed in years, kg, and cm, respectively.

4.2. Patient Imaging Dataset

Twenty-four treatment cycles were retrospectively analyzed (4 cycles/patient). In each cycle, patients were referred for imaging at specific time points before and after therapeutic injection. Imaging was performed at the NM-Rf Department of the CCC, in Lisbon, according to the clinical protocols used in this institution. All patients gave their written informed consent, which was in accordance to the guidelines of the Ethics Committee of the Champalimaud Foundation. All data used in the retrospective analysis were anonymized. Images were acquired with clinical intent. Nonetheless, dose quantification was performed under the assumption that the acquisition configuration remained unchanged for all patients and treatment cycles.

A pre-therapeutic ^{68}Ga-DOTANOC PET/CT total body scan, from the skull vertex to midthigh, was acquired with the Phillips PET/CT GEMINI TF scanner (Phillips Medical Systems, The Netherlands), to determine if patients were eligible to therapy with ^{177}Lu-DOTATATE. Abdominal SPECT and planar (anterior-posterior) WB imaging was performed with the Phillips BrightView Dual Head gamma camera (Phillips Medical Systems, The Netherlands) equipped with parallel-holes medium energy general purpose (MEGP) collimators. WB planar imaging was performed at 1 h, 4 h, 24 h and 120 h post-injection (PI). Scan velocity was 12 cm/min and patient contour technique was used. Data was stored in a 512 × 1024 matrix with 2.009 mm × 2.009 mm pixels. During acquisition, patients were in the supine position with upper limbs placed along the body. For 5 patients, two abdominal SPECT scans were acquired 24 h and 120 h or 168 h PI[2], with 128 projections of 15 sec/view in non-circular step-and-shoot mode. For the other patient (patient #5), only one acquisition was performed 24 h PI, under the same protocol. For these acquisitions, energy windows included the 111 keV (102.7 – 119.3 keV) and 208 keV (192.4 – 223.6 keV) photopeaks (Table 4.2).

Table 4.2. SPECT protocol acquisition parameters for patients and phantom studies with ^{177}Lu.

Parameters	**Patient Studies**	**Phantom Studies**
Collimator	Medium Energy, General Purpose	
Energy Window	208 keV (192.4 – 223.6) 111 keV (102.7 – 119.3)	
Matrix	128 × 128	
Number of Frames	128	
Frame Length	15 sec	
Scan Arc	360º	
Orbit	Non-Circular	
Acquisition Mode	Step and Shoot	

Images were stored in three modes: for the 208 keV and 111 keV peaks alone, and with both energy peaks together. Better resolution was found in the image recorded for the 208 keV photopeak. Although the abundance of this photon is only 11%, the therapeutic activity of 7.4 GBq produces high quality images, with a satisfactory event rate and low dead time influence [43][59]. Therefore, only the images stored for the 208 keV photopeak were used in this study. In addition, following SPECT imaging, low dose CT scans (512 × 512 pixels) were acquired with the Phillips PET/CT GEMINI TF scanner, 24 h PI, with a voltage of 140 kV and effective integrated current (i.e., charge) of 60 mAs.

[2] The moment of the second SPECT acquisition varied between patients as, depending on the injection day, imaging at 120 h PI would fall in the weekend, which was not feasible and was, therefore, postponed two days.

4.3. Phantom Studies

Experiments were conducted with the National Electrical Manufacturers Association (NEMA 2012/IEC 2008) image quality phantom (PI Medical Diagnostic Equipment B.V., The Netherlands), containing six fillable spheres with volumes ranging from 0.5 to 26.5 cm^3 (Figure 4.1). The NEMA phantom was filled with water, with no background activity. This configuration was chosen since it offered simple scatter and attenuation properties that allow data acquisition with a setup similar to those found in patient studies.

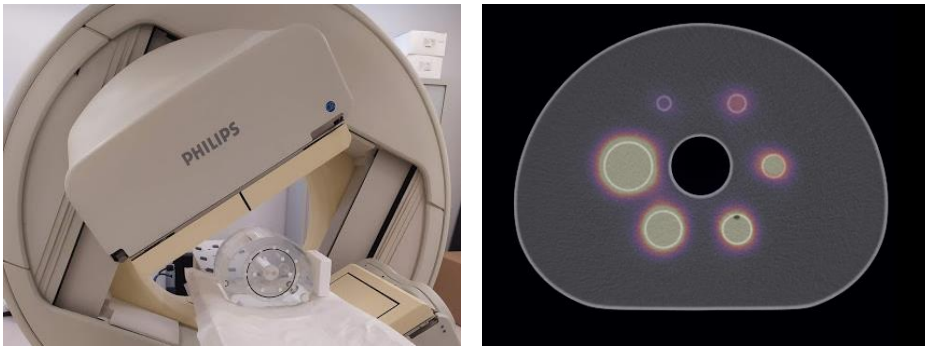

Figure 4.1. In the left panel, set up of the SPECT image acquisitions performed with the phantom. In the right panel, axial view of a SPECT scan of the NEMA phantom aligned with its CT image.

To ensure that the spheres had similar activity concentrations, calculations were made beforehand to determine which activity to draw from the vial for each sphere. After injection of the tracer, the spheres were filled to completion with water. The activity in the syringe was measured before and after filling the spheres. Due to the followed approach (i.e., solution was not made before filling the spheres) and the different residual activity in the syringe from each injection, the activity concentration was not the same in all spheres, which were filled with (mean ± standard deviation) 104.4 ± 5.4 MBq/cm^3 of an aqueous solution of ^{177}Lu. Activity values on the first acquisition day, corrected for residual activity in the syringe, are reported in Table 4.3.

Table 4.3. Volumes and activities (corrected for residual activity) of the spheres of the NEMA phantom, measured at the day of the first imaging acquisitions.

Sphere	Volume (cm^3)	Activity (MBq)	Concentration (MBq/cm^3)
S1	0.5	52.5	105
S2	1.2	137.2	114.3
S3	2.6	271.2	104.3
S4	5.6	576	102.8
S5	11.5	1177	102.3
S6	26.5	2597	98

The phantom was scanned sequentially (i.e., SPECT imaging) for seven days, performing a total of five acquisitions, using the same acquisition and reconstruction protocol as in the patient studies. A CT scan was acquired to perform the corrections for attenuation and scatter in the images. In all acquisitions, the phantom was placed in the center of the camera's FOV.

4.4. Phantom and Patient Data Processing

Pre-therapeutic ^{68}Ga-DOTANOC PET/CT scans were reconstructed using the iterative time-of-flight reconstruction algorithm (BLOB-OS-TF), which resulted in a 144 × 144 matrix with 4 mm cubic voxels.

CT-based attenuation correction and compensations for scatter, random coincidences, dead time and decay were included in the image reconstruction process. ^{177}Lu-DOTATATE SPECT scans were reconstructed with the iterative ordered-subset expectation maximization (OSEM) algorithm, using 3 iterations and 16 subsets, provided by the AutoSPECT Pro software (Phillips Medical Systems, The Netherlands), included in IntelliSpacePortal v.10.1 (Image and Information Management Software). Reconstruction resulted in a 128 × 128 SPECT matrix with 4.664 mm cubic voxels. A Butterworth low-pass filter with a cut-off of 2 cycles/cm and 10th order, was applied to sharpen the anatomical structures. The reconstruction algorithm included CT-based compensation for non-uniform attenuation and scatter, as well as CDR correction (i.e., resolution recovery).

Images acquired at different time points were registered to a common reference study. In particular, all SPECT images were manually co-registered to the CT scan (reference) acquired for each treatment cycle, using the AutoSPECT Pro software. Rigid transformations (e.g., translation and rotation) were applied, to preserve anatomical structures. Original DICOM (Digital Imaging and Communications in Medicine) images were converted to NiFTI (Neuroimaging Informatics Technology Initiative) format to simplify data transfer and analysis. In addition to the image corrections included in the reconstruction process, to achieve an accurate quantification, SPECT scans were also compensated for dead time losses, using the phantom experiments. The workflow with all the steps that were followed in processing the SPECT images is shown in Figure 4.2. Before dosimetry calculations, the scans were corrected for several image degrading phenomena and converted into quantitative images with the desired matrix size. Correction factors determined from the phantom experiments were used. A detailed description of these steps is given in the following sections. No correction was applied to planar acquisitions.

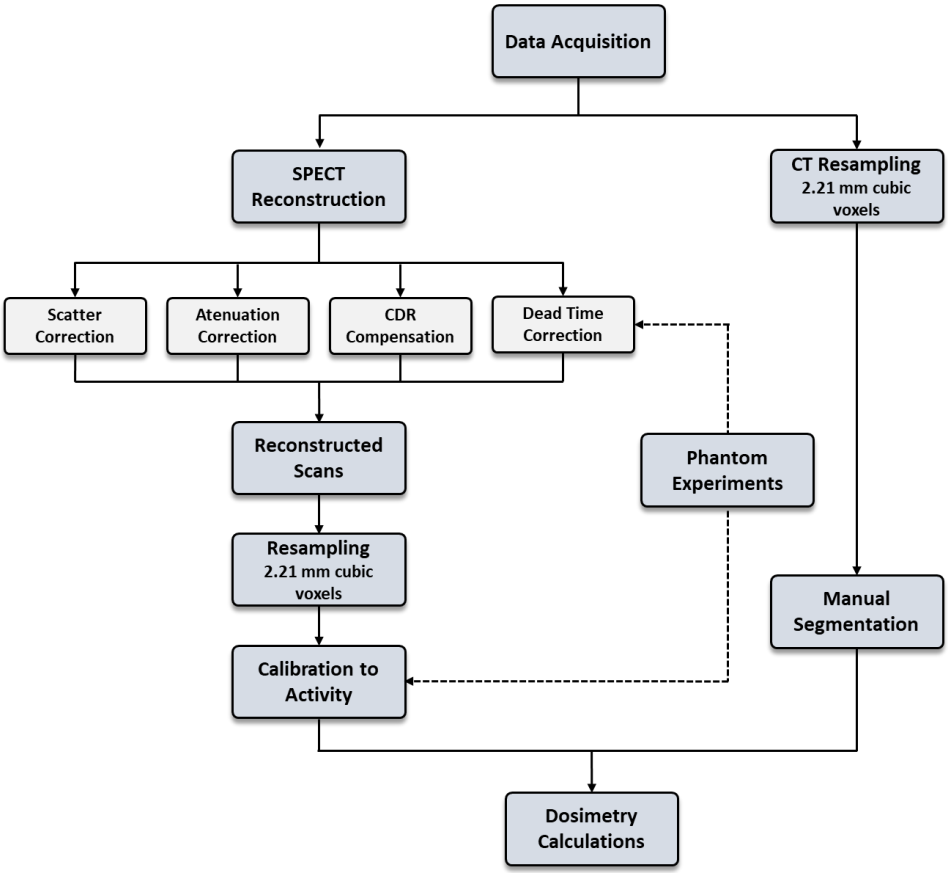

Figure 4.2. Workflow of the steps followed in data processing.

4.4.1. Dead Time Correction

With a dedicated in-house MATLAB R2018a (The MathWorks, Inc, United States) routine, a correction factor for dead time losses was determined from a series of phantom measurements with gradually decreasing activity, the decaying source method. Concerning accuracy, it has been reported that measurements should be performed for a time period equal to, at least, the half-life of the radionuclide under study [49]. Thus, given that the half-life of ^{177}Lu is 6.647 days, five phantom SPECT images were acquired over a 7-day period to estimate the dead time constant of the system.

Scans in NiFTI format were imported into MATLAB using the *Tools for NifTI and ANALYZE image* package [110]. To assess dead time losses, the total counts detected over the entire FOV of reconstructed SPECT scans were divided by the image's acquisition time to attain the corresponding count rate (cps). No background correction was performed. Since it has been suggested that contemporary gamma cameras can be described by a paralyzable behavior (i.e., a new event during the dead time resets the recovery period) [111][112], the data was fitted to the Sorenson's paralyzable model [113] using the following equation

$$R_{obs} = R_{true}\, e^{-R_{true}\tau_p} \tag{4.1}$$

that expresses a relationship between the observed count rate, R_{obs}, obtained from the experiment, and true count rate (i.e., absence of dead time losses), R_{true}. Here, τ_P is the paralyzable dead time constant or dead time of the system. To estimate the dead time, the decaying source method discussed in Knoll [49] was used. The true count rate behavior, over time, can be approximated by the known exponential decay of the source

$$R_{true}(t) \approx R^0_{true} e^{-\lambda t} \tag{4.2}$$

where R^0_{true} is the initial true count rate and λ is the physical decay constant of ^{177}Lu. Therefore, Equations (4.1) and (4.2) can be combined into

$$\ln(R_{obs}) + \lambda t = \ln(R^0_{true}) - e^{-\lambda t} R^0_{true}\tau_p\,. \tag{4.3}$$

By plotting $\ln(R_{obs}) + \lambda t$ (i.e., ordinate) versus $e^{-\lambda t}$ (i.e., abscissa) and applying a linear fit ($y = mx + b$) to the data using the total least squares algorithm, the intercept gives $\ln(R^0_{true})$ and the slope gives $-R^0_{true}\tau_p$. Thus, the paralyzable dead time constant was estimated according to

$$\tau_p = -m/R^0_{true} \tag{4.4}$$

where R^0_{true} was determined as e^b. The uncertainty of the dead time constant was estimated with the method described in Appendix C. Equation (4.1) can only be solved iteratively. Thus, dead time corrections were applied to the images following the approach presented by Heemskerk et al. [114]. True count rates were determined using the Lambert W function (Eq. (4.5)) and the estimated dead time constant.

$$W(z)e^{W(z)} = z \tag{4.5}$$

The accuracy of this method depends on the accuracy of the determinations of the dead time constant. Considering Equations (4.1) and (4.5), we find

$$z = -R_{obs}\tau_p \tag{4.6}$$

$$W(z) = -R_{true}\tau_p\,. \tag{4.7}$$

Combining both Eq. (4.6) and (4.7), we can derive an expression for R_{true},

$$R_{true} = -\frac{W\left(-R_{obs}\tau_p\right)}{\tau_p}. \tag{4.8}$$

As in [114], only the principal branch, W_0, of the Lambert function was considered, to determine a real solution for R_{true}. Therefore, its Taylor series around 0 is

$$W_0(z) = \sum_{n=1}^{\infty} \frac{(-n)^{n-1}}{n!} z^n \tag{4.9}$$

which allows a straightforward calculation of R_{true}. However, for this calculation, we used the MATLAB function *lambertw* considering $z = -R_{obs}\tau_p$. Dead time losses were then quantified as the percentage difference between observed and true count rates.

4.4.2. Registration and Resampling

SPECT and CT images were resampled in open-source 3D Slicer software (v4.10.2) to 2.21 mm cubic voxels, via linear interpolation, since VSVs of that size and shape were used in later absorbed dose calculations. This resampling was performed to achieve a compromise between the original SPECT and CT scans matrix size, and satisfactory calculation accuracy and reduced computation time. Moreover, since null voxels lead to a longer computation without adding useful information to the result, processed SPECT images were cropped. Caution was taken to avoid the exclusion of vital data. Regarding pre-therapeutic ^{68}Ga PET/CT scans, these were co-registered with the SPECT and CT scans from the first treatment, in Slicer, using rigid transformations. First, the CT – CT registration was performed, due to more detailed anatomical disposition, and the transformations were then applied to the PET scans, which were also cropped and upsampled to match the dimensions of the respective SPECT images.

4.4.3. Segmentations

Using Slicer, the VOIs, corresponding to the spleen, liver, kidneys, red bone marrow, and NETs, were manually outlined, slice by slice, on the patient's CT scans with 2.21 mm cubic voxels (Figure 4.3). The presence of hepatic lesions is a typical feature of the patients included in the study. Thus, the total liver volume included these lesions.

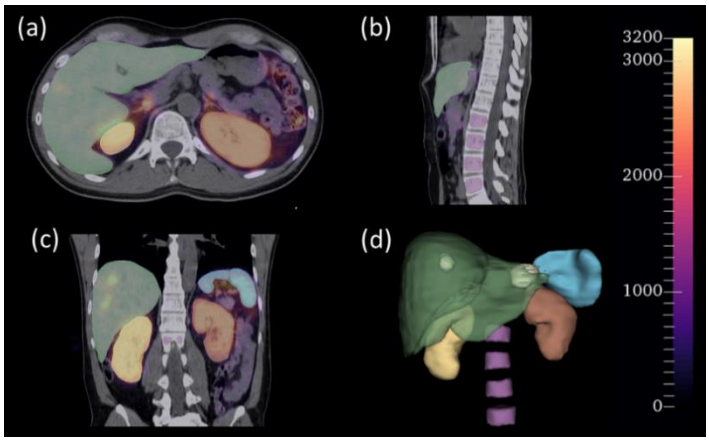

Figure 4.3. (a) axial, (b) sagittal and (c) coronal projections of the VOIs (liver, spleen, kidneys, bone marrow and NETs) of patient #3 in the 1st treatment cycle, superimposed to the SPECT scan acquired 24 h PI fused with the respective CT scan. (d) 3D representation of the segmented VOIs. Green: Liver; Yellow: Right Kidney; Brown: Left Kidney; Blue: Spleen; Purple: Bone Marrow; White: NETs.

Kidney segmentations included the renal cortex and medulla, but not the pelvis. The segmentation of the bone marrow segmentation encompassed the trabecular region on the L2 to L5 lumbar vertebrae, when included in the FOV. NETs segmentation was based on both CT morphology and uptake information from SPECT scans. For all patients, the same NETs were segmented in all treatment cycles to allow for comparison and evaluation of response to therapy. In addition, the interface between tumor and healthy tissue was delineated. A VOI with a uniform-thickness shell of 4.42 × 4.42 × 4.42 mm (i.e., two voxels in each dimension) was defined. Half of the VOI contained values outside the tumor's VOI and the other half included values inside. All VOIs were drawn by a single individual to minimize inter-observer variability and were carefully validated by a NM physician.

4.5. Image-based Activity Quantification

4.5.1. SPECT-phantom Calibration Factor

The reconstructed scans represent the 3D distribution of the photons emitted by the radionuclide injected into the patient. To convert the reconstructed image's voxel values to activity, the gamma camera system must be calibrated using a ^{177}Lu source with a well-known activity [37]. SPECT images of the NEMA phantom, with a well-known activity in each sphere, were used to estimate the camera's 3D CF (MBq/cps). Since the phantom was filled with water, it represented an acceptable approximation of the scatter and attenuation properties in patient imaging, reducing the effects of imperfect corrections. As mentioned, image acquisition of the phantom was repeated at different times. However, the activity was only measured at the first day of acquisitions. Therefore, activity was decay corrected to each acquisition time (i.e., 72 h, 120 h, 144 h and 168 h after the first acquisition), using the half-life of ^{177}Lu (6.647 days). For each scan, the CF_{SPECT} was determined as follows

$$CF = \frac{A_{FOV}}{C_{FOV}/T_{acq}} \tag{4.10}$$

where T_{acq} is the acquisition duration (i.e., time per frame times total number of frames), A_{FOV} and C_{FOV} represent the total decay-corrected activity and counts in the FOV, respectively. As resampling modifies the voxels' values, CF_{SPECT} estimations and activity calibration were performed using the scans with the final matrix size (i.e., 2.21 mm cubic voxels), to avoid inaccurate dosimetry calculations. The five computed CF_{SPECT} (i.e., from the five imaging acquisitions) were averaged to determine the final value, which was used to convert patient SPECT images to activity according to

$$A^{i,j,k} = \frac{C^{i,j,k}}{t_{acq}} \cdot CF \tag{4.11}$$

where (i,j,k) are the spatial indexes of each voxel. Patient studies did not allow the validation of quantification since no SPECT scans were acquired before the patient voided.

4.5.2. Planar-based Biodistribution of ^{177}Lu-DOTATATE

Activity quantification from planar imaging was achieved using a pixel-based method, the conjugate view approach, which allows the determination of activity within a region of interest (ROI) without requiring knowledge of the source's depth [37].

This method involves the computation of the geometric mean with the anterior and posterior projections, which was performed in a dedicated MATLAB routine, according to

$$I_{GM} = \sqrt{I_A I_P} \tag{4.12}$$

where I_A and I_P are the pixel counts in the anterior and posterior view, respectively. Since the two projections were inverted, it was necessary to flip one, along a vertical axis (Figure 4.4), to enable the geometric mean computation. This step was performed on the posterior image, since visual recognition of anterior images is simpler. Note that, when computing a pixel-by-pixel geometric mean, null pixels in one projection will lead to a null value, which underestimate the average count rate and, consequently, the activity. However, it does not seem to be critical for ^{177}Lu-DOTATATE imaging, since a significant activity dose is usually injected, resulting in a high number of events (i.e., different from "null pixels").

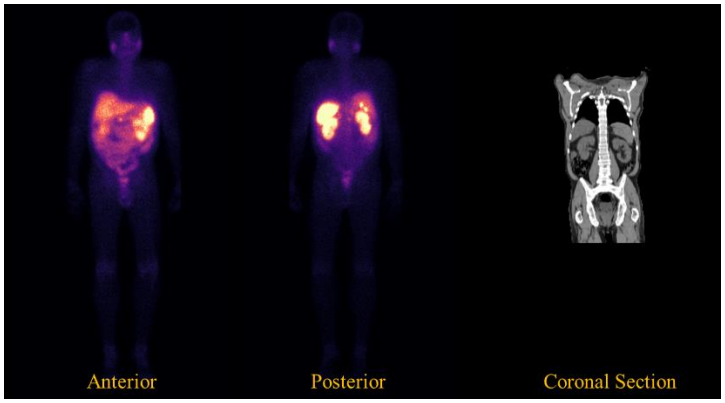

Figure 4.4. Original anterior-posterior planar WB scan and coronal section of the CT scan acquired approximately 24 h PI in the first treatment cycle of patient #1. Two saturated NETs are seen in the posterior projection. Before computing the geometric mean, pixel-by-pixel, the displayed posterior view was mirrored.

To study the physiological biodistribution of ^{177}Lu-DOTATATE, TACs were generated (i.e., tracer's planar-based biodistribution as a function of time). These were determined from a series of WB planar scans from different time points PI (Figure 4.5). Some scans contained a ^{177}Lu source in their FOV, positioned next to the patient, to help determine the camera's 2D CF. The source was manually delineated, in Slicer, and the ROI was used to remove it from the images so that the total activity in the FOV matched the total activity in the body at each instant. Activity quantification and TACs generation was performed using an in-house MATLAB routine.

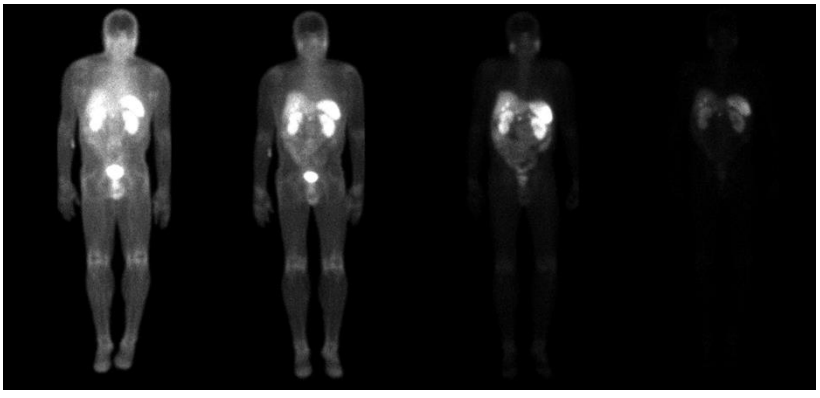

Figure 4.5. Conjugate view of the planar WB images (i.e., geometric mean of anterior and posterior projections), in counts, of patient #1 in the first treatment cycle 1 h, 4 h, 24 h and 120 h (left to right) PI. All images are presented at the same scale.

To convert counts into activity, a patient-specific 2D CF (i.e., detection efficiency), was determined using the planar WB image acquired 1 h PI. It was assumed that no biological elimination had occurred between the injection and imaging, which is supported by the high bladder uptake observed in this scan.

Therefore, the activity contained in the FOV 1 h PI was considered equal to the decay corrected injected activity. Note that the actual injected activity was determined by considering the physical decay of ^{177}Lu between the time of activity measurement and the time of injection, as well as the residual activity in the vial. Furthermore, it was assumed that all injected activity was contained in the images' FOV. The CF_{PLANAR} was defined as the ratio between activity and count rate at 1 h PI. The activity contained in the FOV was determined as the ratio between the total count rate and estimated CF_{PLANAR} (Eq. (4.11)). No compensation for background counts was performed.

4.5.2.1. Whole-Body Analysis

WB activity at each time point was determined using the quantitative information from the planar WB scans. Activity in all instants was normalized to the total injected activity (Eq. (4.13)) to present the relative uptake (i.e., fraction of injected activity, IA) and tracer retention.

$$IA(t) = \frac{A_{FOV}(t)}{A_{WB}^{admin}} \times 100 \tag{4.13}$$

With MATLAB R2018a statistics toolbox, activity in the WB was modelled as a bi-exponential decay process (Eq. (4.14)). As the fit requires a minimum of four points, this analysis was only performed for treatment cycles with four imaging acquisitions. Therefore, a total of 12 cycles were included.

$$A = e^{-\lambda_1 t} + e^{-\lambda_2 t} \tag{4.14}$$

In the equation above, λ_1 and λ_2 are the effective decay constants of the fast and slow clearance components, respectively. Effective half-life of the tracer in the WB was extrapolated from the fits.

4.5.2.2. Organ-level Analysis

Organ and NETs activity at each time point was determined using the quantitative planar scans. The ROI of each organ (i.e., maximum intensity projections of the 3D segmentation on the CT scans – coronal plane) were co-registered to all planar images and resampled to their dimensions (via linear rigid transformations and nearest neighbor interpolation), with Slicer. Using ROI analysis, activity was normalized to the total injected activity (Eq. (4.15)) to present the relative uptake.

$$IA(t) = \frac{A_{ROI}(t)}{A_{WB}^{admin}} \times 100 \tag{4.15}$$

TACs were generated for the liver, spleen, kidneys and NETs by fitting mono and/or bi-exponential functions to the data points. Bone marrow was not included in this particular study since it presented poor visualization in planar scans and an incorrect registration would lead to inaccurate conclusions. According to the EANM guidelines on internal dosimetry [115], organ and tumor TACs were generated for all treatment cycles with at least two planar image acquisitions. Effective half-life of the tracer in the ROIs was extrapolated from the exponential fits.

4.6. Voxel S-values Computation

The second part of this project was focused on the study of the influence of radionuclide VSVs in 3D dosimetry of ^{177}Lu in PRRT. The calculation of VSVs for different isotopes, materials and cubic voxel dimensions was performed using the TOPAS-MC toolkit v.3.5, based on Geant4 v10.06.p01. The code was compiled on a Linux Ubuntu 20 workstation equipped with Intel Core i7 9th Gen processors @ 2.6 GHz (16 GB RAM). No variance reduction techniques were applied to improve simulation speed. To achieve a reasonable compromise between accuracy and simulation speed, a range cut of 0.05 mm

was applied to all simulated particles and photons (i.e., range for electron and absorption length for photons [116]). Radiation with a path-length lower than the established cutoff was produced but not tracked, and its energy was deposited locally within that range. VSVs were used later in this work in dosimetry calculations at the macro scale (i.e., voxel-level analysis). Thus, the cutoff did not significantly impact the results since it is smaller than the chosen voxel size (i.e., 2.21 mm or 4.42 mm cubic voxels) [69] and the short-path radiation contributes to the overall dose tallied in the voxel (i.e., attenuated within the voxel where is produced, regardless of the applied range cut).

Electromagnetic interactions were simulated with Geant4's standard EM package, which includes photoelectric effect, pair production, Compton and Rayleigh scattering for photon interactions, and bremsstrahlung, atomic ionization and multiple scattering for electron interactions. The production of characteristic X-ray (i.e., fluorescence), PIXE (particle induced X-ray emission) and Auger electrons was activated in the code and considered during calculations. The radioactive decay of the emitting source was simulated using the G4RadioactiveDecayPhysics module, which provides at-rest processes, such as the full disintegration of radioactive nuclei (e.g., ^{177}Lu, ^{137}I, ^{60}Co) by α, β^+ and β^- emissions, isomeric transition and electron capture. The underlying model is empirical and uses decay data (e.g., half-lives, nuclear level structure for parent or daughter nuclide and decay branching ratios) from the Evaluated Nuclear Structure Data File (ENSDF) [117]. The G4Decay physics module was also included to simulate possible decay processes that occur after ion interactions.

TOPAS was run with the RANECU pseudo-random number generator. Particle transports, due to the decay of ^{177}Lu and ^{68}Ga, were simulated in two finite homogeneous mediums: soft tissue (i.e., ICRU 4-component soft tissue, $\rho = 1.0$ g/cm^3) and bone (i.e., compact bone, $\rho = 1.85$ g/cm^3), with the elemental composition and physical density defined by International Commission on Radiation Units and Measurements (ICRU) Report 44 [118]. To achieve low statistical uncertainties[3] (< 10%), simulations were performed using 25 million events. Source particle was considered as atoms of ^{177}Lu and ^{68}Ga, at rest (the only initial physical process was the decay), such that each event corresponds to one full decay, including multiple primary particles. The emitting isotropic radioactive source was uniformly sampled within the central cubic voxel (0,0,0). To allow for backscatter, regions beyond the phantom were simulated as air. The absorbed dose (Gy), caused by all primary and secondary particles, was scored on a grid of 11×11×11 cubic voxels of 2.21 mm and 4.42 mm, centered at the origin of the cartesian referential (Figure 4.6). A total of 8 simulations were performed over the course of 1-2 weeks.

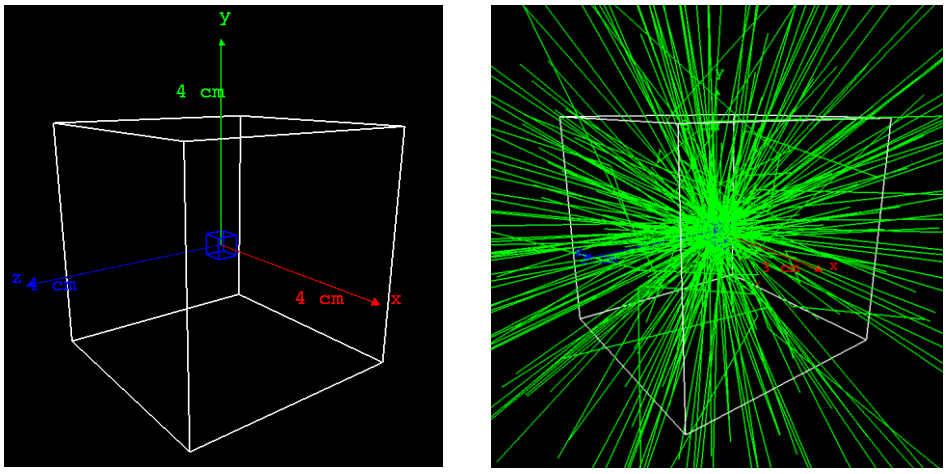

Figure 4.6. On the left: OpenGL visualization of the simulation set up for VSVs computation. The isotropic radiation source is uniformly distributed within the blue voxel (0,0,0) centered at the origin of the cartesian referential. The absorbed dose was

[3] Estimated according to Chetty et al. [119].

scored on a grid of 11×11×11 cubic voxels around the blue voxel, included. On the right: Representation of the radiation transport in the described set up, considering a reduced number of events. Photons are represented in green.

The absorbed dose scored in each voxel was converted, in MATLAB, in dose to the target voxel per unit of accumulated activity ($mGyMBq^{-1}s^{-1}$), and associated with the target position in the cartesian grid (i,j,k). All VSVs datasets computed in this study were recorded in text files that can be imported into any in-house code designed for voxel-wise internal dosimetry calculations. The VSVs were provided within an octant of 6×6×6 cubic voxels, as a function of voxel integer 3D coordinates, ranging from (0,0,0) up to (5,5,5). VSVs include the contributions from beta, Auger and γ-emissions. To benchmark the new datasets, ^{177}Lu VSVs were compared to validated data by Lanconelli et al. [94], who used the EGSnrc (DOSXYZnrc) MC code. For a qualitative analysis, VSVs were plotted, in one dimension, as a function of the radial distance to the source, r_n, defined as

$$r_n = \sqrt{(\Delta \cdot i)^2 + (\Delta \cdot j)^2 + (\Delta \cdot k)^2} \tag{4.16}$$

where (i,j,k) are the cartesian coordinates of the target voxel and Δ is the voxel size. Data was sorted by radial distance, such that $0 \leq r_1 \leq \ldots \leq r_n$, where $r_n = 0$ corresponds to the source voxel. For a quantitative comparison, the relative difference, ε, was determined for each target voxel with respect to the reference data (Eq. (4.17)) and was represented as a function of the distance to the source voxel.

$$\varepsilon_{i,j,k} = \frac{S_{i,j,k}^{TOPAS-MC} - S_{i,j,k}^{\text{DOSXYZnrc}}}{S_{i,j,k}^{\text{DOSXYZnrc}}} \times 100 \tag{4.17}$$

After validation, the VSVs computed for ^{177}Lu in soft tissue and 2.21 mm cubic voxels were used in voxel-level dosimetry with the convolution method. A detailed description of the dosimetry protocol is provided in the following section.

4.7. Post-treatment Dosimetry

Dosimetry calculations were performed using two computational approaches, the convolution method with VSVs and TOPAS-MC simulations (Figure 4.7). In this work, two different analyses were performed. The first involved the use of post-therapeutic ^{177}Lu-DOTATATE SPECT and CT scans to assess absorbed dose distribution after PRRT.

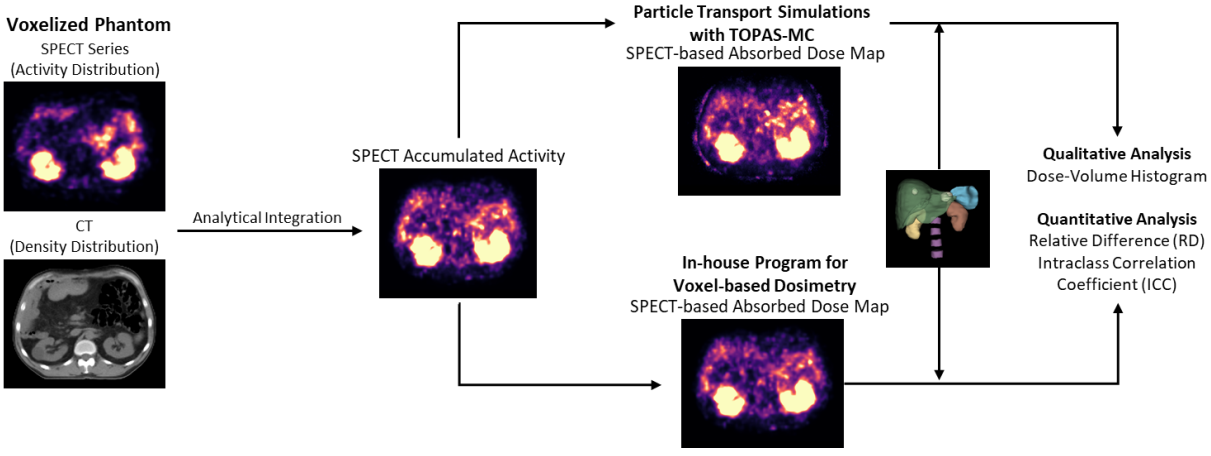

Figure 4.7. Dosimetry workflow for a PRRT post-treatment study (an identical methodology was used for ^{68}Ga-PET/CT pre-treatment planning dosimetry, considered in this work as one treatment cycle), using VSVs and MC simulation (TOPAS). Concerning VSV dosimetry, the time-integrated activity distribution is convolved with pre-calculated ^{177}Lu VSVs (soft-tissue and 2.21 mm cubic voxels) to obtain absorbed dose distributions. Regarding MC simulations, the time-integrated activity distribution is combined with the voxelized CT scans and used for voxel-based radiation transport. Manual segmentations are applied to the clinical data to compute the mean absorbed dose in the critical organs and NETs.

After quantification of the SPECT scans, the two parametric quantitative images (i.e., activity distribution at 24 h PI and 120 h or 168 h PI) were resized to the same dimensions in Slicer. The largest number of voxels in each dimension was kept so that no information was lost. In a MATLAB routine, these resized scans were used to compute the accumulated activity distribution, given by SPECT, which was used in both dosimetry methods. The image of accumulated activity, $\tilde{A}^{i,j,k}$ (MBq·s), for each cycle, was determined by numerical integration of the activity maps at specific time intervals (12 h – 72 h or 96 h, and 72 h or 96 h to infinity PI) and subsequently added together to obtain the total time-integrated activity distribution (Figure 4.8) and ultimately the total absorbed dose distribution.

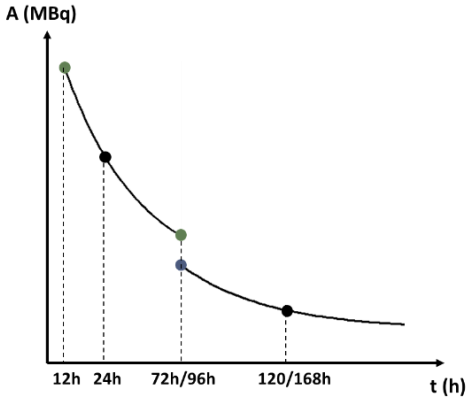

Figure 4.8. TAC used to determine the accumulated activity maps, defined as the area under the curve. An exponential decay with the physical half-life of ^{177}Lu was considered. The first 12 h PI were not included in the calculation. The two green and one blue points represent the activity values estimated from the SPECT scans acquired 24 h and 120 h or 168 h PI, respectively.

An exponential function was considered for the integration, using the physical half-life of ^{177}Lu (Eq. (4.18)). When only one SPECT acquisition was available in a treatment cycle, Equation (4.19) was used instead, where the integration limits were defined from 12 h to infinity.

$$\tilde{A}^{i,j,k} = \int_{12\,h}^{72\,h} A_{12\,h}^{i,j,k} e^{-\lambda_f t}\, dt + \int_{72\,h}^{\infty} A_{72\,h}^{i,j,k} e^{-\lambda_f t}\, dt \tag{4.18}$$

$$\tilde{A}^{i,j,k} = \int_{12h}^{\infty} A_{12h}^{i,j,k} e^{-\lambda_f t}\, dt \tag{4.19}$$

In the expression above, A represents the initial activity at each period, and λ_f is the physical decay constant. For the first and second time periods, initial activity distributions (i.e., 12 h and 72 h or 96 h PI) were extrapolated from the decay corrected SPECT images acquired at 24 h and 120 h or 168 h PI, respectively. The exception was the 3rd cycle of patient #6, in which only one SPECT image was acquired 1 h PI. In this case, activity distribution at 12 h PI was extrapolated from this scan. The first 12 h PI were not considered as this period is characterized by an unpredictable pattern behavior related to the initial phase of renal clearance [120]. Therefore, we chose to focus on the slower elimination phase, that comprises more than 70% of the total accumulated activity [121].

4.7.1. Voxel S-value based Dosimetry

The set of VSVs previously validated and the time-integrated activity distributions given by the SPECT scans were used to calculate the patient-specific 3D absorbed dose distributions following the VSV approach, implemented with an in-house MATLAB routine. Since the VSVs datasets were provided for only one octant, values for the remaining octants were determined by invoking symmetry arguments. The 3D accumulated activity distributions were convolved with the pre-calculated ^{177}Lu VSVs, for soft-tissue and 2.21 mm cubic voxels, to determine the absorbed dose distributions (according to Eq. (3.12) of Section 3.6.4), under the assumption of uniform medium (i.e., soft tissue). Thus, an internal function

of MATLAB that enables the computation of N-dimensional convolution was used. 3D convolution was performed, returning the absorbed dose image, which has the same dimensions as the accumulated activity matrix,

$$C(i,j,k) = A(i,j,k) \otimes B(i,j,k) = \sum_{i\prime}\sum_{j\prime}\sum_{k\prime}[A(i',j',k') \cdot B(i-i',j-j',k-k')] \quad (4.20)$$

where A and B represent, respectively, the accumulated activity map and the VSVs kernel. In order to assess the impact of dead time losses of SPECT images in absorbed dose, calculations were repeated using the dead time uncorrected SPECT scans. As this method depends only on the VSVs kernel and activity distribution, so does its uncertainty. Therefore, VSV-based dosimetry was herein performed with a maximum uncertainty not lower than 10% (i.e., maximum statistical uncertainty of the VSVs).

4.7.2. Monte Carlo based Dosimetry

A more complex digital model for ^{177}Lu was implemented to simulate absorbed dose distributions using patient data. Pharmacokinetic data (i.e., accumulated activity distribution) gives information about the number of decays in each voxel. Both accumulated activity maps and patient CT scans were used to determine the absorbed dose spatial distribution by MC simulations.

4.7.2.1. TOPAS Extension to Read Activity Distribution from SPECT and PET

A new routine for TOPAS-MC was developed using Visual Studio Code v1.54.3 (Microsoft Corporation, United States), to use the information from functional images to simulate events that reproduce the realistic biodistribution of the tracer within the patient. To this date, TOPAS-MC did not support this feature. The rationale is that the information given by the SPECT and PET scans is used to define the distribution of the radiation source position in a proportional manner to the voxels' intensity (e.g., number of events).

The algorithm uses the functional data, given by the DICOM images, converted into a text file in MATLAB to be imported to TOPAS. This text file must contain the size (in mm) and number of voxels in each dimension and their intensity values. Particle position is generated using the inverse transform method applied to a discrete distribution of stochastic variables, x_i (i = 1, …, N), which can be the number of arbitrary counts in the scans that is related with the number of 208 keV photons emitted in a specific time period, with a probability distribution, p_i. The SPECT or PET intensity data is read as a vector with Nx × Ny × Nz elements (i.e., total number of elements in the original 3D matrices, where Nx, Ny and Nz are, respectively, the number of elements in x, y and z). The vector values (i.e., intensity data) are normalized to the total number of counts, and the cumulative probability discrete function is computed for each voxel (Eqs. (4.21) and (4.22)).

$$P_j = p_j + p_{j-1} + \cdots + p_1 \; if \; x_{j-1} \leq x < x_j \quad (4.21)$$

$$P_n = p_n + p_{n-1} + \cdots + p_1 = 1 \quad (4.22)$$

$$j,n = 1,\ldots,Nx + Ny + Nz$$

where x represents the voxel's unidimensional index. Using Geant4's default random number generator (HepJamesRandom engine), a random number ξ uniformly distributed in the interval (0,1) is generated ($\xi \rightarrow$ U(0,1)). This value is searched for in the cumulative probability vector, using the binary search algorithm (see next section). The distribution of x is obtained through the condition

$$X = x_j \; if \; P_{j-1} < \xi \leq P_j, j \neq 1\,. \quad (4.23)$$

Voxels with higher intensity values will be selected more often, such that the particle source's position is sampled proportionally to the number of decays in the voxels with respect to the total number of events in the image. The index of the voxel whose value is equal to ξ corresponds to a voxel at a certain position in the original 3D image. Thus, the original 3D coordinates are determined to obtain the spatial position of the particle. Within the selected voxel, the coordinates are sampled randomly and uniformly in each of the three dimensions. To avoid stuck particles in the voxels' boundaries (and lost steps), particularly when these define the transition between two different media, an offset can be considered so that the sampling region within the voxel is smaller than its actual extent (i.e., exclusion of the borders). A new set of coordinates that defines the particle's position is generated in each event.

This extension supports the simultaneous spatial translation of the phantom and voxelized source (e.g., to the coordinates defined in the DICOM header). However, no implementations regarding rotation were included. To be in agreement with TOPAS-MC placement of volumes in the spatial system, a translation equal to half the size of the source volume, in the negative direction, was applied to the emission distribution. Therefore, by default, the voxelized source is placed centered at the spatial system, being automatically aligned with a phantom or patient (i.e., specification of null translation in the parameter file for both volumes).

4.7.2.1.1. Binary Search Algorithm

The generated random number (key element) is searched for in the cumulative probability array (i.e., sorted array), using an adaptation of the binary search algorithm. The index of the middle voxel of the array is selected as the partitioning element. This is used in a pairwise comparison made to check whether ξ is equal, higher (a) or lower (b) than the partitioning element (Figure 4.9).

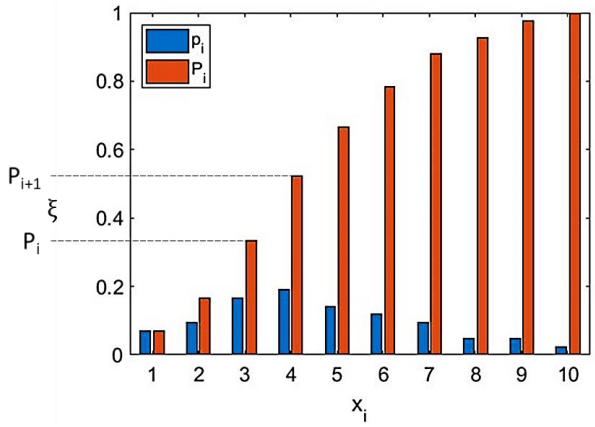

Figure 4.9. Example of the behavior of the implemented search algorithm to find the voxel in which the generated random number, ξ, is included. The integrated array values are represented in orange and the original array is shown in blue. If ξ has no direct correspondence in *x*, being between two values, it is considered to fall in the voxel of the immediately upper value.

If the values match, the position of the middle element in the array is returned. If the elements are not equal, the initial array is partitioned in two subarrays, with reference to the middle index. If condition (a) is verified, the lower half of the array is discarded. Contrary, if condition (b) is true, the upper half of the array is rejected. The process (comparison of key with middle element) is repeated for the remaining subarray, half of the original size, and it continues progressively until the key element, with the same value as ξ, is found. If ξ has no direct correspondence in the array, standing between two values, it is considered to fall in the voxel of the immediately upper value.

4.7.2.2. TOPAS-MC Simulations

Patient-specific MC dosimetry was performed using TOPAS-MC v3.6.1 package, based on Geant4 v10.06.p01. No variance reduction techniques were applied. Particle interactions were simulated with

the same physics modules used for the VSVs computation. The complete radioactive decay of the emitting source (^{177}Lu) was simulated using the G4RadioactiveDecayPhysics and G4Decay modules. All electromagnetic interactions were simulated using Geant4's standard EM physics package (G4EMStandardPhysics_option4). Fluorescence, PIXE and Auger electron emission was also enabled. A cutoff of 0.05 mm was set to all radiation and particles.

The simulations were based on patient data. TOPAS allows the use of CT scans in DICOM format. To reduce simulation time, the CT images were cropped to the same dimensions as the accumulated activity distributions using Slicer. This CT scan is converted into a logical volume to define a voxelized anthropomorphic phantom that reproduces the actual patient anatomy (Figure 4.10). TOPAS provides a built-in converter that assigns different materials to the CT structures according to Schneider's calibration of Hounsfield Units (HU) [122], to provide accurate attenuation maps. The converter assigns 26 different material compositions to each voxel of the phantom and scales the density to achieve an equivalent stopping power as described by the HU, reproducing tissue heterogeneity.

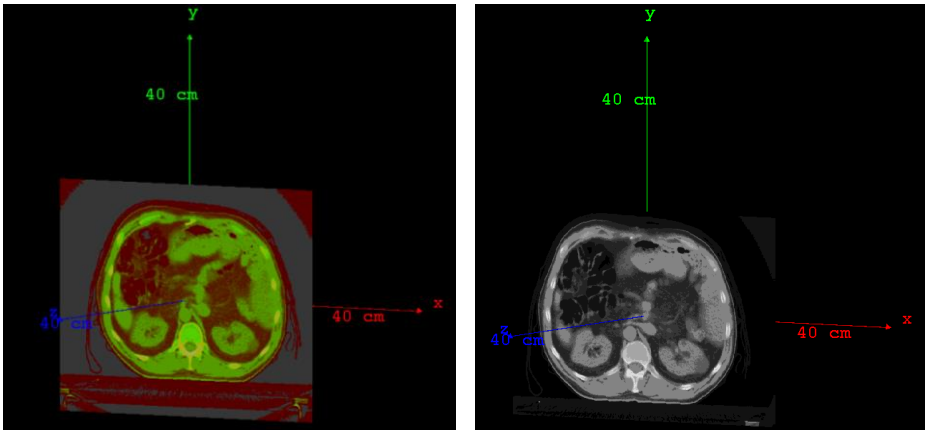

Figure 4.10. OpenGL visualization of the setup of a TOPAS-MC simulation of ^{177}Lu-DOTATATE distribution within a patient. Only a single slice of the voxelized phantom is shown. CT materials are shown in different colors (in the left, default colormap in TOPAS HU to material converter, in the right, conventional grayscale) according to their HU value.

The accumulated activity distributions, given by the clinical co-registered SPECT data, were converted to text files in MATLAB and used to define the radiotracer's spatial distribution (i.e., decay probability map within the patient), employing the extension developed in this work. In this case, the accumulated activity maps were normalized to the total number of decays and were simulated with the CT scan of the same therapy cycle or the available post-therapy CT image. Both the anthropomorphic phantom and radioactive source volumes were centered in the TOPAS spatial reference system. The particles, ^{177}Lu atoms at rest, were sampled randomly within the patient but according to the activity distribution.

Using a number of events equal to the actual number of disintegrations is not feasible as it requires a high calculation time. Therefore, simulations were performed using 10^8 events. Voxel-level statistical uncertainties were typically kept below 0.2%. Each event corresponds to one full decay of ^{177}Lu, including multiple primary particles. The absorbed dose (i.e., dose-to-medium in TOPAS-MC) due to all primary and secondary particles was scored at the voxel-level on a grid overlaid on top of the voxelized phantom, using the HU-material conversion table. The grid, with 2.21 mm cubic voxels and same dimension as the phantom, was a parallel geometry with coarser resolution than the CT scan to avoid memory faults. From the simulations we obtained 3D absorbed dose maps (Gy/event), covering all the CT scan. In MATLAB, the maps were scaled to the actual number of decays, according to

$$D^{i,j,k}(Gy) = D^{i,j,k}(Gy/event) \times \tilde{A}_{SPECT\ FOV}(event) \tag{4.24}$$

where $D^{i,j,k}$ corresponds to the absorbed dose estimated in each voxel and $\tilde{A}_{SPECT\ FOV}$ to the estimated total number of disintegrations in the image's FOV (i.e., total accumulated activity).

4.7.3. Dosimetry Analysis

A dosimetry analysis was performed for the liver, kidneys, spleen, bone marrow, NETs and tumor-healthy tissue interface. VSV and MC voxel-wise absorbed dose distributions were processed to determine the organ and tumor mean absorbed dose values. cDVHs were computed for each VOI, using the SlicerRT extension, and were used to perform a qualitative analysis of the absorbed dose maps. For each patient, mean absorbed dose estimates were normalized to the injected activity (D/A_{inj}) of ^{177}Lu-DOTATATE and presented in Gy/GBq. In addition, kidney and bone marrow toxicity was assessed.

4.8. Pre-treatment Dosimetry

The dosimetry methodology previously described was reproduced using the pre-therapeutic ^{68}Ga-DOTANOC PET/CT scans to evaluate the possibility of treatment planning in PRRT. Since the half-life of ^{68}Ga is very short compared to ^{177}Lu, ^{68}Ga-labeled peptides quantitative imaging cannot be directly used to predict absorbed dose in ^{177}Lu-DOTATATE PRRT [99]. Thus, in both dosimetry methods, the expected absorbed dose distributions were estimated by "replacing" ^{68}Ga with ^{177}Lu as the dose-contributing radionuclide. This methodology was possible because this was a retrospective study, and the activity injected to each patient was known. That is, the distribution of ^{68}Ga was assumed to be ^{177}Lu with the net injected activity known from the treatment of each patient. Therefore, PET scans, originally calibrated in Bq/mL of ^{68}Ga-DOTANOC, were calibrated to ^{177}Lu of total accumulated activity extrapolated from the quantitative SPECT scans of the first treatment cycle, determined as mentioned in the previous section. In both methods, the time-integrated activity distributions given by the clinical PET data was used to define ^{177}Lu-DOTATATE's spatial distribution. In the VSV method, these maps were convolved with the ^{177}Lu VSVs kernel of soft tissue and 2.21 mm cubic voxels. In TOPAS-MC, these determined the decay probability map of ^{177}Lu within the patient and were simulated with the respective pre-therapeutic CT scan. A dosimetry analysis was also performed for the liver, kidneys, spleen, bone marrow and NETs. VSV and MC voxel-wise absorbed dose distributions were processed to determine the mean absorbed dose and compute cDVHs for each VOI.

4.9. Statistical Analysis

Statistical analysis was performed with MATLAB R2018a statistics toolbox. Graphic representation of boxplots and scatter plots was carried out using the Prism v9.0.0 software (GraphPad Software Inc., San Diego, CA). Descriptive statistics was used to report measures of tendency and variability for the effective half-lives and mean absorbed dose estimates. Data was presented as mean ± standard deviation (SD) or median and range. In the presented boxplots, outliers were defined as values below or above $Q1 - 1.5 \times IQ$ and $Q3 + 1.5 \times IQ$, respectively. Q1 is the 25th percentile, Q3 is the 75th percentile and IQ the interquartile range. Sample size is reported as *n*. The determination coefficient, R^2, was used to evaluated the goodness of the exponential fits to the TACs. The agreement between organ and NETs mean absorbed dose estimated by VSV dosimetry and TOPAS-MC simulations was assessed using the intraclass correlation coefficient (ICC) for absolute agreement (two-way mixed effects, single measure). The ICC was computed using an open-source function available in [123]. The relative difference (RD) between VSV and MC mean absorbed dose values was determined for each VOI according to

$$RD = \frac{D^{VSV} - D^{MC}}{D^{MC}} \times 100\,. \tag{4.25}$$

TOPAS-MC data was arbitrarily considered as the reference. Bland-Altman analysis was used to evaluate the agreement of absorbed dose values, obtained by VSV and MC, at the tumor – healthy tissue interface, in terms of mean.

Apart from the tumor-healthy tissue interface analysis, the same statistical analysis was performed to compare the agreement of the predicted absorbed dose distributions, estimated with the pre-therapeutic ^{68}Ga-DOTANOC PET/CT distribution patterns, with the actual absorbed dose distribution, given by the ^{177}Lu-DOTATATE SPECT scans in the first therapy cycle. Herein, SPECT data was considered the reference. In general, for statistical inference, a significance level of 5% was considered.

Chapter 5

Results

In this chapter, the results obtained in this study are presented. Twenty-four treatments from six patients (4 treatment cycles/patient) with histologically confirmed inoperable and/or metastatic NETs over-expressing SSTR, who underwent ^{177}Lu-DOTATATE PRRT, were retrospectively analyzed. Individual characteristics of the patients are presented in Table 4.1 (Section 4.1). At the time of the first treatment cycle, the average age was 61.2 (SD = 8.9) years. A mean activity of 7.2 (SD = 0.5) GBq/cycle of ^{177}Lu-DOTATATE was administered. After injection, two SPECT (24 h and 120 h or 168 h PI) and one CT acquisitions (24 h PI) of the abdominal region were performed. The reconstructed and corrected SPECT scans were calibrated using the CF_{SPECT} determined in phantom studies. These images and the ^{68}Ga PET/CT scans were then used for voxel-wise absorbed dose quantification using two methods, convolution with pre-calculated VSVs and TOPAS-MC simulations. Biokinetic and dosimetry analysis was focused on critical organs and NETs.

5.1. Dead Time and SPECT Calibration Factor

To account for dead time losses, the SPECT system was assumed to behave according to Sorenson's paralyzable model. Five SPECT acquisitions of the NEMA phantom, performed over a 7-day period, and the decaying source method were used to estimate the camera's dead time. The model was fitted to the data with a determination coefficient, R^2, of 0.99, which suggests a good fit. The extrapolated paralyzable dead time constant was 0.122 ± 0.007 μs. The relation between the observed and true count rates, for the 208 keV photopeak of ^{177}Lu, is illustrated in Figure 5.1. According to the curve, the maximum theoretical count rate detected by the camera is estimated to be approximately 3000 kcps.

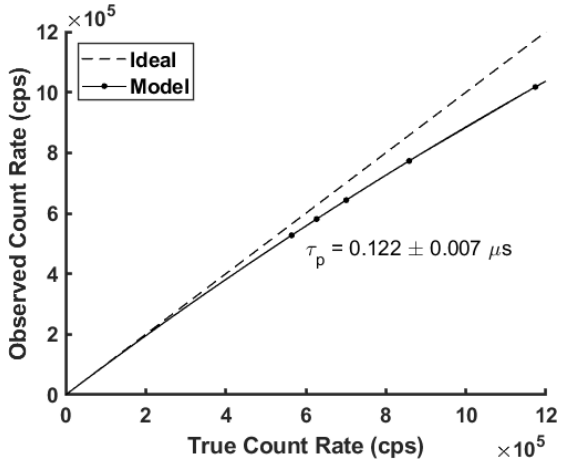

Figure 5.1. Observed count rate as a function of the true count rate for the 208 keV photopeak. The dashed line represents de ideal model (i.e., no count losses) and the fit of the Sorenson's paralyzable model to the data is displayed by the solid line.

In phantom studies, count losses ranged from 6.6% up to 13.3%, with an average of 9.1%. Regarding patient scans, average dead time losses of 4.1% (min = 0.4%, max = 10.1%), 2.5% (0.6%, 7.1%) and 1.6% (0.4%, 3.9%) were found for the SPECT images acquired 24 h (n = 23), 120 h (n = 7) and 168 h (n = 10) PI, respectively (Table 5.1). These values are lower than those found in the phantom studies as lower activities were in the patients at the time of imaging, compared to those in the phantom, due to biological elimination of the tracer. In general, higher dead time losses were seen for the scans acquired 24 h PI, which was expected since these presented a higher count rate (i.e., higher percentage injected activity). Count losses decreased as the tracer was cleared from the body.

Table 5.1. Percentage dead time losses on clinical SPECT scans at the three time points.

	Sample Size (# of scans)	**Median [range]**	**Mean (SD)**
Dead Time Losses (%)			
SPECT 24 h PI	23	2.94 [0.37 – 10.1]	4.07 (2.73)
SPECT 120 h PI	7	0.87 [0.61 – 7.12]	2.49 (2.60)
SPECT 168 h PI	10	1.16 [0.43 – 3.91]	1.59 (1.30)

The 3D calibration factor, CF, was also determined using the five phantom SPECT scans properly processed (i.e., resampled to 2.21 mm cubic voxels). The final CF_{SPECT} was $(436.1 \pm 0.6) \times 10^{-6}$ MBq/cps (approximately 2293 cps/MBq), which was the average value of five CFs (i.e., one CF for each scan), computed using activities ranging from 2.3 to 4.8 GBq.

5.2. Image-based Biodistribution of ^{177}Lu-DOTATATE

Quantitative analysis of WB planar scans was performed for all treatment cycles of all patients except for those who did not meet the imaging requirements needed in this retrospective work (i.e., at least four and three planar acquisitions, respectively, for WB and VOI analysis). For each patient, the activity in the WB at each instant was determined and normalized to the injected activity. Figure 5.2 shows the typical TAC of the WB activity and a bi-exponential model applied to fit the data. A good fit was achieved for all datasets, with a minimum determination coefficient of 0.98.

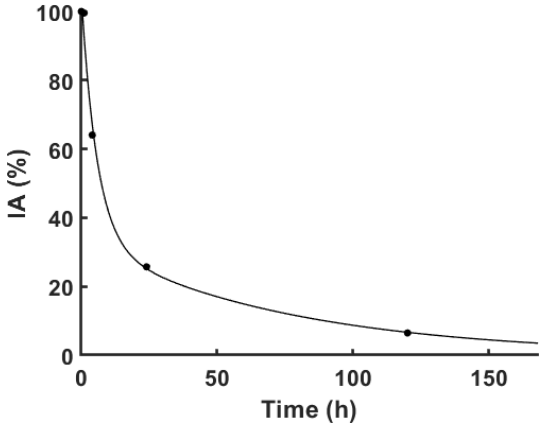

Figure 5.2. Typical WB TAC of a patient who underwent ^{177}Lu-DOTATATE PRRT (first treatment cycle of patient #1), up to 168 h PI. The pharmacokinetic data was obtained from serial post-therapeutic planar WB scans. Activity at each time point is presented as a percentage of the injected activity. Two phases (earlier and later) describe the clearance of the radiotracer from the body.

The two clearance phases of the tracer were seen. The mean effective half-life (SD) for the fast (i.e., earlier) and slow (i.e., later) clearance phases were, respectively, 4.02 (0.79) h and 72.6 (20.9) h. Figure 5.4 shows the inter-patient variability of the WB effective half-life estimates (n = 12 cycles).

The time-dependent retention of ^{177}Lu-DOTATATE in the WB of patients who underwent PRRT is presented in Table 5.2. A decreasing tendency of the retained activity was seen. The majority of the tracer is cleared within the first 24 h PI, with a retention of approximately 32.2%. The results show an average retention of less than 20% of the total injected activity remaining in the body at approximately 120 h PI and around 8.5% at 168 h PI.

Table 5.2. Percentage retention values of ^{177}Lu-DOTATATE at the time of each post-therapy WB planar image acquisition. Values are presented as mean ± SD (range).

Post-therapy Scan Time (h)	**^{177}Lu-DOTATATE Retention (%)**
1	99.6
4	66.5 ± 9.8 (51.8 – 88.9)
24	32.2 ± 14.9 (17.8 – 69.0)
120	17.8 ± 13.6 (5.5 – 30.6)
168	8.5 ± 7.4 (3.0 – 25.5)

The tracer kinetics in the liver, kidneys, spleen and NETs for three of the six patients included in the cohort are shown in Figure 5.3. The curves for the other patients are presented in Figure D.1 of Appendix D. As mentioned, data is only presented for cycles with more than three planar acquisitions (n = 19 cycles). Thus, patient #5 and the 3rd cycle of patient #6 were excluded from the analysis as only two acquisitions were performed. These curves exhibit similar behavior to that of the WB in Figure 5.2, with a decrease in retained activity after uptake. Significant inter-patient and inter-cycle variability concerning curve shape and amplitude was observed. The highest radiotracer accumulation was found in the liver, followed by the NETs in cases of high tumor burden. Patients #2 and #4 presented a delayed uptake. Liver and NETs depicted this phase between 4 h and 24 h PI, followed by the clearance period. This was also seen in the right kidney of patient #2. However, it was assumed that the accumulation was related to cross-irradiation from the liver rather than uptake from the right kidney. Regarding maximum accumulation, the NETs and liver of patient #2 reached a maximum activity at roughly the same instant. Contrary, NETs of patient #4 showed a slower uptake than the liver. No uptakes were observed in other organs.

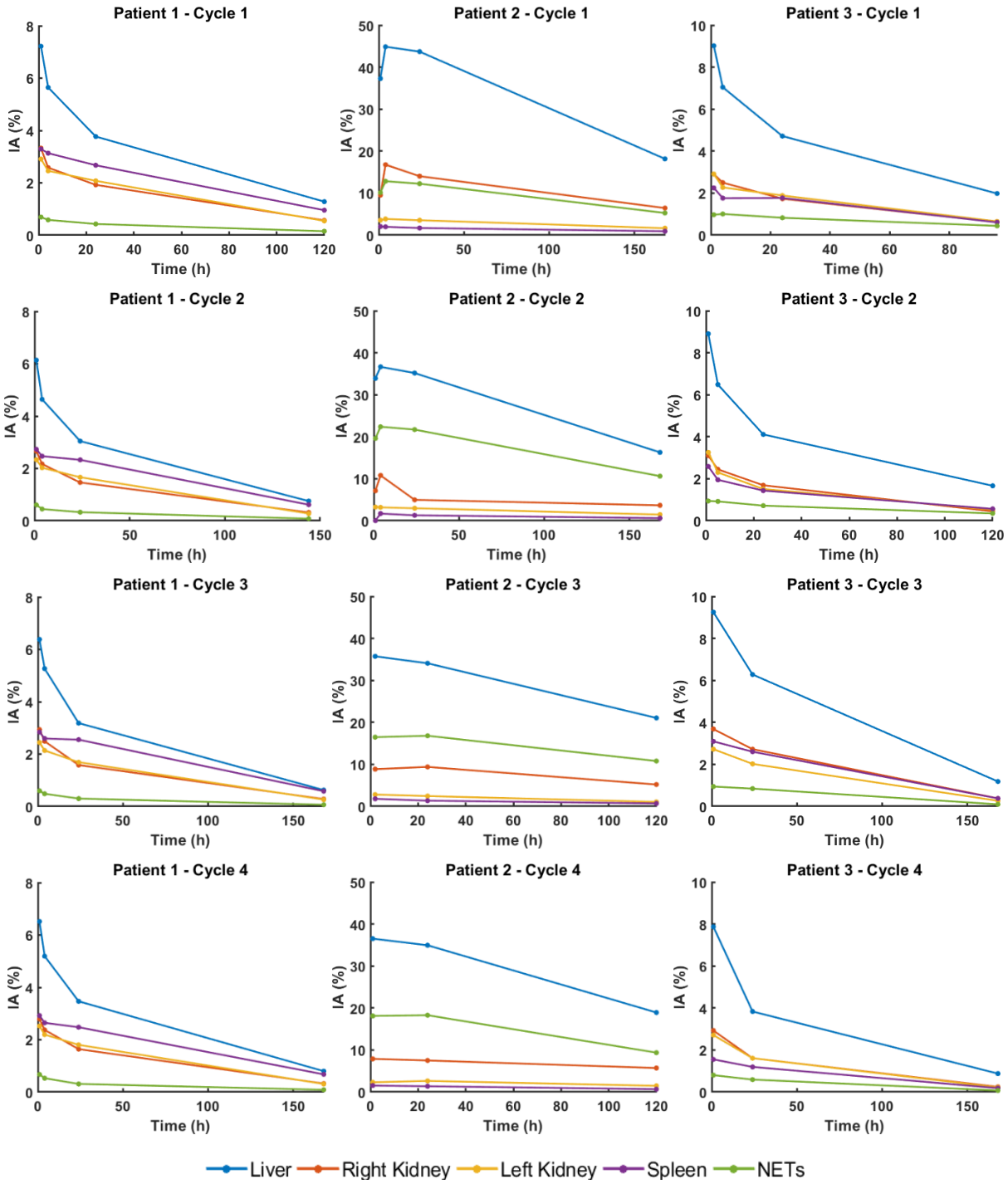

Figure 5.3. Time-activity data for the liver, kidneys, spleen and NETs of three of the six patients included in this study (patients #1, #2 and #3). The lines are for guidance purposes only as no fit to the data is presented. The uptake phase is not clear in all curves due to the absence of quantitative information in the first hour PI. The data were fitted to mono- or bi-exponential functions to determine the tracer's effective half-life in each VOI. Please note the different scales of injected activity and time.

Similar to the WB, mono and bi-exponential fits were applied to the organ and NETs data, according to the number of acquisitions performed in each cycle. The goodness of the fits was evaluated with the determination coefficient, which presented lower values for the mono-exponential model, suggesting that organ TACs are better described by a bi-exponential process. To investigate differences in tracer kinetics, the effective half-life in the VOIs was extrapolated from the curves. Effective half-lives in VOIs to which the bi-exponential model was applied, were determined for the slow clearance phase to

be comparable with the values inferred from the mono-exponential fits. Figure 5.4 shows the variability of organ and tumor effective half-life estimates.

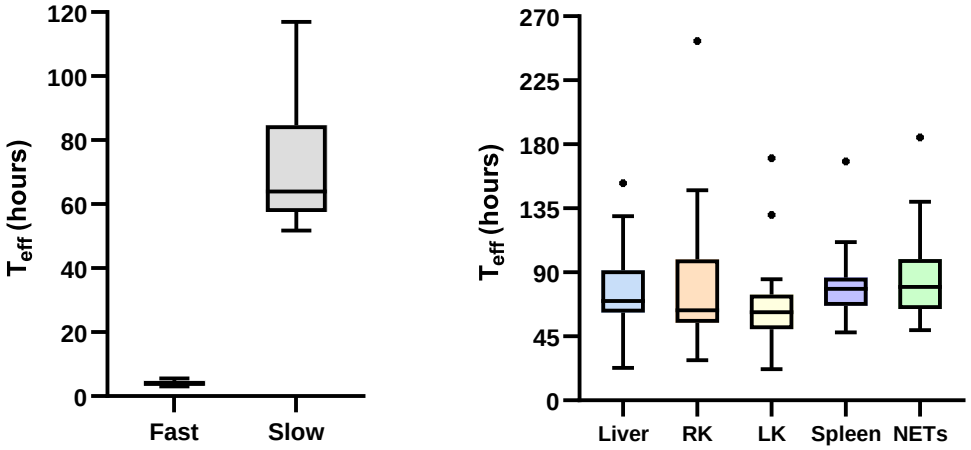

Figure 5.4. Estimated effective half-lives of ^{177}Lu-DOTATATE for the fast and slow WB clearance phases (left panel) and the liver, kidneys (right and left), spleen and NETs (right panel). The boxes comprise values within the 25th and 75th percentiles and the whiskers span to the most extreme data points, excluding outliers, which are shown as individual black dots. The central tick represents the median of the dataset. All values are lower than the physical half-life of ^{177}Lu suggesting that the tracer is eliminated more rapidly by physiologic means. NETs presented the highest tracer retention.

The mean value (SD) of the estimated effective half-live of 79.6 (31.5) h was observed in the liver. The right and left kidneys presented mean values of 81.9 (50.2) h and 67.7 (33.7) h, respectively, while the spleen was found to have a mean value of 80.8 (25.9) h. NETs presented the highest estimates, with a clearance of 88.4 (33.4) h. Effective half-life in the liver and right kidney showed significant inter-patient variability, which is possibly related with different hepatic tumor burden that influences tracer retention. In patient #2, some effective half-life estimates exceeded 90 h, reaching values over 100 h. These cases are represented as outliers. Since the determination of effective half-lives in the WB and VOIs relied exclusively on the TACs, their uncertainty is no less than that of activity (2.5%).

5.3. Voxel S-values Computation

VSVs for two radionuclides (^{177}Lu and ^{68}Ga), voxel sizes (2.21 mm and 4.42 mm) and materials (soft tissue and bone) were computed with TOPAS-MC by simulating the radioactive decay of a uniformly distributed ^{177}Lu source within the central voxel of a voxelized phantom. VSVs are presented as a function of the distance to the central voxel (Figure 5.5 and Figure 5.6). The blue dots and lines correspond to the values found in the literature for ^{177}Lu. As expected, all VSVs decrease with distance, presenting the highest values in the voxels closer to the source. Moreover, VSVs decrease with increasing voxel dimensions due to the integration of deposited energy over a larger mass. For all datasets, the statistical uncertainties increase with the distance to the source.

Energy deposition was mostly focused at the source (central) voxel, reflecting the short range of the charged particles (i.e., electrons and positrons). For instance, regarding soft tissue and 2.21 mm cubic voxels (Figure 5.5 a)), VSVs for the source voxel were 1.86 mGyMBq^{-1}s^{-1} for ^{177}Lu and 2.78 mGyMBq^{-1}s^{-1} for ^{68}Ga. The S-value of the nearest neighbor voxel (centroid to centroid distance of 2.21 mm) was reduced to approximately 2.8% and 19% of the self-dose, respectively, for ^{177}Lu and ^{68}Ga. As to ^{177}Lu VSVs, a significant decrease by approximately 5 orders of magnitude was seen at 4.5 mm from the source voxel. From this point on a clear change in the VSVs is observed, related to a greater contribution of photons to the deposited energy and a negligible influence of the electron component. Similarly, for ^{68}Ga, there was a decrease of around 4 orders of magnitude at approximately 8.5 mm from the source.

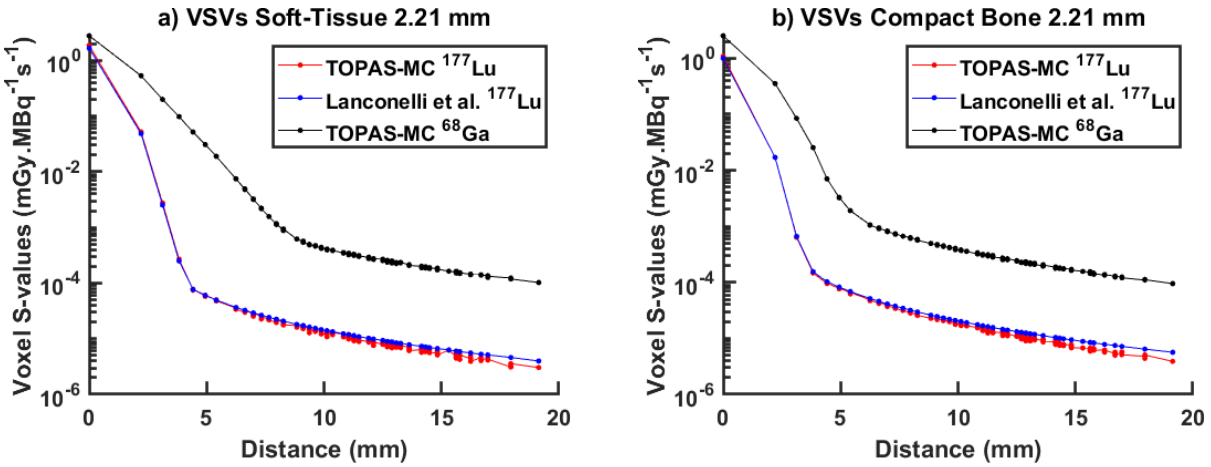

Figure 5.5. VSVs for the β-emitter ^{177}Lu and positron emitter ^{68}Ga, computed in a grid of 2.21 mm cubic voxels of a) soft tissue and b) bone, presented as a function of the distance to the central voxel, in mm. For both radionuclides, VSVs decrease with the distance to the source voxel, where the highest S-value was registered. ^{177}Lu VSVs were compared with the validated data of Lanconelli et al. [94].

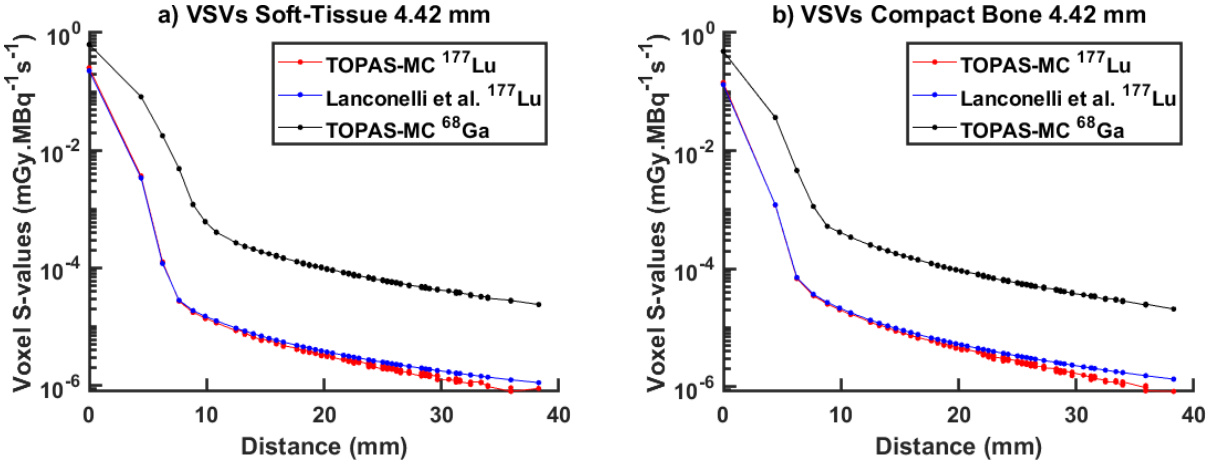

Figure 5.6. VSVs for the β-emitter ^{177}Lu and positron emitter ^{68}Ga, computed in a grid of 4.42 mm cubic voxels of a) soft tissue and b) bone, presented as a function of the distance to the central voxel, in mm. For both radionuclides, VSVs decrease with the distance to the source voxel, where the highest S-value was registered. ^{177}Lu VSVs were compared with the validated data of Lanconelli et al. [94].

The behavior of the VSVs of bone (Figure 5.5 b)) is comparable, but the photon contribution starts at a shorter distance, specifically at about 4 and 6 mm for ^{177}Lu and ^{68}Ga, respectively. This was expected, since the attenuation is higher and the electrons will have a shorter range compared to that of soft tissue. In addition, radionuclides with high-energy photons, such as ^{68}Ga (511 keV photons), have been found to have higher VSVs compared to low-energy β-emitters, such as ^{177}Lu. Overall, this behavior was also observed in the VSVs computed for other voxel dimensions (see Figure 5.6).

The ^{177}Lu VSVs datasets were compared with published data obtained with the EGSnrc MC tool. ^{68}Ga VSVs datasets were not compared with reference values as none were found in the literature for the chosen tissues and voxel sizes. The curves exhibit good agreement on the logarithmic scale, with more significant differences in the region with higher photon contribution to energy deposition (Figure 5.5 and Figure 5.6). Regarding the quantitative assessment, Figure 5.7 shows the percentage RD between our data and the reference values, with respect to [94]. A general reasonable agreement was seen with relative percent errors ranging from -44.5% up to 12% across the two tissues and voxel sizes. The datasets are similar for voxels close to the source, with differences within a few percent, while higher discrepancies are observed for larger distances.

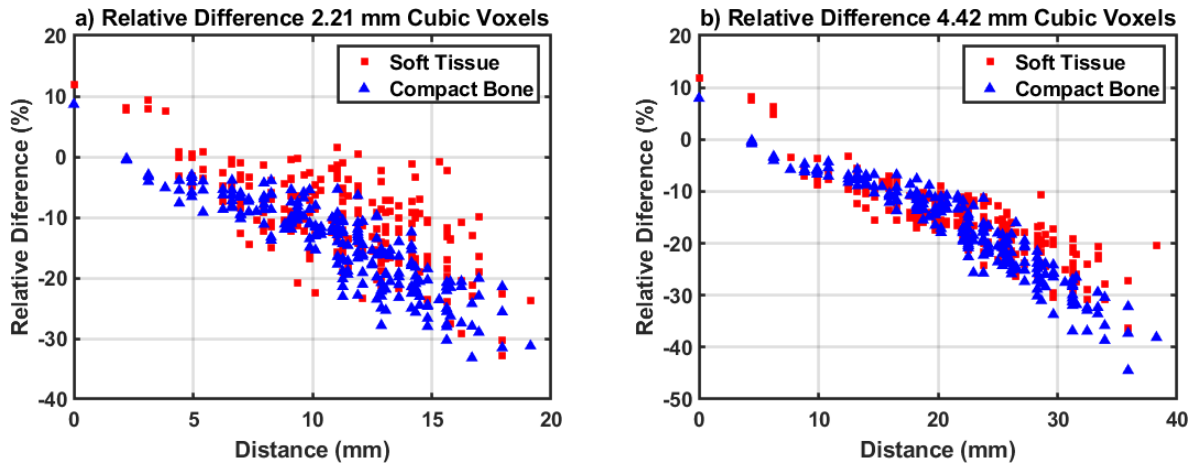

Figure 5.7. RD for ^{177}Lu VSVs in (a) 2.21 mm and (b) 4.42 mm cubic voxels with respect to the reference data [94]. The datasets show a reasonable agreement for voxels closer to the source while higher differences are seen for larger distances. There is a noticeable increase of the RD, in both materials, with the distance to the source voxel.

A comparison between the ^{177}Lu VSVs in specific voxels (i.e., source voxel, nearest neighbor and first diagonal) for both tissues and voxel sizes is presented in Table 5.3. VSVs for the self-irradiating voxel differed from the reference up to 12% and 8.6% in soft tissue and bone, respectively. Regarding voxel size, higher differences were seen for 2.21 mm cubic voxels at the source voxel. VSVs for voxels closer to the source presented similar percentage RD for both voxel sizes. However, at relatively larger distances, 4.42 mm cubic voxels revealed higher discrepancies between the datasets (see Figure 5.7).

Table 5.3. RD values between the VSVs determined in this study and the published data [94] for ^{177}Lu in two different tissues (bone and soft tissue) and voxel sizes (2.21 mm and 4.42 mm cubic voxels) at specific target voxel coordinates (given by the indexes i, j, k).

Target Voxel (i,j,k)	**^{177}Lu Voxel S-values RD (%)**			
	Soft Tissue		**Compact Bone**	
	2.21 mm	**4.42 mm**	**2.21 mm**	**4.42 mm**
(0,0,0)	12%	11.9%	8.6%	7.9%
(0,0,1)[a]	8.1%	7.8%	-0.3%	-0.5%
(1,1,1)[b]	7.5 %	-3.5%	-5.1%	-5.8%

[a] nearest neighbor
[b] first diagonal neighbor

With respect to tissues, greater differences were observed for soft tissue in regions closer to the source. However, VSVs of bone presented higher differences at greater distances (see Figure 5.7). The influence of different tissues in the RD appears to be more significant for small voxel dimensions.

5.4. Voxel-based Dosimetry

Using the quantitative data given by serial post-therapeutic ^{177}Lu-DOTATATE SPECT and pre-therapeutic ^{68}Ga-DOTANOC PET/CT images, patient-specific voxel-wise dosimetry was performed. The aim was to compare the absorbed dose estimated by VSVs and MC simulations. In addition, the main objectives were to assess possible critical organ toxicity and evaluate the possibility of using the ^{68}Ga-DOTANOC distribution in calculating the estimation of absorbed dose distribution during treatment and ultimately estimate the optimal radiation activity to each patient. Organ absorbed dose maps were compared using cDVHs and mean absorbed dose values using the ICC and RD. In general, MC dosimetry entailed a simulation time of approximately 2 days/simulation while the VSV method took less than 1 minute/computation, with the same workstation best described previously in this work.

5.4.1. Post-therapy Dosimetry

Post-therapeutic ^{177}Lu-DOTATATE SPECT scans were used to compute the absorbed dose distribution using two computational approaches. The axial, sagittal and coronal orthogonal projections of the absorbed dose maps of patient #3 after the first PRRT cycle are shown as an example in Figure 5.8, in panels (a-c) obtained with the VSV method and in panels (d-f) with TOPAS-MC. In all patients, physiological uptake of the tracer was noted in the liver, kidneys, spleen and NETs. The highest intensity was seen in the NETs, followed by the liver and spleen.

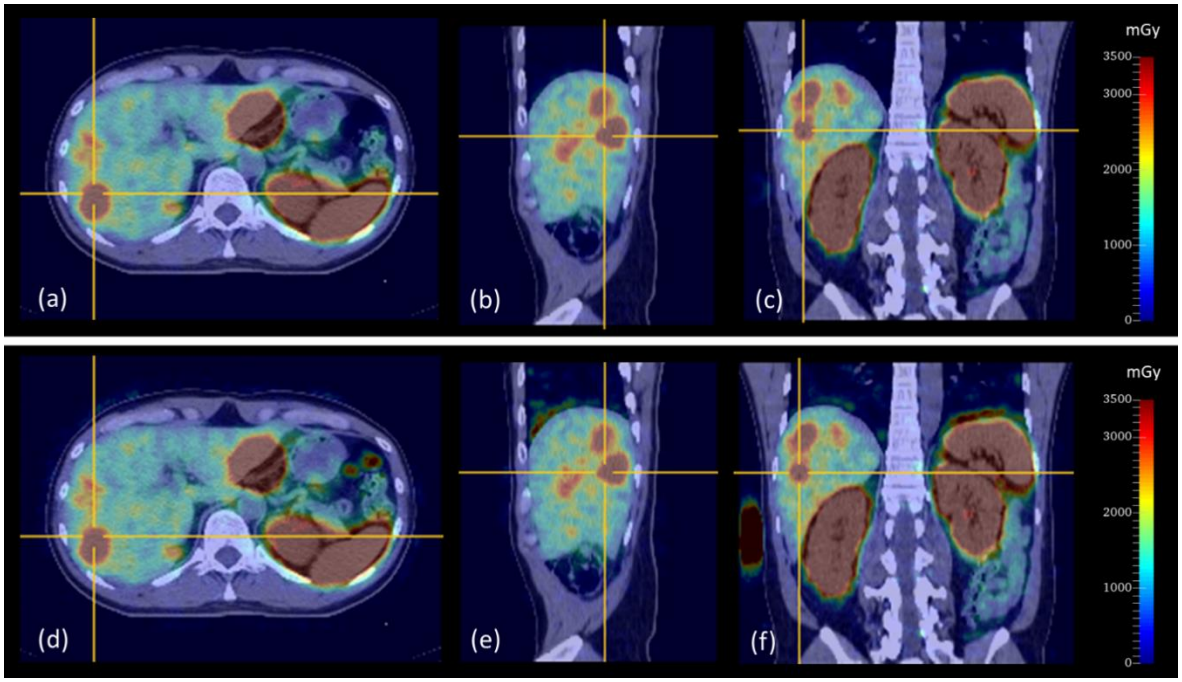

Figure 5.8. (a) axial, (b) sagittal and (c) coronal orthogonal projections of the activity-derived absorbed dose maps of the first therapy cycle of the example patient #3, aligned with the respective CT scan, obtained using VSV dosimetry. The same in (d – f) using TOPAS-MC simulations. The same slices are presented for both methods. The color scale represents the absorbed dose in mGy. All projections are in the same scale. Physiological uptake is noticed in the liver, kidneys, spleen and NETs.

Figure 5.9 shows the mean absorbed dose per injected activity (Gy/GBq) in the liver, kidneys (right and left), spleen, bone marrow and NETs for our patient cohort (n = 6 individuals) and each PRRT cycle, estimated using VSV dosimetry and TOPAS-MC. Mean D/A_{inj} values in the studied organs and NETs, per treatment cycle, obtained for the entire patient cohort are also presented in Tables E.1 and E.2 of Appendix E. Concerning the individual patient data, D/A_{inj} between cycles was reproducible for all organs, except in cases of great tumor burden and close proximity to tumor lesions (e.g., liver of patient #2). This is supported by the great range and SD of D/A_{inj} values. Note that the range of D/A_{inj} estimates in patient #6 reflects the absorbed dose overestimation in the 3rd treatment cycle, due to the use of a single SPECT scan for dose quantification. Moreover, significant intra-patient variability was seen for the NETs D/A_{inj}, followed by the liver, which could be due to different hepatic tumor burden.

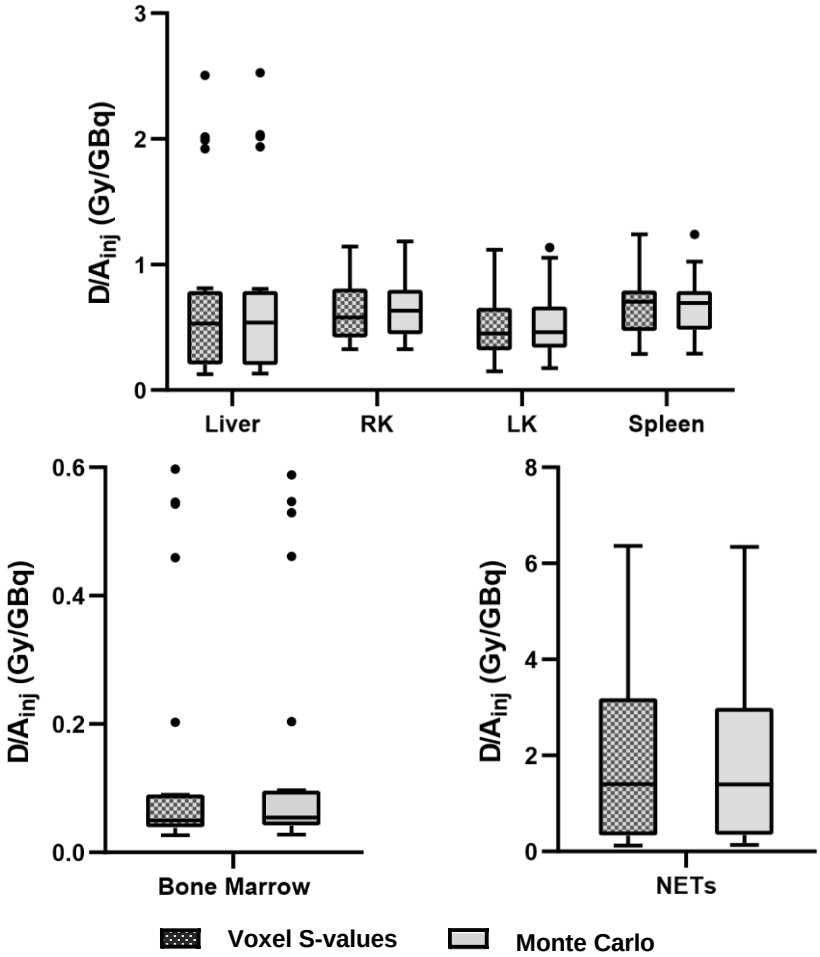

Figure 5.9. Quantification of ^{177}Lu-DOTATATE mean absorbed dose (Gy/GBq) in the liver, right and left kidneys, spleen, bone marrow and NETs estimated by VSV and TOPAS-MC. To facilitate analysis, the data are presented in three graphs with appropriate scales. Patients were injected with a therapeutic radiation activity of 7.2 (SD = 0.5) GBq. Mean absorbed dose estimates of the two groups (VSV and MC) showed a negligible difference (ICC > 0.90). The boxes comprise values within the 25th and 75th percentiles and the whiskers span to the most extreme data points excluding outliers, which are shown as individual black dots. The central tick represents the median of the dataset.

The cDVHs obtained by the two methods for each VOI are presented in Figure 5.10. These represent the typical curves of patients with low (patient #1) and high tumor burden (patient #2). The cDVHs of the remaining patients are presented in Appendix E. VSV and TOPAS-MC show similar absorbed dose distribution in organs and NETs with almost overlapping cDVHs. All curves present the expected appearance, characterized by an initial plateau followed by a sudden or gradual decrease. In patients #1 and #6, the D_{90} (i.e., minimum absorbed dose covering 90% of the volume) for the spleen is higher than that of other organs, meaning that it received the highest doses, followed by the kidneys. For instance, in the first treatment of patient #1, approximately half of the spleen's volume (D_{50}) was exposed to more than 6 Gy, while the D_{50} for the NETs was lower than 2 Gy. Contrary, in the other patients, the NETs were exposed to higher doses. Considerable tumor heterogeneity was seen. In the first cycle of patient #2, approximately 50% of the tumor's volume received a minimum of 35 Gy, with some voxels reaching up to 50 Gy. In addition, half of the liver volume received a minimum dose of approximately 10 Gy, with a maximum of 45 Gy in some voxels. Since liver volume included hepatic lesions, regions with higher absorbed dose values probably correspond to functioning NETs. Moreover, despite the different mean absorbed dose, cDVHs show that right and left kidney dose distribution is quite similar for all patients (i.e., identical slope). Lastly, the bone marrow presented the most uniform absorbed dose distribution.

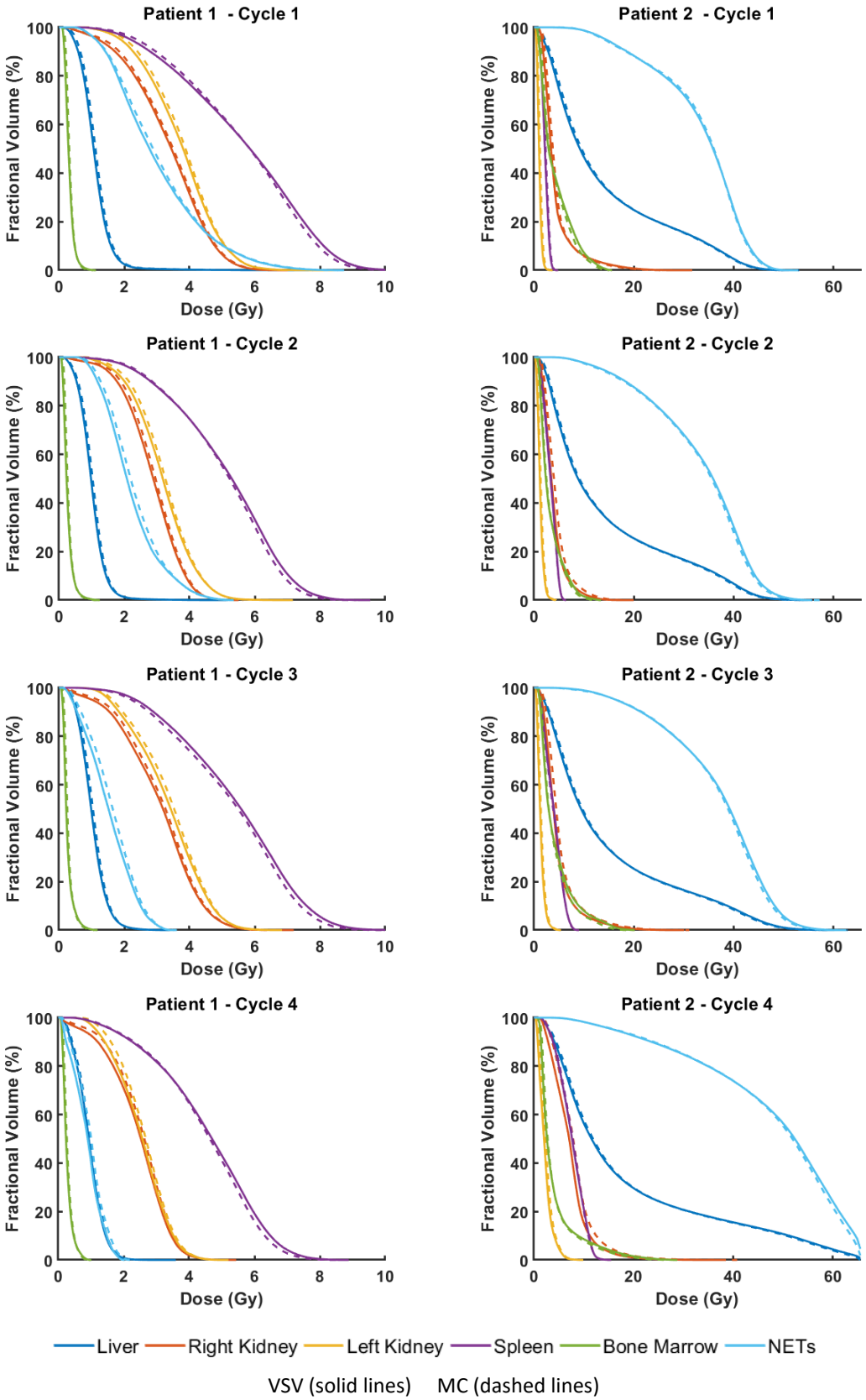

Figure 5.10. Cumulative DVHs computed for the liver, right and left kidneys, spleen, bone marrow and NETs by analysis of the voxel-wise absorbed dose distributions obtained with the VSV (solid lines) and MC (dashed lines) methods for patients #1 and #2. The vertical axis represents the fractional volume that received a minimum absorbed dose. The smaller the slope of the curve, the greater the non-uniformity of the absorbed dose distribution. For each VOI, cDVHs for the two dosimetry methods are almost identical.

Very good agreement (ICC > 0.90) was found between organ absorbed dose distributions obtained with VSV and TOPAS-MC, with similar cDVHs in all VOIs (Figure 5.10). Organ and tumor mean absorbed dose estimated by the two methods was also comparable, with no significant differences. This is supported by the ICC of 1.000, 0.992, 0.998, 0.999, 0.999 and 0.999 obtained, respectively, for the mean absorbed dose in the liver, right kidney, left kidney, spleen, bone marrow and NETs.

Figure 5.11 reports the RD of the mean absorbed dose in organs and NETs estimated by the two methods, for each treatment cycle in our cohort of patients, considering MC as the reference. These differences are most likely due to patient morphology considerations in MC simulations. The highest median RD of -3.6% (min = -25.6%, max = 3.8%) was seen for the bone marrow. The most significant differences (> 17%) were observed for patient #4, which has a great tumor burden, with the VSV method leading to lower mean absorbed dose estimates. In the other patients, the bone marrow RD was found to be below 10%. Liver and NETs presented a similar pattern, with a median RD of -1.0% (-5.5%, 0.7%) and 0.4% (-10.3%, 8.25%), respectively. However, NETs exhibited a wider range. The largest discrepancies were found for patient #1, with the VSV method displaying the lowest values. Right kidney, left kidney and spleen presented median RD of -2.9% (-11.1%, 2.6%), -1.9% (-15.4%, 1.7%) and 0.2% (-4.3%, 4.1%), respectively. The greatest deviations in renal mean absorbed dose were seen for patient #2, with slightly higher discrepancies for the left kidney.

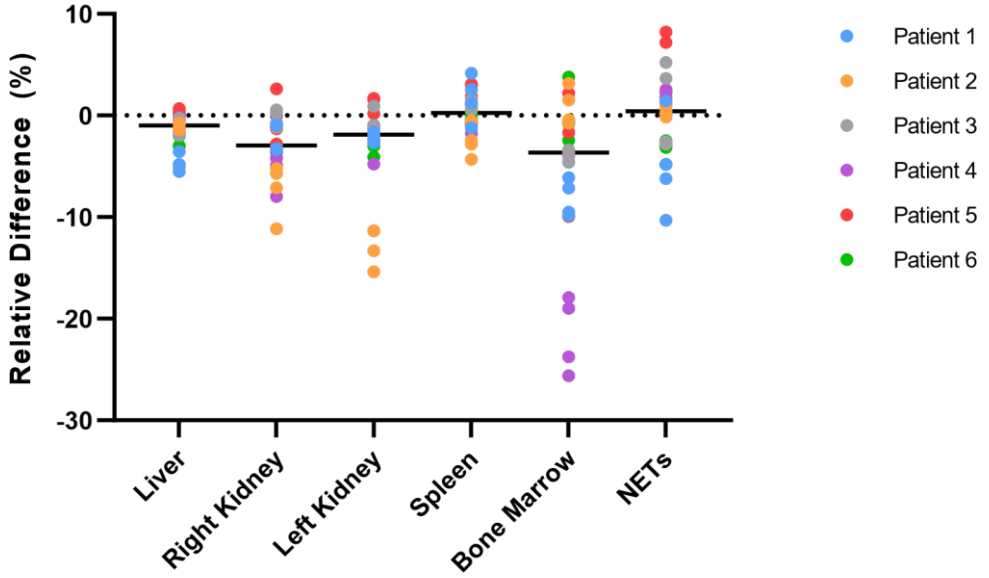

Figure 5.11. Scatter plot of the RD of the mean absorbed dose in organs and NETs estimated by the VSV and MC methods, using sequential post-therapeutic ^{177}Lu-DOTATATE SPECT scans. The black line represents the median RD for each VOI considering all the treatment cycles for each patient. Positive values express the cases in which the mean absorbed dose obtained by MC was lower than that determined by the VSV approach.

Figure 5.12 shows the correlation at the voxel-level, between the absorbed dose values computed by the two methods (VSV and MC) at the interface between the tumors and the healthy tissue, for each patient. The Bland-Altman plots suggest good agreement between the two methods in this interface region. A mean absolute difference close to zero was found for all patients. Voxels with higher absorbed dose presented the greatest differences, which was expected as these are scarce or possible outliers. This observation is supported by the cDVHs in Figure 5.10.

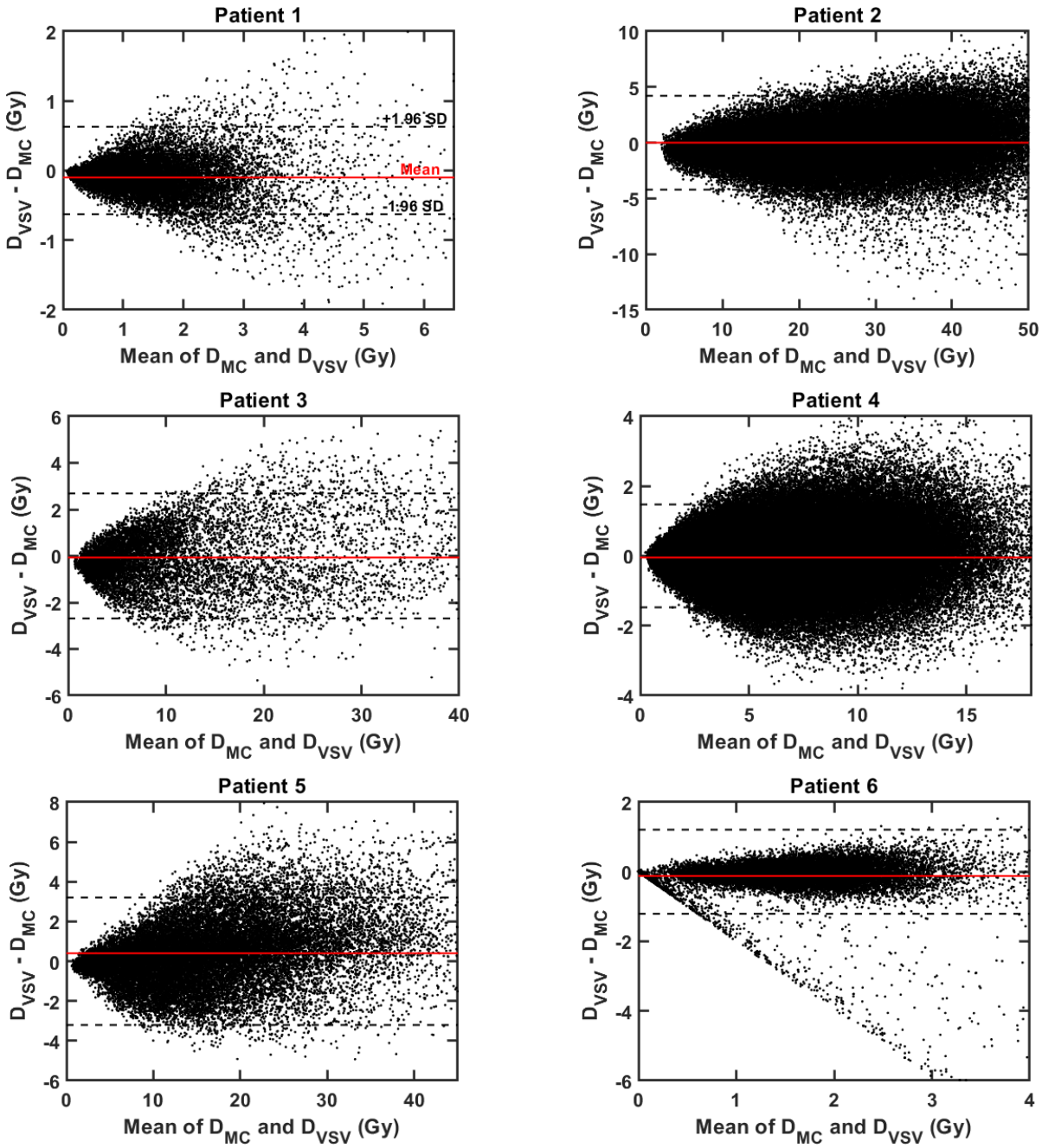

Figure 5.12. Bland-Altman plots of the variability between the absorbed dose values at the NETs and healthy tissue interface, calculated by VSV dosimetry and MC simulations. The plot of each patient included data from all four treatment cycles. The upper and lower dashed lines represent the 95% confidence limit (±1.96×SD). The red line represents the mean absolute difference between absorbed dose measures. Plots were zoomed in for better visualization.

Table 5.4 presents the total absorbed dose (i.e., after all PRRT cycles) in the organs and NETs, estimated by both dosimetry approaches. As expected, the NETs showed the highest average total absorbed dose and inter-patient variability, followed by the liver. Contrary, the lowest total absorbed dose values were seen for the bone marrow.

Table 5.4. Total absorbed dose (Gy) in the organs and NETs, determined using VSV dosimetry and TOPAS-MC simulations, for an injected activity of 7.2 (SD = 0.5) GBq. Values are presented as mean (± SD) [range].

VOI	D_{VSV} (Gy)	D_{MC} (Gy)
Liver	20.0 (± 21.5) [4.0 – 61.8]	20.2 (± 21.7) [4.2 – 62.4]
Right Kidney	17.3 (± 5.1) [11.6 – 24.5]	17.9 (± 5.3) [12.0 – 25.0]
Left Kidney	14.5 (± 6.8) [5.8 – 24.9]	14.8 (± 6.6) [6.6 – 25.1]
Spleen	19.3 (± 4.8) [11.5 – 25.1]	19.2 (± 4.6) [11.6 – 25.0]
Bone Marrow	4.0 (± 5.8) [1.0 – 15.7]	4.1 (± 5.6) [1.2 – 15.6]
Tumors	59.3 (± 55.2) [7.7 – 151.6]	58.4 (± 54.6) [8.0 – 150.9]

The individual total absorbed dose results for the critical organs (i.e., kidneys and bone marrow) and NETs in the patient cohort, determined from the TOPAS-MC absorbed dose distributions, are presented in Figure 5.13. Overall, the absorbed dose across all PRRT cycles did not exhibit a predictable pattern in these VOIs. Values show that, in 50% of the patients, the bone marrow was the absorbed dose limiting organ, with total absorbed dose values exceeding the 2 Gy threshold. On the other hand, only patient #5 reached the renal absorbed dose limit of 23 Gy. Regarding tumor dosimetry, in some patients the mean absorbed dose decreased in later cycles, while in others fluctuations (patient #4) or an increasing pattern (patient #2) were seen. The same findings were seen for the VSV absorbed dose data.

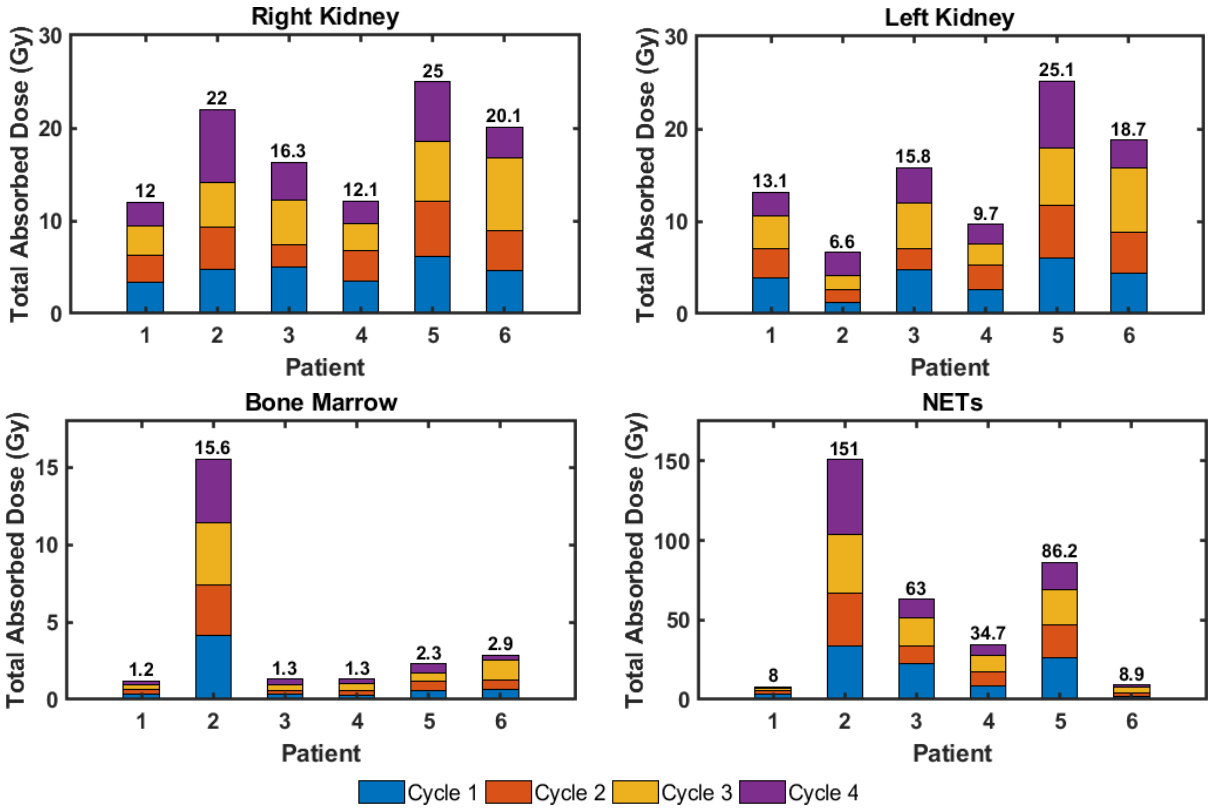

Figure 5.13. Total absorbed dose (Gy) in the right and left kidneys, bone marrow and NETs after all four PRRT cycles, estimated using TOPAS-MC. Values show that the bone marrow was the dose-limiting organ with half of the patients, exceeding the generally accepted absorbed dose threshold. Only one patient reached the renal absorbed dose limit.

Figure 5.14 reports the ratio between dosimetry with the VSVs and TOPAS-MC simulations, considering the total absorbed dose in the organs and NETs of the six patients included in the cohort. The uncertainty of each measure was determined as the uncertainty of the estimated mean absorbed dose value in each VOI (according to $\varepsilon = SD/\sqrt{\#voxels\ in\ VOI}$). There is not a clear tendency in the results, with some organs and NETs receiving a higher total absorbed dose according to TOPAS-MC and vice-versa. Overall, total absorbed doses presented a similar inter-patient variability as the mean absorbed dose estimates per treatment cycle.

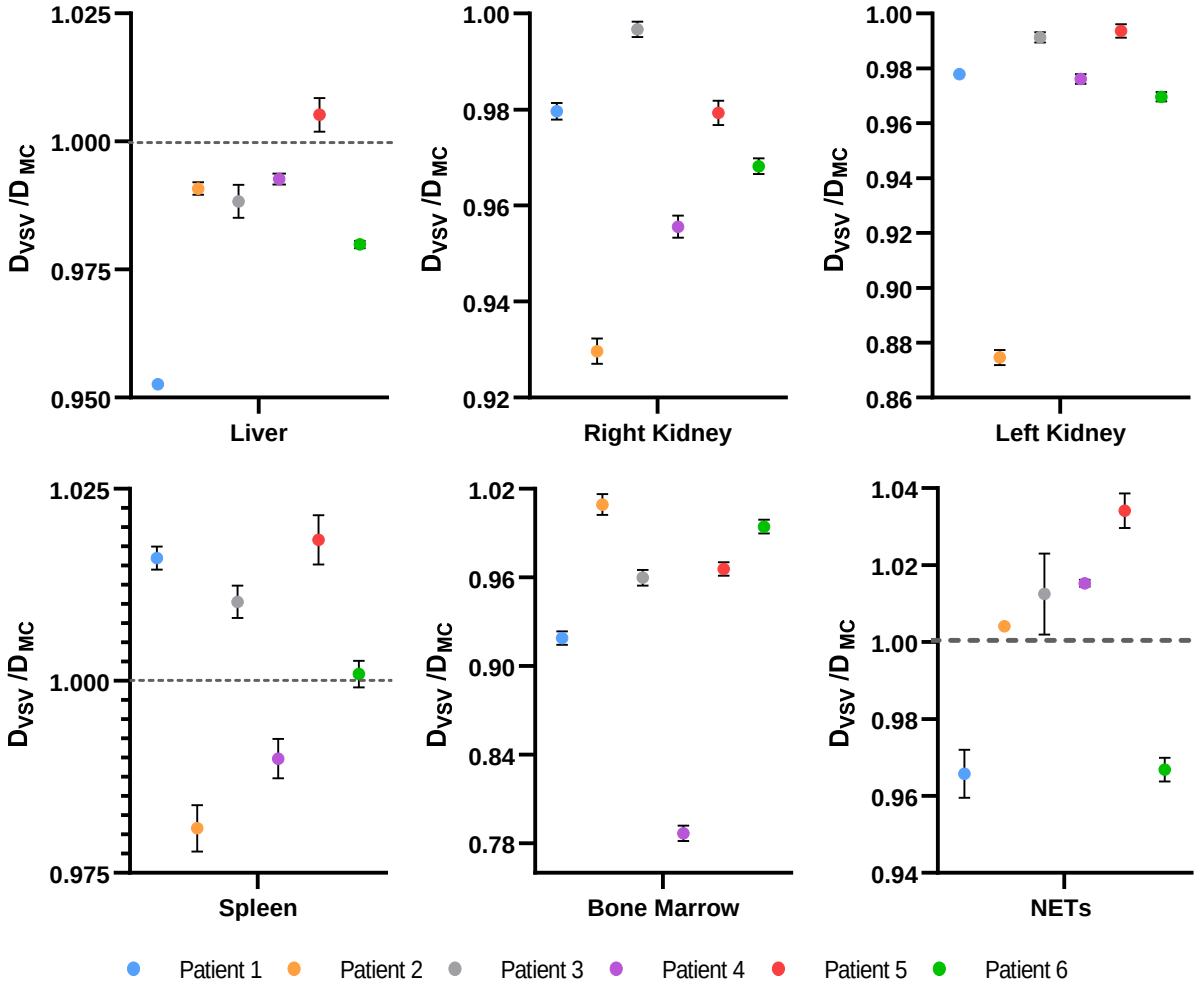

Figure 5.14. Ratio between the organ (i.e., liver, kidneys, spleen and bone marrow) and NETs total absorbed dose, for each of the six patients included in the cohort, estimated by VSV dosimetry and TOPAS-MC simulations using serial post-therapeutic ^{177}Lu-DOTATATE SPECT scans. Error bars smaller than the respective marker are not shown.

The highest median RD was seen for the bone marrow, with -3.7% (-21.3%, 0.9%). Bone marrow total absorbed dose was generally lower with the VSV method, except in patient #2. Deviations were notably high for patient #4, which is in agreement with the previous results. Liver, right and left kidneys, spleen and NETs followed with a median RD of -1.0% (-4.7%, 0.5%), -2.6% (-7.0%, -0.3%), -2.3% (-12.5%, -0.6%), 0.6% (-1.9%, 1.8%) and 0.8% (-3.4%, 3.4%), respectively. Only in patient #5 the VSV method resulted in higher liver total absorbed dose. Contrary, the NETs of four patients showed higher absorbed dose with the VSV approach. The largest differences between the liver and NETs total absorbed dose obtained by the two methods were found for patient #1, as expected. Furthermore, renal total absorbed dose obtained with VSV was always lower than that estimated by MC, with patient #2 presenting the most marked discrepancies, particularly in the left kidney.

The influence of dead time correction in the organ and NETs mean absorbed dose estimates was also assessed. The comparison between the results obtained using the dead time corrected and uncorrected ^{177}Lu SPECT scans is presented in Table 5.5.

Table 5.5. Comparison between the organs and NETs mean absorbed dose, determined with VSV dosimetry, using the dead time corrected and uncorrected ^{177}Lu SPECT scans. Values are presented as median (range).

VOI	Median RD (range) (%)	ICC
Liver	-2.2 (-7.2, -0.7)	0.996
Right Kidney	-2.2 (-7.4, -0.6)	0.992
Left Kidney	-2.3 (-7.6, -0.6)	0.998
Spleen	-2.2 (-7.4, -0.6)	0.993
Bone Marrow	-2.2 (-7.3, -0.9)	0.997
NETs	-2.2 (-6.9, -0.7)	0.997

Differences ranging from -7.6% up to -0.6% were found, with the uncorrected images resulting in an underestimation of mean absorbed dose in all organs and NETs. However, statistical analysis revealed that these values were not significantly different (ICC > 0.99).

5.4.2. Pre-treatment Dosimetry

Absorbed dose calculations with the pre-therapeutic ^{68}Ga-DOTANOC PET/CT scans were performed with both methods (VSV and TOPAS-MC), using the relative tracer distribution captured by the scans and considering ^{177}Lu as the emitting radionuclide (Table 5.6). Although not showing the exact same pattern (i.e., relative biodistribution) as the data obtained using the post-therapeutic ^{177}Lu-DOTATATE SPECT images (Figure 5.15), possibly due to the use of different radiopharmaceuticals and CT scans as the voxelized phantom (i.e., different tissue compositions, detailed discussion in Section 6.4.1), VSV and MC results show good agreement for most organs and NETs (ICC > 0.90).

Table 5.6. Mean absorbed dose (Gy) in the organs and NETs, determined with VSV dosimetry and TOPAS-MC simulations, using the relative tracer biodistribution captured by the pre-therapeutic ^{68}Ga-DOTANOC PET/CT scans. Values are presented as mean (± SD) [range].

VOI	D_{VSV} (Gy)	D_{MC} (Gy)
Liver	3.32 (± 2.96) [1.09 – 9.17]	3.50 (± 3.03) [1.25 – 9.51]
Right Kidney	4.13 (± 2.19) [1.88 – 8.00]	4.27 (± 2.31) [1.96 – 8.40]
Left Kidney	3.20 (± 1.08) [1.89 – 5.06]	3.30 (± 1.04) [2.00 – 5.07]
Spleen	5.36 (± 1.86) [3.89 – 8.79]	6.22 (± 2.74) [3.94 – 10.39]
Bone Marrow	0.91 (± 1.21) [0.09 – 3.32]	0.92 (± 1.17) [0.12 – 3.25]
Tumors	6.18 (± 6.26) [1.11 – 17.66]	6.18 (± 6.26) [1.19 – 17.8]

In general, the MC simulations resulted in slightly higher mean absorbed dose values. Greater inter-patient variability was observed in RD for spleen and bone marrow. The spleen (ICC = 0.846) presented the highest median RD of -8.3% (min = -30.8%, max = 2.5%), followed by the bone marrow and liver

with -5.1% (-24.0%, 2.1%) and -4.6% (-13.2%, -2.2%), respectively. However, these were not statistically significant as an ICC of 0.999 and 0.997 was found for both organs, respectively. In the spleen and bone marrow, the highest deviations were seen for patient #3. Contrary, the kidneys presented the smallest difference range. Both kidneys exhibited a median RD of -3.1%, with the right kidney mean absorbed dose (ICC = 0.997) differing between -4.8% and -0.9% and left kidney mean absorbed dose (ICC = 0.994) between -7.5% and -0.2%. The highest RD values were observed for patient #2, as expected. The lowest difference was seen for the NETs, which presented a median RD of -1.0% (-7.0%, 4.0%) and an ICC of 1.000. Overall, no significant differences were found.

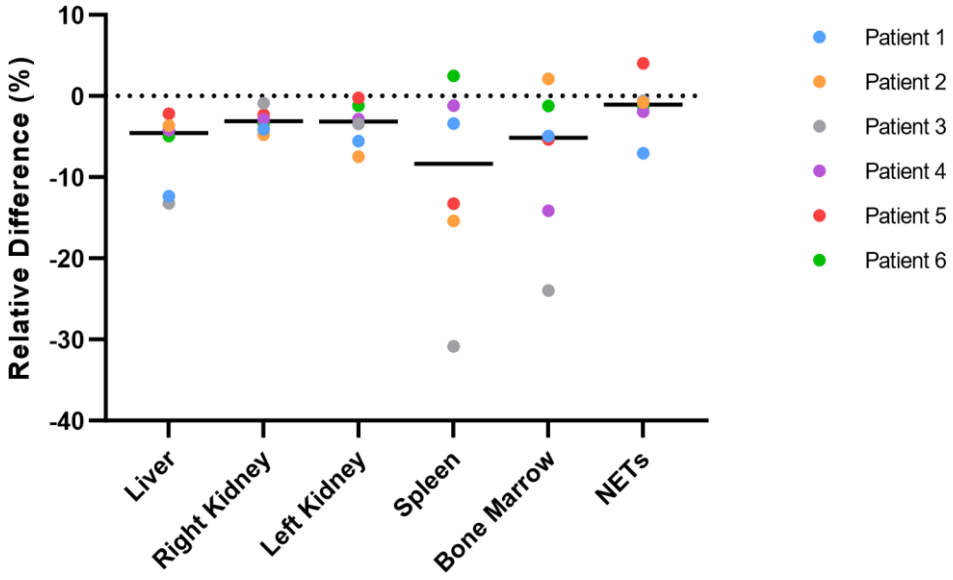

Figure 5.15. Scatter plot of the RD between organ and NETs mean absorbed dose estimated by the VSV and MC methods, using the relative tracer biodistribution captured by the pre-therapeutic ^{68}Ga-DOTANOC PET/CT scans. The black line represents the median RD for each VOI. Positive values express the cases in which the mean absorbed dose obtained by MC simulations was lower than that determined by the VSV approach.

Pre-therapeutic ^{68}Ga-DOTANOC PET/CT scans were used to investigate the feasibility of predicting absorbed dose distribution prior to PRRT. Thus, TOPAS-MC mean absorbed dose estimates were compared with the data determined with the post-therapeutic ^{177}Lu-DOTATATE SPECT images of the first treatment cycle (i.e., predictive vs. measured absorbed dose analysis). Figure 5.16 presents axial, sagittal and coronal orthogonal projections of the voxel-wise absorbed dose distributions of the example patient #3, calculated using in (a-c) ^{177}Lu-DOTATATE SPECT and (d-f) ^{68}Ga-DOTANOC PET/CT scans. Regarding ^{68}Ga-DOTANOC, physiological uptake was seen in the liver, kidneys, spleen and NETs. Tracer biodistribution shows more focal uptake in hepatic lesions with ^{177}Lu-DOTATATE. The spleen was the organ exposed to the highest doses with ^{68}Ga-DOTANOC.

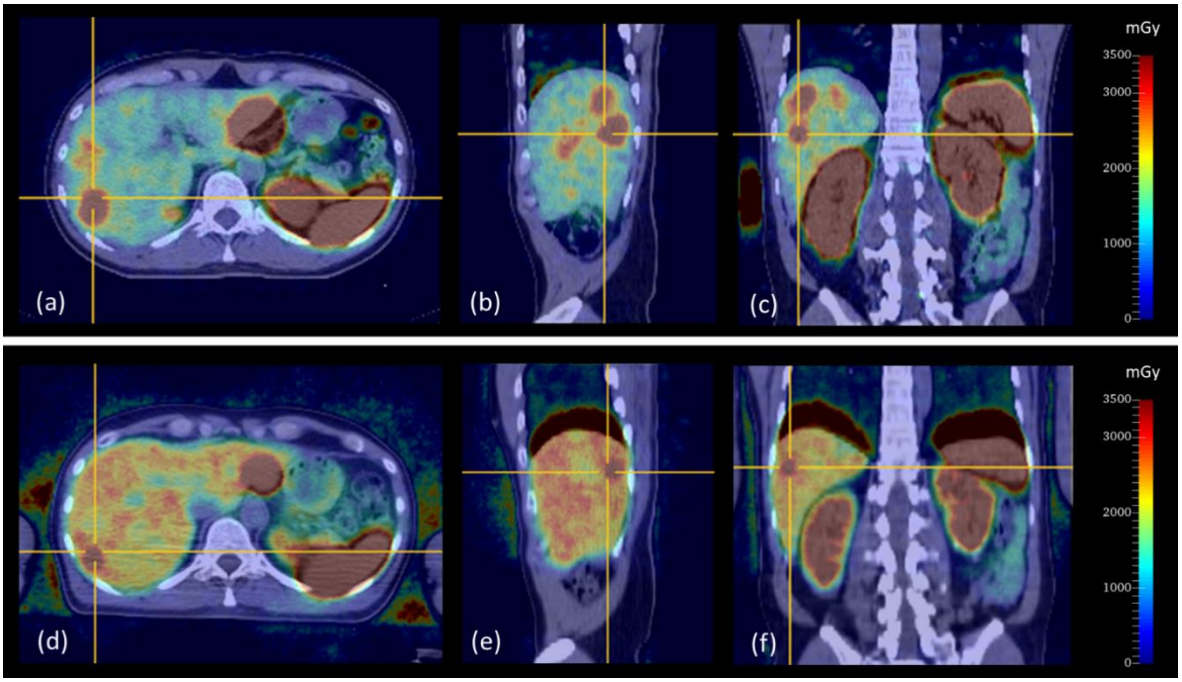

Figure 5.16. (a) axial, (b) sagittal and (c) coronal orthogonal projections of the voxel-wise absorbed dose distribution of the example patient #3 after the first therapy cycle, aligned with the respective CT scan, estimated by TOPAS-MC using ^{177}Lu-DOTATATE SPECT scans. The same in (d – f) obtained with TOPAS-MC using ^{68}Ga-DOTANOC PET/CT scans, considering ^{177}Lu as the emitting source. Note the slight misalignment between the PET and CT scans that is typically due to the patient's breathing movements during imaging and the different acquisition time of the two scans (i.e., CT takes seconds while PET takes several minutes). The same views are presented for both scans. The color scale represents absorbed dose, in mGy. Physiological uptake is noticed in the liver, kidneys, spleen and NETs.

Figure 5.17 exhibits the cDVHs obtained for the organs and NETs using the MC absorbed dose distributions estimated for the two tracers (i.e., for ^{177}Lu-DOTATATE, we present cDVHs for the first PRRT cycle). As in the previously shown cDVHs, the curves exhibit the expected appearance. ^{68}Ga-DOTANOC cDVHs show that both kidneys present similar absorbed dose distribution and that the bone marrow has the most uniform uptake. The same findings were reported in the previous section for the ^{177}Lu-DOTATATE cDVHs (see Figure 5.10). Comparing both tracers, in all patients, ^{177}Lu-DOTATATE and ^{68}Ga-DOTANOC revealed different absorbed dose distribution in some VOIs. The bone marrow cDVHs showed the best agreement, followed by the liver, while NETs revealed the most prominent deviations.

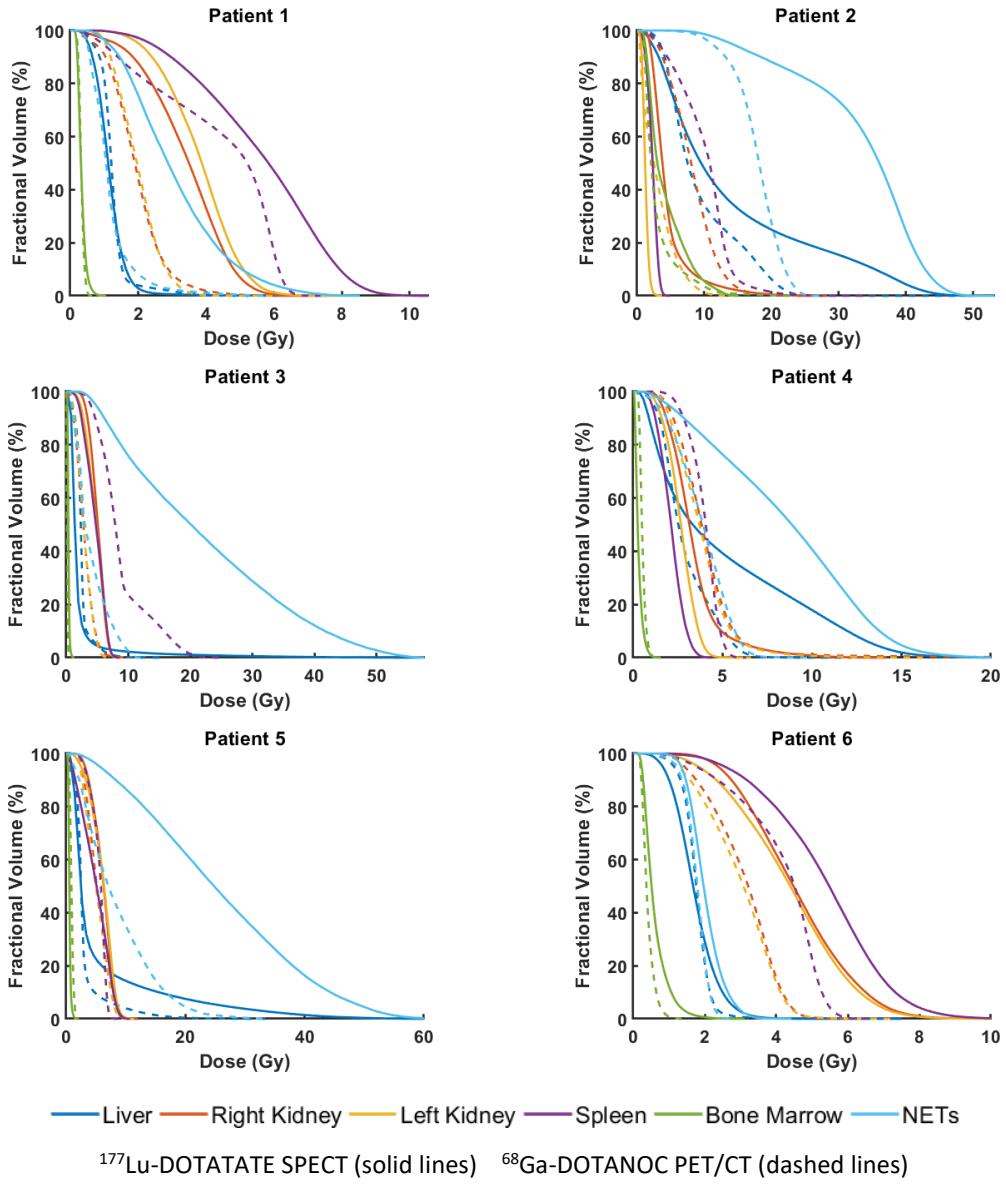

Figure 5.17. Cumulative DVHs computed for the liver, kidneys, spleen, bone marrow and NETs by analysis of the voxel-wise absorbed dose distributions obtained by TOPAS-MC with ^{177}Lu-DOTATATE SPECT scans (solid lines) of the first therapy cycle and pre-therapeutic ^{68}Ga-DOTANOC PET scans (dashed lines). The vertical axis represents the fractional volume that received a minimum absorbed dose. For most VOIs, the cDVHs for the two tracers are rather different.

Organ and NETs mean absorbed dose obtained by MC simulations using ^{177}Lu-DOTATATE SPECT and ^{68}Ga-DOTANOC PET/CT images were comparable in some cases. Table 5.7 exhibits the mean absorbed dose data for all of the patient cohort. Similar to the SPECT data, high inter-patient variability was seen for the mean absorbed dose in all VOIs computed using the pre-therapeutic scans, particularly in the NETs.

Table 5.7. Mean absorbed dose (Gy) in the organs and NETs, determined with TOPAS-MC simulations, using the actual absorbed dose distributions derived from the post-therapeutic ^{177}Lu-DOTATATE SPECT scans of the first therapy cycle and the relative tracer biodistribution captured by the pre-therapeutic ^{68}Ga-DOTANOC PET/CT scans. Values are presented as mean (± SD) [range].

VOI	D_{SPECT} (Gy)	D_{PET} (Gy)
Liver	4.98 (± 4.85) [1.16 – 14.14]	3.50 (± 3.03) [1.25 – 9.51]
Right Kidney	4.55 (± 1.02) [3.38 – 6.08]	4.27 (± 2.31) [1.96 – 8.40]
Left Kidney	3.81 (± 1.69) [1.23 – 6.04]	3.30 (± 1.04) [2.00 – 5.07]
Spleen	4.17 (± 1.58) [2.12 – 5.74]	6.22 (± 2.74) [3.94 – 10.39]
Bone Marrow	1.04 (± 1.51) [0.30 – 4.12]	0.92 (± 1.17) [0.12 – 3.25]
Tumors	16.03 (± 13.23) [2.01 – 33.43]	6.18 (± 6.26) [1.19 – 17.8]

In Figure 5.18, the mean absorbed dose values in the VOIs determined for each patient is presented. Although there is not a clear relation between the two tracers, it can be seen that ^{68}Ga-DOTANOC PET/CT scans resulted in lower mean absorbed dose in the NETs in all patients.

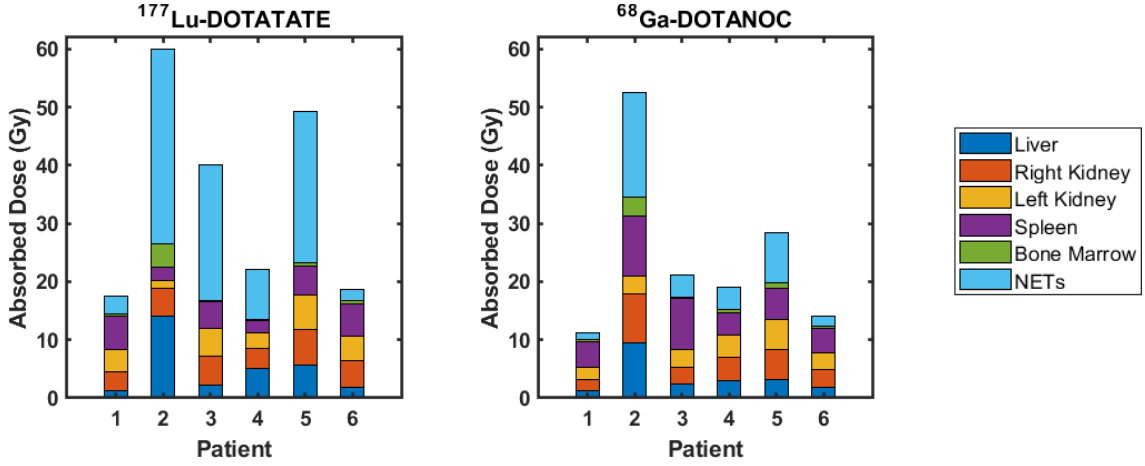

Figure 5.18. Individual results of mean absorbed dose (Gy) in the organs and NETs, determined with TOPAS-MC simulations, using the actual absorbed dose distribution given by the post-therapeutic ^{177}Lu-DOTATATE SPECT scans of the first therapy cycle (left panel) and the relative tracer biodistribution captured by the pre-therapeutic ^{68}Ga-DOTANOC PET/CT scans (right panel).

Figure 5.19 presents the RD between mean absorbed dose values determined using both (SPECT and PET) scans. The results show RDs from -83.1% up to 358.5%. Regarding the liver, dosimetry with ^{68}Ga PET scans underestimated absorbed dose values, with respect to ^{177}Lu SPECT. A median RD of -15.9% (min = -45.4%, max = 17.1%) was found. However, there were no major differences between the two tracers (ICC = 0.841). In most cases, mean absorbed dose in the right kidney was higher for ^{177}Lu-DOTATATE, compared to ^{68}Ga-DOTANOC. A similar trend was seen for the left kidney. The right and left kidneys presented a median RD of -23.2% (-42.9%, 75.8%) and -24.0% (-47.4%, 149.7%), respectively. These deviations were significantly relevant, as an ICC of 0.328 and 0.359 was found, respectively, for the right and left kidneys. Similarly, mean absorbed dose in the spleen was higher for ^{68}Ga-DOTANOC, compared to ^{177}Lu-DOTATATE. The spleen (ICC = -0.265) presented the most significant differences with a median RD of 48.6% (-23.5%, 358.5%). Contrary, the bone marrow

absorbed dose exhibited higher values for ^{177}Lu-DOTATATE. A median RD of -12.3% (-63.9%, 70.3%) was noted, however, the differences were not significant (ICC = 0.953). The highest median RD of -57.9% (-83.1%, -13.0%) was seen for the NETs (ICC = 0.475), which presented higher mean absorbed dose for ^{177}Lu-DOTATATE, being always underestimated by ^{68}Ga-DOTANOC. Since dosimetry using both scans was performed considering the same VOIs to compute mean absorbed dose and ^{177}Lu as the emitting radionuclide, the differences may be related with the use of different peptides.

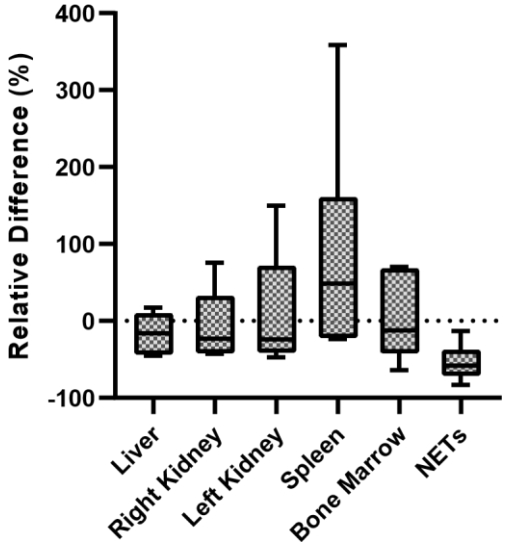

Figure 5.19. RD between the mean absorbed dose estimated by TOPAS-MC in organs and NETs, using post-therapeutic ^{177}Lu-DOTATATE SPECT and pre-therapeutic ^{68}Ga-DOTANOC PET/CT scans, with SPECT data as reference. The spleen presented the highest deviations. Positive values represent cases in which absorbed dose using ^{68}Ga PET/CT images was higher than that determined using ^{177}Lu SPECT scans.

Considering the specific data from these six patients, the predictive dosimetry for personalized treatment planning based on pre-therapeutic scans could not yet be confirmed as the results suggest that absorbed dose obtained using pre- and post-therapy information is quite different in the studied organs and NETs. A detailed discussion of the results here reported is presented in the next chapter.

Chapter 6

Discussion

In the last decade, ^{177}Lu-DOTATATE PRRT has been shown to be remarkably effective in the treatment of advanced NETs over-expressing SSTR, with symptom relief and tumor regression. However, a better outcome can be achieved when patient-personalized dosimetry is performed [106]. While renal toxicity is manageable with the co-injection of amino acid infusions that reduce tubular reabsorption, dosimetry calculations after each treatment cycle allow the delivery of patient-specific activities that maximize tumor irradiation and reduce the risk of toxicity. In addition, the significant absorbed dose variability among patients highlights the need for individualized treatment. Several methods have been used to quantify tissue exposure to ionizing radiation. The aim of this work was to perform internal absorbed dose calculations in the context of ^{177}Lu-DOTATATE PRRT, to compare the dosimetry of two methods (VSV and TOPAS-MC) and retrospectively assess possible critical organ toxicity and therapy effectiveness. The feasibility of pre-treatment dosimetry with ^{68}Ga-DOTANOC PET/CT scans was also addressed. For this purpose, processed (i.e., reconstructed, corrected, co-registered, resampled) pre- and post-therapeutic clinical scans were used.

6.1. Dead Time and SPECT Calibration Factor

The decreased image intensity related with a poor photon detection can be due to limited processing of the system's electronics and pileup effect. Dead time correction compensates for count losses and removes the pileup effect, returning the image's actual count distribution. Repeated phantom measurements were used to compute the camera's dead time and CF_{SPECT}. Five image acquisitions were performed over a 7-days period. The dead time constant was estimated using the decaying source method, assuming that the camera's system behaves according to the Sorenson's paralyzable model.

The estimated dead time constant was not significantly different from the values found in the literature for similar studies and gamma cameras. Some groups mention that, when using the decaying source method, imaging should be performed for a period at least equal to the half-life of the radionuclide under study [49]. However, others support that image acquisition should be conducted until count losses are not significant, namely until the last scan has less than 4 kcps [112]. Due to logistical constraints, we chose the first approach. The computed dead time constant was used to correct phantom and patient SPECT scans for dead time losses using the Lambert W function. Performing a similar analysis as in other studies [124], we found that dead time losses reached up to approximately 10%, 7% and 4% in SPECT scans acquired 24 h, 120 h and 168 h PI, respectively. Around half of the SPECT scans acquired 24 h PI were affected by count losses higher than 3%, while approximately half of the SPECT images at 120 h and 168 h PI suffered from losses greater than 0.9% and 1%, respectively (Table 5.1). Higher count losses were seen in patients with significant tumor burden (patients #2 and #4). This is possibly related with the increased retention of the tracer in the NETs and a lower clearance rate, which resulted in a greater number of events in imaging studies. Furthermore, regarding the patient with the highest

injected activity (~ 7.7 GBq) and tumor burden in the FOV, it was seen that SPECT scans acquired 24 h PI exhibited a count rate of approximately 740 kcps, a value much lower than the estimated saturation point (~ 3000 kcps). Therefore, given the considerable low count rate registered in the patient studies, the influence of dead time losses was deemed negligible. This observation was supported by comparing the organ mean absorbed dose obtained using both dead time corrected and uncorrected SPECT scans (see Section 5.4.1), which revealed that these were not statistically different (ICC > 0.99). In general, dead time losses resulted in an underestimation of mean absorbed dose higher than 2% in more than half of the cases, reaching values up to approximately 7% in all VOIs (see Table 5.5).

Our findings are comparable with the results of others. In a recent study, Desy et al. [124] investigated the influence of dead time losses in absorbed dose calculations of clinical studies of ^{177}Lu-DOTATATE PRRT using a Symbia T6 gamma camera. They deduced a dead time constant for the whole spectrum of ^{177}Lu (τ = 0.55 μs) while we determined its value for the 208 keV photopeak. Nevertheless, they reported count losses ranging from 0.55% up to 9.82% in the scan acquired 24 h PI and found that, if uncounted for, dead time can lead to an underestimation of renal absorbed dose up to 6.15%. Since count losses increase with injected activity, in personalized PRRT dead time correction may be required for accurate dosimetry as the use of higher activities results in higher count rates, particularly in scans acquired shortly after injection. The absence of dead time correction in these cases leads to an underestimation of the absorbed dose in critical organs which may support the administration of more treatment cycles, thus increasing the toxicity risk [124].

Regarding quantitative ^{177}Lu SPECT imaging with the 208 keV photopeak, several 3D CFs have been reported. In this study, the CF used to calibrate the clinical SPECT scans was computed as the average of five values calculated for activities ranging from 2.3 to 4.8 GBq. The CF_{SPECT} was significantly higher than the typical values, which is possibly due to the different system's components geometry (i.e., angle of acceptance), SPECT's spatial resolution and reconstruction process. It has been reported that the estimated CF_{SPECT} could result in an overestimation of the activity for actual values under 13 MBq [22]. However, since images at all time points presented a higher total activity, the CF_{SPECT} seemed a reasonable value to be applied to patient studies for activity calibration.

6.2. Image-based Biodistribution of ^{177}Lu-DOTATATE

Planar quantification allows the study of the retention and elimination of the tracer, during a given time period. This is the first step in estimating the absorbed dose by the tissues. In this study, the activity distribution was determined using the quantitative information from serial planar WB scans acquired at specific moments PI. The analysis was based on the assumption that all biokinetic models were still an accurate representation of the tracer distribution beyond the last imaging point.

Post-therapeutic planar WB scans revealed the expected physiological uptake of the tracer in the liver, spleen, kidneys and known NETs. The retention of ^{177}Lu-DOTATATE in the WB, over time, in patients who underwent PRRT was retrospectively evaluated. It was found a significant inter-patient variability regarding retained activity, which can be due to several factors such as kidney function, tumor burden and SSTR density [125]. The impact of these aspects is unclear since it was outside of the scope of the present work. Overall, a decreasing tendency of the retained activity over time was seen. The majority of the tracer is cleared within the first 24 h, as seen in Figure 5.2, with minimal retention 120 h PI and less than 10% of the total injected activity remaining in the body seven days after therapy (Table 5.2). In a recent study, Levart et al. [125] reported that most of the injected activity was eliminated within 24 h PI, with an average ^{177}Lu-DOTATATE retention of 33%, which is comparable with our 32.2%

retained activity. Our results are also in agreement with the NETTER-1 phase-III study [6], which showed a renal clearance of approximately 60% in the first 24 h PI.

The bi-exponential model is the best fit to the data when early imaging is performed [121]. Therefore, in the present work, this model was applied to the WB activity estimated from the 2D scans for an accurate analysis of the tracer's biodistribution. Our results showed the two elimination phases of ^{177}Lu-DOTATATE, as previously reported by Sandstrom et al. [101], namely a faster and earlier clearance with an effective half-life of roughly 4 h and a slower excretion of approximately 72.6 h (Figure 5.4). The early clearance phase is assumed to be related to the physical decay of ^{177}Lu and renal clearance. The later phase is possibly mainly due to the physical decay since the tumors will behave as progressive activity sinks, which reduces the levels of circulating radiotracer and leads to lower renal clearance. As expected, a greater retention was seen in patients with higher tumor burden (patients #2 and #4), which presented a longer effective half-life for the later clearance phase. The estimated WB effective half-life values are comparable with those of other groups [126], who have reported an early effective half-life of 4.5 h for ^{177}Lu-DOTATATE. However, others [101][127] found lower values for both clearance phases. This disagreement was not surprising as the tracer long-term retention is determined by the tumor burden [128], which varied significantly between patients. In fact, when data from patient #2 was excluded, it was found a better agreement, with a slower elimination phase of around 66 h. Nevertheless, different activity calculation methods (e.g., blood samples, planar imaging) and fit models, may also be related with different estimates. Additionally, we included the injected activity value in the fitted data. However, the duration of the injection, which took approximately 30 minutes, was not considered. Thus, it is possible that the effective half-life determined for the earlier elimination phase may be affected by an uncertainty related to this simplification.

The organ and NETs data (Figure 5.3), in all cycles, showed a similar behavior as the WB with a gradual decrease of the retained activity after injection. Organ uptake varies according to the arterial supply and venous washout. Therefore, it is assumed that organ activity is described by a sudden increase in the first minutes PI (or during) [128][129], which is related with the specific binding of ^{177}Lu-DOTATATE to the SSTR, and by an exponential decline, in which the physical decay and clearance dominate over the residual binding of the tracer. As there is no information before the first hour PI, the uptake phase is not visible in all curves. To better understand the behavior of the tracer in the organs during this period, a dynamic study can be performed. Nonetheless, some patients revealed a delayed uptake in the liver which may be related with the presence of hepatic lesions. Overall, a non-uniform uptake was seen among all patients (Figure 5.4). Quantitative evaluations confirmed the slow clearance from the NETs, which presented the highest effective half-life of approximately 88 h. All organs presented a mean effective half-life lower than the ^{177}Lu's physical half-life of 6.647 days. This implies that the tracer is eliminated faster through physiological mechanisms than by the physical decay, as expected. In addition, effective half-life estimates in the liver and right kidney showed large inter-patient variability, which is possibly related with the different hepatic tumor burden between patients.

Most of our organ effective half-life estimates lie within the range of values reported by other groups (see Table D.1. of Appendix D). The liver and NETs median effective half-lives agreed with Hanscheid et al. [130], although we report a larger range. Contrary, our spleen effective half-life estimates did not completely agree with the literature, being higher than expected. However, the range was similar. For these VOIs (i.e., liver, spleen and NETs), the highest values belonged to patient #2 (i.e., these are outliers, see Figure 5.4). When the data from this patient, with the greatest tumor burden, was excluded from the analysis, a better agreement with the published data was achieved, with a mean effective half-life of 66.2 h, 71.6 h and 74.2 h for liver, spleen and NETs, respectively. Our results became particularly closer to those reported by Wehrmann et al. [127], who followed a similar protocol as in this study.

Moreover, our renal effective half-lives were consistently higher, even when the data from patient #2 was removed. The disregard of these data also resulted in a lower inter-patient variability in all VOIs (i.e., lower SD).

Although the observed behavior of the tracer in the organs and NETs did not differ from the expected, the use of planar scans for activity quantification suffers from some issues, such as tissue overlapping. Renal activity can be significantly affected due to high uptake of the liver and intestine overlap. If not addressed, renal activity will be overestimated. This is particularly important when TACs are used in dosimetry. However, in this study, organ TACs obtained with 2D scans were only used for the biokinetic analysis and effective half-life determination. In addition, there are other uncertainties in the planar images because they have not been corrected for photon attenuation and scattering. The influence of these variables on the effective half-life calculation was outside the scope of the present study.

6.3. Voxel S-values Analysis

State-of-the-art SPECT and PET scanners, currently used in medical institutions, display multiple image spatial resolutions. This is challenging when one wishes to perform voxel-wise dosimetry using the kernel convolution approach as VSVs are radionuclide-, tissue- and voxel size-specific. Therefore, it is important to have VSVs for all possible combinations of voxel dimensions typically used in NM studies. Several methods can be used to compute VSV kernels. However, most are rather complex and these are usually pre-calculated using MC simulations. In this study, VSVs for different isotopes (^{177}Lu and ^{68}Ga), materials (soft tissue and bone) and cubic voxel sizes (2.21 mm and 4.42 mm) were determined using TOPAS-MC. Simulations were performed considering a source uniformly distributed within the central voxel of a homogeneous cubic voxelized phantom. VSVs were benchmarked against published data to assess their influence in 3D dosimetry of ^{177}Lu-DOTATATE in PRRT. Furthermore, this comparison was used to validate TOPAS-MC for subsequent patient-specific absorbed dose simulations.

Considering the data for both materials and voxel sizes, our results showed a significant decrease of the VSVs from the source voxel to their nearest neighbor, higher than 97% and 80% for ^{177}Lu and ^{68}Ga, respectively. This was expected for ^{177}Lu. This radionuclide decays with the simultaneous emission of γ-photons and β-particles. The latter, due to their very short range (see Table 2.1, lower than 2.21 mm), deposit most kinetic energy in the source voxel. Thereby, the contribution of electrons to the VSVs, due to inelastic collisions, is significant at small distances. Contrary, the tail of the ^{177}Lu distribution (i.e., VSVs at larger distances) is due to the contribution of bremsstrahlung and γ-emissions. Since the energy of the photons emitted by ^{177}Lu with higher probability is greater than 50 keV, photon contribution to the VSVs is mostly from Compton scattering. Moreover, ^{177}Lu VSVs are lower than those computed for ^{68}Ga (Figure 5.5 and Figure 5.6) due to a higher energy deposition by ^{68}Ga's γ-emission, which was expected as this decay has a higher energy ($Q_{Ga\text{-}68}$ = 2.9 MeV and $Q_{Lu\text{-}177}$ = 498 keV).

Regarding the ^{177}Lu data, reasonable agreement with the reference values was seen in voxels close to the source, for both tissues and voxel sizes. In this region, differences were within ±10%. Higher discrepancies, up to approximately 44%, were seen for voxels at larger distances. Overall, the deviations in the VSVs are most likely related to the different particle transport physical models used in the MC codes and different decay scheme data. These findings are in agreement with Pacilio et al. [93], who compared VSVs obtained with different MC codes. They reported higher differences for voxels further from the source and variations up to 30% at small distances for low-energy β-emitters.

Concerning different radiation transport models, uncertainties in the material's cross sections increase at lower energies. In fact, studies have reported particularly larger differences in the VSVs computed

for low-energy β-emitters using different MC codes [131]. However, TOPAS-MC by being based on Geant4, a modern radiation transport code, is assumed to better model low energy physic processes than older codes such as DOSEXYXncr. In addition, higher discrepancies were observed for bone data compared to soft tissue and these were more significant for 4.42 mm cubic voxels (Figure 5.7). The phantom's material composition used in this study was different from that used by Lanconelli et al. [94], who considered the soft tissue and bone composition defined by the ICRU Report 10b [132]. This could have contributed to the observed differences since it has been shown that the use of materials with similar but different elemental compositions can lead to significant discrepancies in energy deposition due to the different cross-section libraries used by the various MC codes [133].

Unlike Lanconelli et al. [94], who simulated primary particles individually as monoenergetic sources and summed their weighted contributions according to the emission spectrum of ^{177}Lu, we simulated the full decay. Therefore, differences between our datasets may be related with the consideration of different particle emissions, which results in different energy deposition and absorbed dose distribution. Mikkel [134] computed ^{177}Lu VSVs for 3 mm cubic voxels using DOSXYZncr. The results were in excellent agreement with [94], except for the source voxel. Since both used the same MC code, Mikkel suspected that this could have been related with the non-negligible Auger and internal conversion electron emission in the decay of ^{177}Lu that Lanconelli et al. may not have considered. Similar conclusions were drawn by Lai et al. [135], who compared ^{177}Lu VSVs data including and excluding the contribution from these electrons. When these were not accounted for, they found lower differences (~ 7 times) in the VSVs of the source voxel, with respect to [94]. Due to the short range of these particles, their exclusion did not affect VSVs at larger distances. Since in this study the contribution of both Auger and internal conversion electrons was included in the VSVs computation, this could explain the differences in the regions with greater electron contribution to the energy deposition, as these electrons comprise around 33% of the total number of emissions per disintegration [135]. Furthermore, although using a different voxel size, Lai et al. [135] reported a RD of approximately 10% for the source voxel in breast tissue (ρ = 1.04 g/cm^3), when considering all radiation contributions, which is comparable with our values in soft tissue (see Table 5.3).

Lastly, it was expected that VSVs in voxels at an equal distance from the isotropic source would have similar values. However, at further distances this was not seen (i.e., asymmetrical VSVs) although the fluctuations are within the statistical uncertainty of the VSVs. This issue could have been overcome by computing the mean value of the VSVs in voxels at the same radial distance from the source voxel and assign that value to all symmetric voxels. However, since MC absorbed dose estimates would reflect this asymmetry and voxels further away from the source present VSVs several orders of magnitude lower than that of the source voxel, causing little impact on absorbed dose estimation at the voxel level [93][94]-[96], we decided to use the original ^{177}Lu VSVs dataset instead of the mean values, determined for soft tissue and 2.21 mm cubic voxels, for our voxel-wise dosimetry with the convolution method.

6.4. Voxel-wise Dosimetry

6.4.1. Comparison between the VSV method and TOPAS-MC

Over the years, due to the increasing awareness to perform individual dosimetry calculations in NM therapies to ensure the maximum irradiation of tumor tissue and prevent toxicity, several methods have been suggested to quantify tissue absorbed dose. Currently, MC simulations are considered the gold standard of dosimetry approaches, with high accuracy despite the great computational demand [76][78]. Although some groups have explored the potential of GATE-MC and GAMOS-MC in image-based

dosimetry in TRT [136][137], to the best of our knowledge, no studies report the use of TOPAS-MC for this purpose. In this retrospective study, we evaluated the use of VSVs and TOPAS-MC simulations to perform voxel-wise dosimetry calculations in patients who underwent ^{177}Lu-DOTATATE PRRT. A comparison between the two methods was performed to assess if VSV dosimetry is suitable for clinical purposes. The comparison was made in terms of absorbed dose per treatment cycle.

Our data shows that, in most cases, organ and NETs mean absorbed dose was lower when estimated by the convolution method (Figure 5.11). Nevertheless, a very good agreement (ICC > 0.90) was found between the two methods. cDVHs (Figure 5.10) show nearly identical absorbed dose distribution in all VOIs. Differences are possibly related with the inclusion of patient-specific anatomy information in the MC simulations since the VSVs were calculated under the assumption of homogeneous soft tissue (ρ = 1.0 g/cm^3). Therefore, the convolution method may not produce accurate absorbed dose estimates for low- or high-density regions (e.g., lung and bone) and media interfaces (e.g., soft tissue – bone).

The best agreement was found for the liver (ICC = 1.000). In more than half of the twenty-four treatments, liver mean absorbed dose obtained by VSV was lower than the MC estimates (median RD = -1.0%). The liver presented the lowest intra- and inter-patient variability. Liver and NETs RD showed a similar pattern, which was expected since most NETs, in this patient cohort, were located in the liver. However, NETs exhibited a higher inter-patient variability (RD varying within ±10%), with half of the treatments presenting higher mean absorbed dose with MC (median RD = 0.4%). Still, differences were statistically negligible (ICC = 0.999). Bland-Altman analysis of the absorbed dose in the interface tumor – healthy tissue supports this observation by pointing to a good correlation and agreement between the two approaches in this region (Figure 5.12). The highest discrepancies in the liver and NETs mean absorbed dose were found for patient #1, with the VSV method displaying the lowest values by approximately 6% and 10%, respectively. VOI analysis revealed that the NETs of this patient had a mean HU of -12. According to TOPAS output file, tissues with HU values between -15 and 15 were assigned a density of 0.98 – 1.0 g/cm^3. Since this density is lower than that assumed in the convolution method for soft tissue, simulated radiation interacted over a longer path-length, depositing its energy in a larger area and leading to a higher mean absorbed dose, as seen. In patient #5, the opposite occurred (RD_{max} = 8%). NETs of this patient presented mean HU values between 44 and 48, to which were assigned a density of 1.04 g/cm^3. In this case, the MC method simulated a more localized energy deposition, such that more voxels within the VOI presented lower absorbed doses, particularly at the border, resulting in a lower mean absorbed dose. Our results are comparable with those of Grimes and Celler [92], who reported a good agreement between tumor mean absorbed dose obtained by VSV and MC. They found that NETs presented the highest discrepancy compared to the other VOIs (i.e., liver, kidneys and spleen), with the convolution method underestimating absorbed dose by more than 5%. Conversely, a recent study by Graves et al. [138] reported a maximum absolute difference of 3.4% for tumor absorbed dose. Specifically, both studies encompassed a cohort of six patients, but used different MC codes, HU to material converters and VSVs lookup tables.

Regarding renal mean absorbed dose, we found that, in more than half of the treatment cycles, it was almost always higher when estimated by TOPAS-MC (ICC > 0.99). The largest differences were seen for patient #2, with MC simulations resulting in higher values. The left kidney, which had HU values lower than expected, presented slightly greater discrepancies since kidney density was significantly different from that of soft tissue assumed in the convolution approach. In turn, the RD of spleen mean absorbed dose was variable (median RD = 0.2%), as in the study by [92], with half of the treatment cycles presenting higher values with MC and the other half with VSV. However, an excellent agreement was found (ICC = 0.999) with differences within ±5%, which suggests that the assumption of uniform soft tissue in the VSV method is reasonable for estimating spleen absorbed dose.

Although not significantly different, not all MC absorbed dose estimates were in agreement with our prospects. The "worst" agreement was found for the right kidney (ICC = 0.992). However, higher differences were anticipated for the bone marrow absorbed dose since it is the organ with elemental composition more different from that of soft tissue. Due to the inclusion of more accurate information concerning patient morphology, we expected less scored absorbed dose with MC in high density regions (i.e., greater attenuation of cross-irradiation). However, albeit negligible (ICC = 0.999), bone marrow mean absorbed dose was almost always higher with MC. The bone marrow (median RD = -3.6%) presented the largest inter-patient variability, with the highest difference of approximately 26% between the two methods. The most significant deviations were seen for patient #4, wherein the VSV method presented lower mean absorbed dose values. We suspect this is possibly related with the local deposition of self-irradiation that contributed to a higher local dose. Moreover, higher bone marrow mean absorbed dose with MC could be related to low bone density. However, regarding patient #4, this does not seem to explain the significant RD as the patient was a 62 years-old male, being unlikely to suffer from this condition. Contrary, patient #2 had bone metastases in the L2 and L5 vertebrae, which seemed to cause a lower energy deposition.

Furthermore, low-density regions have lower interaction probabilities with radiation than soft tissue. Therefore, regions containing air (e.g., lungs, stomach, bowels) or hypodense structures will not have accurate absorbed dose values with the convolution method. The MC absorbed dose map in Figure 5.8 shows the absorbed dose distribution outside the patient's body, which is possibly due to the modelling of photon annihilation in air (i.e., loss of backscatter) [138]. This was also seen for the other patients and is not clear in the VSV absorbed dose distributions since this region was deemed as soft tissue, which lead to a higher attenuation of the radiation emitted from the patient and local energy deposition.

In addition to the neglect of tissue heterogeneities in the VSV approach, other factors may have contributed to the observed differences. Due to limited computational resources (e.g., processor and memory), the VSVs kernel used in the convolution was restricted to five voxels around the source. Hence, unlike MC simulations, above a certain distance this method disregards the contribution of high-energy γ-photons to the voxel-wise absorbed dose distribution [71]. This will most affect absorbed dose in organs in which cross-irradiation is a significant contributor to energy deposition. Some authors have investigated the effects of this phenomenon. Marcatili et al. [139] compared ^{18}F absorbed dose estimated by VSVs kernels of two different sizes and GATE-MC simulations. They found lower differences between the two methods when the larger kernel was used, reporting higher absorbed dose values. Gotz et al. [140] performed a similar analysis using several ^{177}Lu VSVs kernels of different sizes (i.e., ^{177}Lu is not a pure β-emitter). They verified that larger kernels increased the computation time but resulted in a better agreement between MC and the convolution method. Therefore, the truncation of the ^{177}Lu VSVs kernel and unrealistic consideration of cross-irradiation may explain the lower mean absorbed dose values obtained with the VSV approach compared to MC, particularly the highest differences seen for the bone marrow since the contribution of cross-irradiation, mostly from NETs, to bone marrow absorbed dose is significant [97][101], and very dependent on tumor burden and proximity to the bone marrow. Regarding patient #4, the influence of neglecting cross-dose may have been more substantial, possibly due to a different tracer distribution in the tissues that contribute to bone marrow irradiation. Although considered a possible outlier, in this particular case, MC simulations may be the most suitable method to assess hematological toxicity.

Regarding the data obtained with the pre-therapeutic PET/CT scans, slightly different results were seen compared to the analysis performed with the SPECT images. Similarly, MC simulations usually led to higher mean absorbed dose values. However, the highest median deviation of approximately -8% was seen for the spleen (ICC = 0.846), which also presented the largest inter-patient variability (Figure 5.15),

followed by the bone marrow (median RD = -5.1%). The different pattern may be related with the different tracer distribution within the VOIs, given by the PET scans, and the use of the pre-therapeutic CT scans that could have resulted in different radiation interactions and, ultimately, in a more different energy deposition compared to the convolution method. Moreover, significant changes in the organ's volumes and characteristics may have occurred during the period between the pre- and post-treatment imaging acquisitions. Since the segmentation was based on the post-therapeutic CT scans, it may have not been an accurate representation of the organ and NETs volume at the time of pre-therapy imaging, with additional co-registration misalignments, and could have influenced our data as the comparison was made in terms of mean absorbed dose in the VOIs. This may have been particularly significant for the NETs, which presented a smaller RD range, compared to that determined with the SPECT scans, as well as a lower median RD of -1.0%. This suggests that the density of these VOIs in the pre-therapeutic CT scans was more similar to that assumed in the VSV method, which may be related with a lower extension of the disease at that time (i.e., possible lower tumor volume). Nonetheless, the differences were not significant (ICC > 0.8) and the possible reasons for the observed deviations given above for the SPECT data are also valid.

In general, despite the knowledge that MC simulations yield more accurate results than other dosimetry approaches, both methods presented comparable dosimetry for organs and NETs in the abdomen. Other studies have reported similar conclusions in analogous contexts [92][136][138][140]. Therefore, the convolution method with VSVs appears to be a reasonable option for voxel-wise clinical dosimetry calculations in ^{177}Lu-DOTATATE PRRT patients, in regions with small density variations, considering the compromise between computation time and dosimetry accuracy. Nonetheless, MC may be required when considering high density regions or cross-irradiation from other organs is significant.

6.4.2. Post-treatment Dosimetry

In ^{177}Lu-DOTATATE PRRT, the kidneys and bone marrow are considered the main critical organs and the injected activity should be adjusted according to the possibility of nephrotoxicity or hematological complications. In this study, mean absorbed dose in the organs and NETs was analyzed to determine whether the patients were at risk of toxicity and to assess response to therapy. Since MC absorbed dose data is the most accurate, it was used for this purpose. However, as discussed in the previous section, as no significant differences were found between VSV and MC dosimetry, for this patient cohort, the conclusions are also applicable to the VSV data. Here we discuss the data from twenty-four treatment cycles of six patients.

The liver and spleen were the organs with the highest absorbed doses during PRRT (Appendix E), as expected, with a mean D/A_{inj} of 0.704 ± 0.699 Gy/GBq and 0.675 ± 0.233 Gy/GBq, respectively. The high physiological uptake by hepatic metastases results in a large liver irradiation [141]. Moreover, immunohistochemical studies [142] have confirmed the predominance of SSTR2 in the splenic tissue, which is the SSTR subtype preferred by DOTATATE. In general, mean absorbed dose in both VOIs was in good agreement with published results [143]. However, our liver values were slightly higher, which may be due to the inclusion of patients with great tumor burden in the liver as its volume included hepatic lesions.

Bone marrow mean absorbed dose (0.142 ± 0.182 Gy/GBq) was higher than the reported estimates [127][143]. The highest values were determined for patient #2, who presented bone metastases in the L2 and L5 vertebrae. When the data from this patient was excluded from the analysis, bone marrow mean absorbed dose became closer to the published data (0.064 ± 0.039 Gy/GBq). Except for this patient, the bone marrow was the organ that presented the lowest mean absorbed dose values, with a total absorbed dose ranging from 1.2 to 15.6 Gy (Table 5.4). Results show that, in half of the cohort

(patients #2, #5 and #6), total absorbed dose in the bone marrow was higher than expected, surpassing the maximum threshold of 2 Gy (Figure 5.13). However, since no biological parameters were collected, we cannot assert if bone marrow function was compromised. In general, higher bone marrow absorbed dose was found in patients with greater tumor burden. Moreover, since the spleen is a blood reservoir, upon radiation exposure, the red blood cells will also be irradiated. While some studies have discredited the correlation between spleen absorbed dose and hematological toxicity in ^{177}Lu-DOTATATE therapy, others have found a connection. In particular, Sabet et al. [34] reported that patients who had undergone splenectomy before treatment presented a lower degree of hematological toxicity. Thus, it was expected that patients with higher spleen mean absorbed dose would present higher bone marrow mean absorbed dose. However, this was not seen. Therefore, we deduce that the major contributions to the bone marrow absorbed dose, in this patient cohort, were self-irradiation, high tumor burden and, when applicable, the presence of bone lesions. These findings are in agreement with those reported by Sandstrom et al. [101], who have shown that irradiation from blood cells is the greatest contribution to bone marrow absorbed dose (i.e., self-irradiation) and that cross-irradiation from large NETs, particularly in the liver, is significant (i.e., increase in bone marrow absorbed dose). They also found that bone lesions contribute to a local rise in bone marrow absorbed dose, as we have seen. In addition, patients with a bone marrow total absorbed dose higher than the accepted limit also presented higher renal total absorbed doses compared to the other individuals.

Mean D/A_{inj} was found to be, respectively, 0.630 ± 0.233 Gy/GBq and 0.524 ± 0.261 Gy/GBq for the right and left kidneys. Overall, mean absorbed dose in both kidneys was not comparable in all patients. The difference was particularly significant for patient #2, with the left kidney receiving approximately 70% less dose than the right kidney. In patients with lower tumor burden, the left kidney presented slightly higher mean absorbed dose probably due to spleen cross-irradiation. Contrary, the right kidney was more exposed in patients with higher tumor burden, particularly focused in the liver, as the tracer will specifically bind to the up-regulated SSTR in tumor cells. Moreover, it has been reported that differences between absorbed dose in the right and left kidneys may be related to a different clearance rate of both kidneys, particularly if the tracer has a relatively long physical half-life, as is the case of ^{177}Lu [92]. This is further supported by the previously reported renal effective half-life estimates (see Section 5.2). Renal total absorbed dose exceeded the toxicity threshold of 23 Gy in only one patient (patient #5), who could have been at risk for renal impairment. However, more data regarding kidney function (e.g., serum creatinine) is needed to draw accurate conclusions. As mentioned, dosimetry was performed using only one SPECT scan, in some patients. In these cases, the non-consideration of biological excretion led to a greater error. Patient #5 presented both critical organs total absorbed dose above the accepted limits. However, absorbed dose calculations for patient #5 and the 3rd cycle of patient #6 were performed under these circumstances. Data from the latter showed an overestimation of the absorbed dose compared to the other cycles (Figure 5.13). Thus, we cannot assert if patient #5 was, indeed, at risk of hematological and/or renal toxicity. In this study, renal mean absorbed dose was higher than that estimated by Santoro et al. [143]. However, as the NETs, the range of the values is comparable with that reported by Cremonesi et al. [109], who summarizes data from multiple research groups.

In all patients, NETs presented higher mean absorbed dose (2.026 ± 1.789 Gy/GBq) than the liver. The greatest inter-patient variability in mean absorbed dose values was seen for these VOIs, which is possibly related with the different tumor burden, SSTR density profile or binding affinity [141]. In some cases, intra-patient variations in liver and NETs mean absorbed dose were due to therapy effectiveness. Positive response was seen in four patients, with decreasing tumor mean absorbed dose in late cycles, which indicates a reduction in the number of malignant cells. As to the other patients, one (patient #4) presented stable tumor mean absorbed dose and the other (patient #2) exhibited increasing values, which

may have been related with the high tumor burden that caused the accumulation of the tracer after previous cycles [144]. This last patient presented the highest tumor total absorbed dose of 151 Gy.

Mean absorbed dose values of the same patient were reproducible for most organs between cycles. The small differences may be due to variations in the tracer pharmacokinetic profile [143]. Increasing renal and bone marrow absorbed dose in later cycles has been related with treatment efficacy, secondary to reduced tumor burden and higher levels of circulating tracer [144]. However, the intra-patient mean absorbed dose in the kidneys, at the end of each cycle, was comparable (Figure 5.13) and differences are possibly related to the effectiveness or injected amount of renal protective agents [33]. Bone marrow mean absorbed dose was also reproducible, with no significant changes. Regarding absorbed dose distribution, cDVHs (Figure 5.10) were very useful to assess the uptake uniformity within a VOI, being particularly important in the study of NETs as they allow to understand their properties and determine whether the therapy is being well targeted. In all patients, except patient #2, the bone marrow presented a uniform uptake. Contrary, the NETs with the highest mean absorbed doses presented significant non-uniform absorbed dose distribution. However, the cDVHs also show that most of the NETs' volume received doses higher than tumor mean absorbed dose, which is desirable.

In view of the thresholds of 23 Gy and 2 Gy as the maximum recommended renal and bone marrow total absorbed dose, respectively, and despite the absence of biological samples that would confirm toxicity, the absorbed dose distributions show that, for half of the patients, the bone marrow was the absorbed dose limiting organ. In these cases, the injected activity could have been altered, not in an attempt to optimize treatment effectiveness, but rather to improve bone marrow toxicity. However, we cannot conclude about the treatment efficacy if that reduction had been implemented.

6.4.3. Pre-treatment Dosimetry

Prior to ^{177}Lu-DOTATATE PRRT, a ^{68}Ga-DOTA-peptide scan is acquired to diagnose the NETs and determine the patient's eligibility to the therapy. Since the peptide used in this pre-therapeutic imaging has similar characteristics to the one used in PRRT, the scans are thought to be useful in predicting the absorbed dose distribution due to the treatment. To the best of our knowledge, there are very few studies and limited information on this matter [127][145]. Thus, in this work, pre-therapeutic ^{68}Ga-DOTANOC PET/CT scans were used as the theoretical tracer's biodistribution to attempt to predict organ and NETs absorbed dose after therapy. Dosimetry was performed considering ^{177}Lu as the emitting radionuclide. Mean absorbed dose values obtained with MC were compared with those determined using the post-therapeutic SPECT scans of the first cycle.

^{68}GA-DOTANOC absorbed dose distributions revealed a similar visual pattern as ^{177}Lu-DOTATATE, with higher uptake in the spleen and NETs (Figure 5.16). However, results show that dosimetry data from ^{68}Ga PET and ^{177}Lu SPECT only agreed in two VOIs (ICC > 0.80), the liver and bone marrow (Figure 5.19). Overall, ^{68}Ga-DOTANOC and ^{177}Lu-DOTATATE presented distinct absorbed dose distribution in most VOIs, as shown by the cDVHs (Figure 5.17). Differences can be related with the use of different peptides, which have different affinity for the SSTR leading to a different tracer kinetics profile, and with the shorter half-life of ^{68}Ga ($T_{1/2}$ = 68 min) compared to ^{177}Lu. In half of the patients (#2, #4 and #5), liver mean absorbed dose with ^{68}Ga-DOTANOC was lower than that of ^{177}Lu-DOTATATE (median RD = -15.6%) and the bone marrow presented a higher mean absorbed dose for ^{177}Lu-DOTATATE (median RD = -12.3%) in four patients (#1, #2, #3 and #6). Biokinetic studies have shown that irradiation from circulating blood cells is the greatest contribution to bone marrow absorbed dose. Therefore, different clearance rate of both tracers results in different bone marrow irradiation. Studies that compared DOTANOC and DOTATATE kinetics [145] found that DOTANOC has a slower elimination rate and higher retention in blood circulation. Thus, higher bone marrow absorbed dose was

expected for ^{68}Ga-DOTANOC. In addition, patients in which dosimetry with ^{68}Ga-DOTANOC scans resulted in higher bone marrow mean absorbed dose also presented higher renal mean absorbed doses (patients #2, #4 and #5). Although this same relation was seen for the absorbed dose determined with SPECT scans (see Section 6.4.2), the patients were not the same (Figure 5.18).

In the remaining organs and NETs, no similarity was found between ^{68}Ga PET and ^{177}Lu SPECT mean absorbed dose estimates (ICC < 0.50). Both kidneys presented higher mean absorbed dose for ^{177}Lu-DOTATATE in four patients (#1, #3, #5 and #6). Since DOTATATE has a faster clearance rate via kidneys, this higher renal absorbed dose would be expected. However, the amino acid infusion administered prior to the treatment should have reduced this effect. The greatest discrepancy was seen for the spleen, with the RD varying between -23.5% and 358.5%. In four patients (#2, #3, #4 and #5), the spleen exhibited significantly higher mean absorbed dose values for ^{68}Ga-DOTANOC (median RD = 48.6%). However, this was not expected. Immunohistochemical studies have demonstrated the predominant expression of SSTR2 in the splenic tissue (around 80%), with SSTR3 and SSTR5 being minimal or non-existent [142]. DOTATATE is highly specific for SSTR2, contrary to DOTANOC which has a higher affinity for SSTR2, SSTR3 and SSTR5. Thus, it was expected that DOTATATE would present the highest spleen absorbed doses. Regarding the NETs, mean absorbed dose was always underestimated by ^{68}Ga-DOTANOC (median RD = -57.9%), as expected. The higher tumor absorbed dose for ^{177}Lu-DOTATATE is presumably related with the somatostatin binding profile of the tracers [29], since NETs have predominant SSTR2 expression. Apart from the renal estimates, our findings are in agreement with the results of similar studies. Both Wehrmann et al. [127] and Schuchardt et al. [145] reported higher renal and spleen mean absorbed dose for DOTANOC, with a higher half-life when compared with DOTATATE, while NETs presented higher mean value for DOTATATE. However, unlike in this study, both groups did not find significant differences, which could have been due to the fact that both compared different peptides coupled to the same radionuclide, thus discarding deviations related with different physical half-life.

Besides the use of different peptides, the differences may be also related with the acquisition time of both pre- and post-therapeutic scans. SSTR expression, and consequentially activity distribution, can change significantly during the period between the acquisition of the two scans. Therefore, the pre-therapeutic PET scans may not be an accurate representation of the tracer biodistribution, as these were acquired months before therapy. Moreover, differences between the absorbed dose estimated using ^{68}Ga PET and ^{177}Lu SPECT scans may result from a biased co-registration of the CT component of the PET scans with the CT image of the first treatment cycle. Since mean absorbed dose was computed with the segmentation based on this CT scan, misalignments will lead to inaccurate estimates. This is particularly important for small structures, such as the NETs and bone marrow. In fact, it was observed that, despite very good agreement of all organs, the bone marrow was not always coincident. This might be due to changes in the patient's body between the pre- and post-therapy imaging acquisitions. Nevertheless, in the future, the same analysis should be performed using pre-therapeutic scans acquired with the same peptide used for PRRT.

The data obtained in this study contributed to a clearer understanding of the potential of ^{68}Ga-DOTANOC scans for pre-treatment dosimetry. Overall, no correlation was found between the absorbed dose distribution obtained with ^{68}Ga-DOTANOC PET and ^{177}Lu-DOTATATE SPECT scans. Therefore, the results do not support the possibility of using pre-therapeutic ^{68}Ga-DOTANOC PET/CT imaging to predict organ and tumor absorbed dose after the first cycle of ^{177}Lu-DOTATATE PRRT.

6.5. Study Limitations

This study presents some limitations that may have had some impact on the dosimetry results. First, a small and heterogeneous patient cohort was analyzed. Regarding the comparison between MC and VSV absorbed dose estimates, the conversion from HU values to material density was performed with default density factors of a specific CT scanner, that was not the one used in the NM-Rf Department of the CCC. Therefore, the densities attributed to the tissues in MC simulations may have not been the actual values. Since the same steps of image processing (i.e., reconstruction, segmentation, co-registration, resampling) and activity quantification were followed for both methods, possible errors will affect the results in a similar manner and, therefore, will not have a significant influence in the comparison.

As to the absorbed dose calculation, several other restraints were encountered. CT and SPECT scans were acquired with a non-hybrid device (i.e., dual gamma camera without the CT component). The acquisition of SPECT and CT images on different scanners is not ideal as small misalignments are inevitable due to the inability to secure patient positioning and organ/respiratory motion between acquisitions. In this study, the registration of the two scans was fully manual. From the clinical perspective, this is a reasonable approach. However, for quantification purposes it is questionable, as it is highly dependent on human aptitude and introduces a bias to the results upon voxel-level integration (i.e., incorrect time-integrated activity) and errors in MC simulations. Ideally, SPECT/CT imaging should be performed in a hybrid equipment or include the use of fiducial marks placed on the patient's skin during both (SPECT and CT) scans. Furthermore, VOI segmentation was also purely manual, with the boundary definition being subjected to inter-observer variability. This is particularly significant for NETs, since these are typically small structures whose margins are not always clear. The consideration of an unrealistic volume, could have led to inaccurate absorbed dose estimates (e.g., larger volumes may reduce PVE but absorbed dose will be underestimated). Moreover, PVE was not accounted for, aside from the resolution recovery included in the reconstruction process. Therefore, due to their dimensions, NETs and bone marrow mean absorbed dose values may have been underestimated. Likewise, it has been shown that the use of noise uncorrected SPECT and PET scans, as in this study, can lead to erroneous dosimetry calculations both with VSVs and MC simulations. Regions that would not have event generation, such as air (both inside and outside the patient’s body) and non-human materials (e.g., patient table), will have associated decays that will lead to different absorbed dose distributions in these regions [137]. This may be important to ascertain critical organ toxicity. In addition, the error of the activity measurement based on the SPECT images was not assessed.

The retrospective nature of the study had also an important influence. The imaging protocol was not strictly followed in all clinical cases and dosimetry was performed with the available scans. Some patients did not undergo CT imaging in all therapy cycles. In these cases, VOI segmentation with the CT scan of the previous treatment was used to compute mean absorbed dose and cDVHs, assuming that organ and NETs’ volume remained unchanged between cycles. However, particularly for tumors, this conjecture is not realistic. In addition, dosimetry calculations were performed with one or two post-therapeutic SPECT scans. Due to the limited number of scans, the patient-specific effective half-life of the tracer was not estimated. Thus, no biological clearance was considered during calculation of the accumulated activity and the effective half-life of the tracer was deemed equal to the physical half-life of ^{177}Lu, which led to an overestimation of the absorbed dose distributions. Finally, due to the absence of biological parameters (e.g., blood samples), the results could not confirm toxicity nor the correlation of the absorbed dose with renal and hematological function.

Chapter 7

Conclusion

In this chapter, the main conclusions drawn from this study are reported as well as suggestions for future work in this research area to improve the accuracy of patient-specific voxel-wise clinical dosimetry in ^{177}Lu-DOTATATE PRRT.

7.1. Conclusions

The incidence of NETs has been progressively increasing over the years. Although PRRT is considered the most appealing therapeutic option, there is evidence that the current therapy regimen is not ideal as patients present fairly different responses. The lack of individual dosimetry assessments after TRT is a current issue that involves several clinical institutions. According to the European Council Directive 2013/59/EURATOM, transposed into the Portuguese Decree-Law No.108/2018, treatments must be planned to maximize tumor irradiation and prevent toxicity. Multiple protocols have been suggested for this purpose. Full radiation transport with MC simulations is deemed the gold standard since it presents advantages compared to other methods. However, the implementation in clinical routine is challenging since it poses a significant issue regarding computational resources. Thus, there is an ongoing discussion about which dosimetry protocol should be used to optimize PRRT. In this work, ^{177}Lu-DOTATATE PRRT clinical cases were retrospectively analyzed. The main goal was to investigate the patient-specific voxel-wise dosimetry computed by two different methods, using pre- and post-therapeutic 3D imaging. These measurements were also used to identify cases where the standard regimen led to critical organ toxicity and to assess the feasibility of pre-treatment dosimetry with ^{68}Ga-DOTANOC PET/CT scans.

The first step towards this goal was the computation of VSVs with the TOPAS-MC toolkit, which were validated against published data. After image processing, to enhance image quality and provide more accurate quantification, patient-specific dosimetry using post-therapeutic serial ^{177}Lu-DOTATATE SPECT and pre-therapeutic ^{68}Ga-DOTANOC PET/CT scans was performed with the pre-calculated ^{177}Lu VSVs and TOPAS-MC simulations. The comparison between VSV and MC absorbed dose data provided a valuable insight into the influence of some simplifications in dosimetry calculations. Organ and NETs mean absorbed dose obtained by VSV dosimetry, in the assumption of uniform tissue, was in very good agreement with the values estimated by MC and absorbed dose distributions in the abdominal region were nearly identical. This suggests that the convolution approach may be appropriate for clinical dosimetry in ^{177}Lu-DOTATATE PRRT patients, in regions with small density variations, since it is less time consuming than MC and produces similar dosimetry results. Still, MC simulations may be required when studying regions with high density variations and cross-irradiation is significant, as it provides more reliable dosimetry outcomes. Furthermore, mean absorbed dose values revealed significant inter-patient variability, which further reinforces the need for personalized treatment. Data showed that the bone marrow exceeded the recommended maximum absorbed dose in half of the patients, which could have been avoided if individual dosimetry had been done for each cycle/treatment. Lastly, regarding pre-treatment dosimetry, no correlation was found between organ and NETs mean

absorbed dose obtained with ^{68}Ga-DOTANOC PET/CT and ^{177}Lu-DOTATATE SPECT scans as estimates only agreed for the liver and bone marrow. Therefore, data do not support treatment planning using pre-therapeutic ^{68}Ga-DOTANOC PET/CT scans.

Despite the small patient cohort and existing limitations, overall, our results are in agreement with the values presented by others. We believe this work provides further knowledge for future developments in the dosimetry of TRT, by reinforcing the importance of personalized absorbed dose calculations, to avoid toxicity and improve clinical outcome. It is hoped that this study contributes to the development of a well-defined worldwide dosimetry protocol for personalized ^{177}Lu-DOTATATE PRRT in patients with metastatic NETs, that can be routinely implemented in a clinical setting.

7.2. Future Work

With the increasing interest in TRT for cancer treatment and individualized dosimetry, several improvements can be made to expand the work presented in this dissertation. Regarding the first part of this project, which consisted in the determination of the system's dead time and activity CF, it would be of interest to conduct more experiments using other methods to validate the reported values and, if necessary, to determine accurate factors for the gamma camera used in the NM-Rf Department of the CCC, to be then applied in patient studies of ^{177}Lu-DOTATATE PRRT. In addition, it is important to evaluate the accuracy of the activity measurement based on the SPECT images.

In this study, new routines were developed for TOPAS-MC to enable patient-specific 3D dosimetry using clinical SPECT or PET/CT scans, which was not yet possible with the available features of the code. To ensure the proper behavior of these routines, it would be interesting to validate them in dosimetry calculations against similar tools of other MC codes. Likewise, this validation could include a comparison of absorbed dose values obtained with TOPAS-MC and VSVs in a homogeneous medium to identify possible differences unrelated with tissue non-uniformity. In addition, the comparison between MC and VSV dosimetry was performed using VSVs computed with TOPAS-MC, using the same physics modules as in absorbed dose calculation. Therefore, it would be of interest to replicate the analysis with absorbed dose values determined with VSVs computed with other MC codes. Future studies with these routines could also address the optimization of the simulation parameters to attempt to increase computation speed while maintaining the accuracy. For this purpose, we suggest the adjustment of the radiation and particle range cut. In this work, the cutoff was chosen in a conservatory manner to ensure the precision of the results. This value can be easily increased without significantly altering the accuracy, possibly to a range equivalent to the voxel size as has been stated [69]. Moreover, the HU to material converter could be modified to include density correction factors representative of the CT scanner used in the NM-Rf Department of the CCC, which can be determined from phantom studies. Tissue densities predicted by this new converter could then be validated against those predicted with the Schneider's method [122]. Finally, to better understand the influence of tissue interfaces in absorbed dose, an in-depth analysis using automated segmentation algorithms could also be performed.

Regarding the assessment of critical organ toxicity, future work could include a detailed analysis of the tracer kinetics in each patient, using serial SPECT scans, and dosimetry could be performed considering the patient-specific effective half-life to account for biological clearance. In this context, it is also of great interest to investigate the biological effective dose in the tissues, to assess the biologic impact of the radiation and dose-effect correlation, since it addresses biological parameters that absorbed dose does not, such as the sublethal damage recovery time. In addition, in future patients, biological samples could be collected to allow the determination of a possible correlation between mean absorbed dose and

organic function biomarkers (i.e., dose-response and toxicity). It would also be desirable to perform the same calculations in a larger patient cohort to gain a better understanding of the inter-patient variability.

Finally, one reason behind the lack of routine dosimetry in TRT is the large financial demand related with imaging studies and the additional patient burden. To attempt to minimize this issue, classification algorithms (e.g., random forest) could be developed to predict response to therapy and toxicity, based on the patient's medical history (e.g., renal function), clinical presentation (i.e., SSTR2 density) and circulating biomarkers (e.g., chromogranin A, C-reactive protein, albumin levels). To validate the algorithm and ensure its good behavior, the results would have to be compared with data obtained using the conventional dosimetry approaches and biological parameters.

References

[1] Asadian, S., Mirzaei, H., Kalantari, B. A., Davarpanah, M. R., Mohamadi, M., et al. (2020). β-radiating radionuclides in cancer treatment, novel insight into promising approach. *Pharmacological research, 160*, 105070.

[2] Hoppenz, P., Els-Heindl, S., & Beck-Sickinger, A. G. (2020). Peptide-Drug Conjugates and Their Targets in Advanced Cancer Therapies. *Frontiers in chemistry, 8*, 571.

[3] Chan, T. G., O'Neill, E., Habjan, C., & Cornelissen, B. (2020). Combination Strategies to Improve Targeted Radionuclide Therapy. *J Nucl Med*, *61*(11), 1544–1552.

[4] Filippi, L., Bagni, O. & Nervi, C. (2020) Aptamer-based technology for radionuclide targeted imaging and therapy: a promising weapon against cancer. *Expert Review of Medical Devices*, *17*(8), 751-758.

[5] St James, S., Bednarz, B., Benedict, S., Buchsbaum, J. C., Dewaraja, Y., Frey, E., et al. (2021). Current Status of Radiopharmaceutical Therapy. *International journal of radiation oncology, biology, physics*, *109*(4), 891–901.

[6] Strosberg, J., El-Haddad, G., Wolin, E., Hendifar, A., Yao, J., Chasen, B., et al. (2017). Phase 3 Trial of ^{177}Lu-DOTATATE for Midgut Neuroendocrine Tumors. *New England Journal of Medicine*, *376*(2), 125–135.

[7] Bodei, L., Cremonesi, M., Grana, C. M., Fazio, N., Iodice, S., Baio, S. M., et al. (2011). Peptide receptor radionuclide therapy with ^{177}Lu-DOTATATE: the IEO phase I-II study. *EJNMMI, 38*(12), 2125–2135.

[8] Baum, R. P., Puranik, A. D., & Kulkarni, H. R. (2015). Peptide receptor radionuclide therapy (PRRT) of neuroendocrine tumors: current state and future perspectives. *International Journal of Endocrine Oncology*, *2*(2), 151–158.

[9] Council Directive 2013/59/Euratom of 5 December 2013 laying down basic safety standards for protection against the dangers arising from exposure to ionizing radiation, and repealing Directives 89/618/Euratom, 90/641/Euratom, 96/29/Euratom, 97/43/Euratom and 2003/122/Euratom. 013, 32013L0059. 2014. Available at http://data.europa.eu .

[10] Haug A. R. (2020). PRRT of neuroendocrine tumors: individualized dosimetry or fixed dose scheme? *EJNMMI research*, *10*(1), 35.

[11] Ljungberg, M., & Gleisner, K. S. (2015). Hybrid Imaging for Patient-Specific Dosimetry in Radionuclide Therapy. *Diagnostics*, *5*(3), 296–317.

[12] Muñoz, C. (2016). SPECT/CT Quantification of ^{177}Lu for Dosimetry in Radionuclide Therapy Treatments for Neuroendocrine Tumors [PhD Thesis, Faculty of Physics and Astronomy, University of British Colombia].

[13] Oronsky, B., Ma, P. C., Morgensztern, D., & Carter, C. A. (2017). Nothing But NET: A Review of Neuroendocrine Tumors and Carcinomas. *Neoplasia (New York, N.Y.)*, *19*(12), 991–1002.

[14] Liu, H., Xie, R., Zhao, Z., Xu, D., Yang, K., Ding, M., Tan, D., Liao, W., Han, X., et al. (2020). An 11-year retrospective study: clinicopathological and survival analysis of gastro-entero-pancreatic neuroendocrine neoplasm. *Medicine*, *99*(33), e21682.

[15] University of Iowa. (2018). What is neuroendocrine cancer? [Online] Available at: https://uihc.org/health-topics/what-neuroendocrine-cancer [*2021, May 20*]. *University of Iowa Hospitals & Clinics*.

[16] Ahmed M. (2020). Gastrointestinal neuroendocrine tumors in 2020. *World journal of gastrointestinal oncology*, *12*(8), 791–807.

[17] Dasari, A., Shen, C., Halperin, D., Zhao, B., Zhou, S., Xu, Y., Shih, T., & Yao, J. C. (2017). Trends in the Incidence, Prevalence, and Survival Outcomes in Patients with Neuroendocrine Tumors in the United States. *JAMA oncology*, *3*(10), 1335–1342.

[18] Scherübl, H., Streller, B., Stabenow, R., Herbst, H., Höpfner, M., Schwertner, C., et al. (2013). Clinically detected gastroenteropancreatic neuroendocrine tumors are on the rise: epidemiological changes in Germany. *World journal of gastroenterology*, *19*(47), 9012–9019.

[19] Faggiano, A., Ferolla, P., Grimaldi, F., Campana, D., Manzoni, M., Davì, M. V., et al. (2012). Natural history of gastro-entero-pancreatic and thoracic neuroendocrine tumors. Data from a large prospective and retrospective Italian Epidemiological study: The NET Management Study. *J Endocrinol Invest*, *35*(9), 817–823.

[20] Ito, T., Igarashi, H., Nakamura, K., Sasano, H., Okusaka, T., Takano, K., Komoto, I., et al. (2015). Epidemiological trends of pancreatic and gastrointestinal neuroendocrine tumors in Japan: a nationwide survey analysis. *Journal of gastroenterology*, *50*(1), 58–64.

[21] Reubi J. C. & Waser B. (2003). Concomitant expression of several peptide receptors in neuroendocrine tumours: molecular basis for in vivo multireceptor tumour targeting. *EJNMMI*, *30*(5), 781–793.

[22] Marin, G., Vanderlinden, B., Karfis, I., Guiot, T., Wimana, Z., Flamen, P., & Vandenberghe, S. (2017). Accuracy and precision assessment for activity quantification in individualized dosimetry of ^{177}Lu-DOTATATE therapy. *EJNMMI physics*, *4*(1), 7.

[23] Engstrom, A. (2012). Evaluation of 2D dosimetry in patients that received ^{177}Lu-octreotate for treatment of neuroendocrine tumors. [Master Thesis, University of Gothenburg].

[24] Aslani, A., Snowdon, G., Bailey, D., Schembri, G., Bailey, E., et al. (2015). Lutetium-177 DOTATATE Production with an Automated Radiopharmaceutical Synthesis System. *Asia Oceania J Nucl Med Biol*, 3(2), 107-115.

[25] Kolasinka-Cwikla, A., Lowczak, A., Maciejkiewics, K., & Cwikla, J. (2018). Peptide Receptor Radionuclide Therapy for Advanced Gastroenteropancreatic Neuroendocrine Tumors – from oncology perspective. *Nuclear Medicine Review*, *21*(2).

[26] Das, S., Al-Toubah, T., El-Haddad, G., & Strosberg, J. (2019). ^{177}Lu-DOTATATE for the treatment of gastroenteropancreatic neuroendocrine tumors. *Expert review of gastroenterology & hepatology*, *13*(11), 1023–1031.

[27] Gallivanone, F. (2017). Targeted radionuclide therapy frontiers in theranostics. *Frontiers in Bioscience*, *22*(10), 1750–1759.

[28] Kabasakal, L., Demirci, E., Ocak, M., Decristoforo, C., Araman, A., Ozsoy, Y., Uslu, I., & Kanmaz, B. (2012). Comparison of ^{68}Ga-DOTATATE and ^{68}Ga-DOTANOC PET/CT imaging in the same patient group with neuroendocrine tumours. *EJNMMI*, *39*(8), 1271–1277.

[29] Wild, D., Bomanji, J. B., Benkert, P., Maecke, H., Ell, P. J., Reubi, J. C., Caplin, M. E. (2013). Comparison of ^{68}Ga-DOTANOC and ^{68}Ga-DOTATATE PET/CT within Patients with Gastroenteropancreatic Neuroendocrine Tumors. *J Nucl Med, 54*(3), 364–372.

[30] Ambrosini, V., Campana, D., Bodei, L., Nanni, C., Castellucci, P., Allegri, V., et al. (2010). ^{68}Ga-DOTANOC PET/CT Clinical Impact in Patients with Neuroendocrine Tumors. *J Nucl Med, 51*(5), 669–673.

[31] Pettinato, C., Sarnelli, A., Di Donna, M., Civollani, S., Nanni, C., Montini, G., Di Pierro, et al. (2008). ^{68}Ga-DOTANOC: biodistribution and dosimetry in patients affected by neuroendocrine tumors. *EJNMMI, 35*(1), 72–79.

[32] Hennrich, U., & Kopta, K. (2019). Lutathera®: The First FDA- and EMA-Approved Radiopharmaceutical for Peptide Receptor Radionuclide Therapy. *Pharmaceuticals, 12*(3), 114.

[33] Rolleman, E. J., Melis, M., Valkema, R., Boerman, O. C., Krenning, E. P., & de Jong, M. (2010). Kidney protection during peptide receptor radionuclide therapy with somatostatin analogues. *Eur J Nucl Med Mol Imaging, 37*(5), 1018–1031.

[34] Sabet, A., Ezziddin, K., Hense, J., Ahmadzadehfar, H., Nagarajah, J., Poppel, T., et al. (2012). Long-term hematotoxicity after peptide receptor radionuclide therapy with 177Lu-octrotate. *J Nucl Med, 54*(11), 1857–1861.

[35] Bé, M. M., Chieste V., Dulieu, C., Browne, E., Chechev V., Kuzmenko N., et al. (2004). Table of Radionuclides. Monographie BIPM-5, Vol.2, Bureau International des Poids et Mesures.

[36] Blakkisrud, J. (2015). Tumor Dosimetry in a Phase I Study of Lu(177)-DOTA HH1(Belutin). [Master Thesis, Norwegian University of Science and Technology].

[37] Ljungberg, M., Celler, A., Konijnenberg, M., Eckerman, K., Dewaraja, Y., et al. (2016). MIRD Pamphlet No.26: Joint EANM/MIRD Guidelines for Quantitative ^{177}Lu SPECT Applied for Dosimetry of Radiopharmaceutical Therapy. *J Nucl Med, 57*(1), 151-162.

[38] Dash, A., Pillai, M. R., & Knapp Jr., F. (2015). Production of ^{177}Lu for Targeted Radionuclide Therapy: Available Options. *Nucl Med Mol Imaging*. *49*(2), 85-107.

[39] Basu, S., Parghane, R. V., Kamaldeep, & Chakraborty, S. (2020). Peptide Receptor Radionuclide Therapy of Neuroendocrine Tumors. *Seminars in Nuclear Medicine, 50*(5), 447–464.

[40] Bé, M. M., Chiste, V., Dulieu, C., Browne, E., Chechev V., Kuzmenko N., et al. (2008). Table of Radionuclides. Monographie BIPM-5, Vol.4., Bureau International des Poids et Mesures.

[41] Bé, M. M., Chiste, V., Dulieu, C., Browne, E., Chechev V., Kondev F. G., et al. (2013). Table of Radionuclides. Monographie BIPM-5, Vol.8., Bureau International des Poids et Mesures.

[42] Zaknun, J.J., Bodei, L., Mueller-Brand, J. et al. (2013). The joint IAEA, EANM, and SNMMI practical guidance on peptide receptor radionuclide therapy (PRRNT) in neuroendocrine tumours. *Eur J Nucl Med Mol Imaging 40*(5), 800–816.

[43] Bailey, D. L., Hennessy, T. M., Willowson, K. P., Henry, E. C., Chan, D. L., Alani, A., & Roach, P. J. (2015). In vivo quantification of ^{177}Lu with planar whole-body and SPECT/CT gamma camera imaging. *EJNMMI Physics, 2*(1), 20.

[44] Tsoulfanidis, N., & Landsberger, S. (2015). Measurement & Detection of Radiation. 4th Edition. Chapter 3: Review of Atomic and Nuclear Physics, pp. 71–98.

[45] Serway, R., Moses, C., & Moyer, C. (2005). Modern Physics. 3rd Edition. Chapter 13: Nuclear Structure, pp. 479-491, Chapter 14: Nuclear Physics Applications, pp. 526-530,538.

[46] Hauf, S., Kuster, M., Batic, M., Bell, Z. W., Hoffmann, D. H. H., et al. (2013). Radioactive Decays in Geant4. *IEEE Transactions on Nuclear Science, 60*(4), 2966–2983.

[47] Powsner, R. A., Palmer, M. R., & Powsner, E. R. (2013). Essentials of Nuclear Medicine Physics and Instrumentation. 3rd Edition. Chapter 1: Basic Nuclear Medicine Physics, pp. 1–20.

[48] Harkness-Brennan, L. (2018). An Introduction to the Physics of Nuclear Medicine. Chapter 5: Radiation interactions with matter.

[49] Knoll, G. F. (2000). Radiation Detection and Measurement. 3rd Edition. Chapter 2: Radiation Interaction, pp. 29–65. Chapter 4: General Properties of Radiation Detectors, pp. 103–129.

[50] Lechner, A. (2018). Particle Interactions with Matter. *Proceedings of the CAS-CERN Accelerator School on Beam Injection, Extraction and Transfer, 5*, 47–68.

[51] Berger, M.J., Hubbell, J.H., Seltzer, S.M., Chang, J., Coursey, J.S., Sukumar, R., Zucker, D.S., & Olsen, K. (2010). XCOM: Photon Cross Section Database (version 1.5). [Online] Available at: http://physics.nist.gov/xcom [*2021, July 15*]. *National Institute of Standards and Technology*, Gaithersburg, MD.

[52] Delker, A. (2015). Investigation of models with temporal and spatial interference in image-based dosimetry of ^{177}Lu-labelled radioligand therapies. [PhD Thesis, Ludwig Maximilians University, Munich].

[53] Mosman, E. (2016). Nuclear Medicine. [Online] Available at: https://radiologykey.com/nuclear-medicine-3/ [*2021, May 20*]. *Radiology Key*.

[54] Beauregard, J. M., Hofman, M. S., Pereira, J. M., Eu, P., & Hicks, R. J. (2011). Quantitative (177)Lu SPECT (QSPECT) imaging using a commercially available SPECT/CT system. *Cancer imaging: the official publication of the International Cancer Imaging Society, 11*(1), 56–66.

[55] Bailey, D. L., & Willowson, K. P. (2013). An Evidence-Based Review of Quantitative SPECT Imaging and Potencial Clinical Applications. *J Nucl Med*, *54*(1), 83-89.

[56] D'Arienzo, M., Cazzato, M., Cozzella, M. L., Cox, M., D'Andrea, M., Fazio, A., et al. (2016). Gamma camera calibration and validation for quantitative SPECT imaging with ^{177}Lu. *Applied Radiation and Isotopes, 112*, 156–164.

[57] Dewaraja, Y. K., Frey, E. C., Sgouros, G., Brill, A. B., Roberson, P., Zanzonico, P. B., & Ljungberg, M. (2012). MIRD pamphlet No. 23: quantitative SPECT for patient-specific 3-dimensional dosimetry in internal radionuclide therapy. *J Nucl Med*, *53*(8), 1310–1325.

[58] He, B., Nikolopoulou, A., Osborne, J., Vallabhajosula, S., & Goldsmith, S. (2012). Quantitative SPECT imaging with Lu-177: A physical phantom evaluation. *J Nucl Med, 53*, 2407.

[59] Uribe, C. F., Esquinas, P. L., Gonzalez, M., Zhao, W., Tanguay, J., & Celler, A. (2018). Deadtime effects in quantification of ^{177}Lu activity for radionuclide therapy. *EJNMMI physics, 5*(1), 2.

[60] Mezzenga, E., D'Errico, V., D'Arienzo, M., Strigari, L., Panagiota, K., Matteucci, F., et al. (2017). Quantitative accuracy of 177Lu SPECT imaging for molecular radiotherapy. *PloS one, 12*(8), e0182888.

[61] Velikyan I. (2013). Prospective of ^{68}Ga-radiopharmaceutical development. *Theranostics, 4*(1), 47–80.

[62] Johnbeck, C. B., Knigge, U., & Kjær, A. (2014). PET tracers for somatostatin receptor imaging of neuroendocrine tumors: current status and review of the literature. *Future Oncology, 10*(14), 2259–2277.

[63] Ezziddin, S., Lohmar, J., Yong-Hing, C. J., Sabet, A., Ahmadzadehfar, H., Kukuk, G., et al. (2012). Does the Pretherapeutic Tumor SUV in 68Ga DOTATOC PET Predict the Absorbed Dose of 177Lu Octreotate? *Clinical Nuclear Medicine, 37*(6), e141–e147.

[64] Koustou, T. (2019). Application development for personalized dosimetry in pediatric examinations of Nuclear Medicine based on Monte Carlo simulations and the use of computational models. [PhD Thesis, School of Health Sciences, University of Patra]. Institutional Repository at University of Patras.

[65] Elgazzar, A. H. (2015). The Pathophysiologic Basis of Nuclear Medicine. Chapter 21: Biological Effects of Ionizing Radiation, 715–726. Springer, Cham.

[66] Dance, D. R., Christofides, S., Maidment, A. D. A., McLean, I. D., & Ng, K. H. (2014). Diagnostic Radiology Physics: A Handbook for Teachers and Students. Chapter 20: Radiation Biology, 499–525. International Atomic Energy Agency.

[67] Bolch, W., Eckerman, K., Sgouros, G., & Thomas, S. (2009). MIRD Pamphlet No. 21: A Generalized Schema for Radiopharmaceutical Dosimetry – Standardization of Nomenclature. *J Nucl Med, 50*(3), 477–484.

[68] Decreto-Lei nº 108/2018 de 3 de dezembro da Presidência do Conselho de Ministros. Diário da República, I serie, nº 232. (2018). Last access: November 2020. Available at www.dre.pt.

[69] Botta, F., Mairani, A., Hobbs, R. F., Vergara Gil, A., Pacilio, M., Parodi, K., Cremonesi, M., et al. (2013). Use of the FLUKA Monte Carlo code for 3D patient-specific dosimetry on PET-CT and SPECT-CT images. *Physics in medicine and biology*, *58*(22), 8099–8120.

[70] Gosewisch, A., Ilhan, H., Tattenberg, S., Mairani, A., Parodi, K., Brosch, J., et al. (2019). 3D Monte Carlo bone marrow dosimetry for Lu-177-PSMA therapy with guidance of non-invasive 3D localization of active bone marrow via Tc-99m-anti-granulocyte antibody SPECT/CT. *EJNMMI research*, *9*(1), 76.

[71] Bolch, W. E., Bouchet, L. G., Robertson, J. S., Wessels, B. W., Siegel, J. A., et al. (1999). MIRD pamphlet No. 17: the dosimetry of nonuniform activity distributions-radionuclide S values at the voxel level. Medical Internal Radiation Dose Committee. *J Nucl Med, 40*(1), 11S–36S.

[72] Sapienza, M. T., & Willegaignon, J. (2019). Radionuclide therapy: current status and prospects for internal dosimetry in individualized therapeutic planning. *Clinics, 74*, e835.

[73] Chauvin, M., Borys, D., Botta, F., Bzowski, P., Dabin, J., Denis-Bacelar, A. M., Desbrée, A., et al. (2020). OpenDose: Open-Access Resource for Nuclear Medicine Dosimetry. *J Nucl Med*, *61*(10), 1514–1519.

[74] Stabin, M. G., Sharkey, R. M., & Siegel, J. A. (2011). RADAR Commentary: Evolution and Current Status of Dosimetry in Nuclear Medicine. *J Nucl Med, 52*(7), 1156–1161.

[75] Nuclear Medicine. (2016). Internal Radiation Dosimetry. Fastest Radiology Insight Engine. [Online] Available at: https://radiologykey.com/internal-radiation-dosimetry/ [*2020, January 5*]. *Radiology Key*.

[76] Scarinci, I., Valente, M., & Pérez, P. (2013). Dose Point Kernel calculation and modelling with nuclear medicine dosimetry purposes. *Proceedings of Science*.

[77] Koustou, T., Papadimitroulas, P., Loudos, G., & Kagadis, G. C. (2016). A preclinical simulated dataset of S-values and investigation of the impact of rescaled organ masses using the MOBY phantom. *Physics in Medicine and Biology, 61*(6), 2333–2355.

[78] Huizing, D., de Wit-van der Veen, B.J., Verheij, M. et al. (2018). Dosimetry methods and clinical applications in peptide receptor radionuclide therapy for neuroendocrine tumours: a literature review. *EJNMMI Res, 8*(1), 89.

[79] Nelson, W.R., Hirayama, H., & Rogers, D. (1985). Technical Report: EGS4 code system. Stanford Linear Accelerator Center report SLAC-265.

[80] Brown, F.B. (2003). MCNP - a general Monte Carlo N-particle transport code. v.5. LA-UR03-1987. Los Alamos National Laboratory.

[81] Sempau, J., et al. (1997). An algorithm for Monte Carlo simulation of coupled electron photon transport. Nuclear Instruments and Methods in Physics Research Section B: *Beam Interactions with Materials and Atoms*, *132*(3), 377-390.

[82] Agostinelli, S., Allison, J., Amako, K., Apostolakis, J., et al. (2003). Geant4 - a simulation toolkit. *Nuclear Instruments and Methods in Physics Research Section A: Accelerators, Spectrometers, Detectors and Associated Equipment*, *506*(3), 250-303.

[83] Akagi, T., Aso, T., Faddegon, B., Kimura, A., Matsufuji, N., Nishio, T., et al. (2011). The PTSim and TOPAS Projects, Bringing Geant4 to the Particle Therapy Clinic. *Progress in Nuclear Science and Technology*, *2*, 912-917.

[84] Fahey, F. H., Grogg, K., & El Fakhri, G. (2018). Use of Monte Carlo Techniques in Nuclear Medicine. *Journal of the American College of Radiology, JACR, 15*(3 Pt A), 446–448.

[85] Jan, S., Santin, G., Strul, D., Staelens, S., Assié, K., Autret, D., Avner, S., Barbier, R., et al. (2004). GATE: a simulation toolkit for PET and SPECT. *Physics in medicine and biology*, *49*(19), 4543–4561.

[86] Perl, J., Shin, J., Schümann, J., Faddegon, B., & Paganetti, H. (2012). TOPAS: An innovative proton Monte Carlo platform for research and clinical applications. Medical Physics, *39*(11), 6818–6837.

[87] Arce, P., Rato, P., Canadas, M., & Lagares, J. I. (2008). GAMOS: A Geant4-based easy and flexible framework for nuclear medicine applications. IEEE Nuclear Science Symposium Conference Record.

[88] Stabin, M. G., Sparks, R. B. & Crowe, E. (2005). OLINDA/EXM: the second-generation personal computer software for internal dose assessment in nuclear medicine. *J Nucl Med*. *46*(6), 1023–1027.

[89] Gillam, J. E., & Rafecas, M. (2016). Monte-Carlo simulations and image reconstruction for novel imaging scenarios in emission tomography. *Nuclear Instruments and Methods in Physics Research Section A: Accelerators, Spectrometers, Detectors and Associated Equipment, 809*, 76–88.

[90] Faddegon, B., Ramos-Méndez, J., Schuemann, J., McNamara, A., Shin, J., Perl, J., & Paganetti, H. (2020). The TOPAS tool for particle simulation, a Monte Carlo simulation tool for physics, biology and clinical research. *Physica Medica, 72*, 114–121.

[91] Lee, M. S., Kim, J. H., Paeng, J. C., Kang, K. W., Jeong, J. M., Lee, D. S., & Lee, J. S. (2017). Whole-Body Voxel-Based Personalized Dosimetry: The Multiple Voxel S-Value

Approach for Heterogeneous Media with Nonuniform Activity Distributions. *J Nucl Med, 59*(7), 1133–1139.

[92] Grimes, J., & Celler, A. (2014). Comparison of internal estimates using organ-level, voxel S value, and Monte Carlo techniques. *Med. Phys*, 41(9).

[93] Pacilio, M., Amato, E., Lanconelli, N., Basile, C., Torres, L. A., Botta, F., et al. (2015). Differences in 3D dose distributions due to calculation method of voxel S-values and the influence of image blurring in SPECT. *Phys. Med. Biol., 60*(5), 1945–1964.

[94] Lanconelli, N., Pacilio, M., Lo Meo, S., et al. (2012). A free database of radionuclide voxel S-values for the dosimetry of nonuniform activity distributions. *Phys. Med. Biol, 57*(2), 517–533.

[95] Gonzalez, J., Calderón, C., & Rodriguez, M. (2007). Determination of Radionuclide "S" values for any Voxel size, based on three-dimensional discrete Fourier Transform Convolution Method. *World Journal of Nuclear Medicine*, *6*(1), 40–44.

[96] Franquiz, J. M., Chigurupati, S., & Kandagatla, K. (2003). Beta voxel S-values for internal emitter dosimetry. *Medical Physics*, *30*(6), 1030–1032.

[97] Forrer, F., Krenning, E. P., Kooij, P. P., Bernard, B. F., Konijnenberg, M., Bakker, et al. (2009). Bone marrow dosimetry in peptide receptor radionuclide therapy with [177Lu-DOTA(0),Tyr(3)]octreotate. *EJNMMI*, *36*(7), 1138–1146.

[98] Svensson, J., Rydén, T., Hagmarker, L., Hemmingsson, J., Wängberg, B., & Bernhardt, P. (2016). A novel planar image-based method for bone marrow dosimetry in (177)Lu-DOTATATE treatment correlates with haematological toxicity. *EJNMMI physics*, *3*(1), 21.

[99] Eberlein, U., Cremonesi, M., & Lassmann, M. (2017). Individualized Dosimetry for Theranostics: Necessary, Nice to Have, or Counterproductive? *J Nucl Med, 58*(Supplement 2), 97S–103S.

[100] Gupta, S. K., Singla, S., Thakral, P., & Bal, C. S. (2013). Dosimetric analyses of kidneys, liver, spleen, pituitary gland, and neuroendocrine tumors of patients treated with ^{177}Lu-DOTATATE. *Clinical nuclear medicine*, *38*(3), 188–194.

[101] Sandström, M., Garske-Román, U., Granberg, D., Johansson, S., Widström, C., et al. (2013). Individualized dosimetry of kidney and bone marrow in patients undergoing 177Lu-DOTA-octreotate treatment. *J Nucl Med, 54*(1), 33–41.

[102] Sanders, J. C., Kuwert, T., Hornegger, J., & Ritt, P. (2015). Quantitative SPECT/CT Imaging of (177)Lu with In Vivo Validation in Patients Undergoing Peptide Receptor Radionuclide Therapy. *Molecular imaging and biology*, *17*(4), 585–593.

[103] Beauregard, J. M., Jackson, P., Hofman, M., & Hicks, R. (2013). Bone marrow dosimetry assessment with serial whole-body quantitative SPECT/CT in patients undergoing 177Lu-octreotate PRRT for neuroendocrine tumor. *J Nucl Med*, *54*(2), 582.

[104] Marin, G., Vanderlinden, B., Karfis, I., Guiot, T., Wimana, Z., Reynaert, N., et al. (2018). A dosimetry procedure for organs-at-risk in ^{177}Lu peptide receptor radionuclide therapy of patients with neuroendocrine tumours. *Physica Medica, 56,* 41–49.

[105] Hidayati, N.R., Poon, A., Willowson, K., Eslick, E., Ryu, H., & Bailey, D. L. (2019). Evaluation of Kidney Dose in Neuroendocrine Tumors Patients after Peptide Receptor Radionuclide Therapy using ^{177}Lu-DOTATATE. *Atom Indonesia*, *45*(39), 147-152.

[106] Garske-Román, U., Sandström, M., Fröss Baron, K., Lundin, L., Hellman, P., et al. (2018). Prospective observational study of ^{177}Lu-DOTA-octreotate therapy in 200 patients with advanced metastasized neuroendocrine tumours (NETs): feasibility and impact of a dosimetry-guided study protocol on outcome and toxicity. *EJNMMI*, *45*(6), 970–988.

[107] Sundlöv, A., Sjögreen-Gleisner, K., Svensson, J., Ljungberg, M., Olsson, T., Bernhardt, P., & Tennvall, J. (2017). Individualised ^{177}Lu-DOTATATE treatment of neuroendocrine tumours based on kidney dosimetry. *EJNMMI*, *44*(9), 1480–1489.

[108] Roth, D., Gustafsson, J., Sundlöv, A., & Sjögreen Gleisner, K. (2018). A method for tumour dosimetry based on hybrid planar-SPECT/CT images and semi-automatic segmentation. *Medical Physics*, *45*(11), 5004-5018.

[109] Cremonesi, M., Ferrari, M. E., Bodei, L., Chiesa, C., Sarnelli, A., Garibaldi, C., et al. (2018). Correlation of dose with toxicity and tumour response to ^{90}Y- and ^{177}Lu-PRRT provides the basis for optimization through individualized treatment planning. *EJNMMI*, *45*(13), 2426–2441.

[110] Shen, J. (2021). Tools for NIfTI and ANALYZE image. [Online] Available at: www.mathworks.com/matlabcentral/fileexchange/8797-tools-for-nifti-and-analyze-image [*2021, April 30*]. *MATLAB Central File Exchange*.

[111] Guy, M. J., Flux, G. D., Flower, M. A., Ott, R. J., Papavasileiou, P., & Chittenden, S. J. (2000). Practical scatter-independent gamma camera dead-time correction for iodine-131. *2000 IEEE Nucl Sci Symp. Conf Rec* (Cat. No.00CH37149), *3*, 52 – 56.

[112] Silosky, M., Johnson, V., Beasley, C., & Kappadath, S. C. (2013). Characterization of the count rate performance of modern gamma cameras. *Medical physics*, *40*(3), 032502.

[113] Sorenson, J. (1975). Deadtime characteristics of Anger cameras. *J Nucl Med.*, *16*(4), 284–288.

[114] Heemskerk, J., & Defrise, M. (2020). Gamma detector dead time correction using Lambert W function. *EJNMMI physics*, *7*(1), 27.

[115] Lassmann, M., Chiesa, C., Flux, G., Bardiès, M., & EANM Dosimetry Committee (2011). EANM Dosimetry Committee guidance document: good practice of clinical dosimetry reporting. *EJNMMI*, *38*(1), 192–200.

[116] Geant4. SetCuts: conversion from range to kinetic energy. [Online] Available at: https://geant4.web.cern.ch/sites/geant4.web.cern.ch/files/geant4/collaboration/working_groups/electromagnetic/gallery/cutinrange/doc/setcuts.html [*2021, July 20*]. *Conseil Européen pour la Recherche Nucléaire*.

[117] Capogni, M., Lo Meo, S., & Fazio, A. (2010). Simulation of radioactive decay in GEANT Monte Carlo codes: Comparison between spectra and efficiencies computed with *sch2for* and *G4RadioactiveDecay*. *Applied Radiation and Isotopes*, *68*(7-8), 1428–1432.

[118] White, D. R., Booz, J., Griffith, R. V., Spokas, J. J., & Wilson, I. J. (1989). Report 44. *Journal of the International Commission on Radiation Units and Measurements*, *23*(1).

[119] Chetty, I. J., Rosu, M., Kessler, M. L., Fraass, B. A., Ten Haken, R. K., et al. (2006). Reporting and analyzing statistical uncertainties in Monte Carlo-based treatment planning. *International journal of radiation oncology, biology, physics*, *65*(4), 1249–1259.

[120] Gustafsson, J., Brolin, G., Cox, M., Ljungberg, M., Johansson, L., & Gleisner, K. S. (2015). Uncertainty propagation for SPECT/CT-based renal dosimetry in (177)Lu peptide receptor radionuclide therapy. *Phys Med Biol*, *60*(21), 8329–8346.

[121] Guerriero, F., Ferrari, M. E., Botta, F., Fioroni, F., Grassi, E., Versari, A., et al. (2013). Kidney dosimetry in ^{177}Lu and ^{90}Y peptide receptor radionuclide therapy: influence of image timing, time-activity integration method, and risk factors. *BioMed research international*, *2013*, 935351.

[122] Schneider, W., Bortfeld, T., & Schlegel, W. (2000). Correlation between CT numbers and tissue parameters needed for Monte Carlo simulations of clinical dose distributions. *Phys. Med. Biol*, *45*(2), 459–478.

[123] Salarian, A. (2021). Intraclass Correlation Coefficient (ICC). [Online] Available at: www.mathworks.com/matlabcentral/fileexchange/22099-intraclass-correlation-coefficient-icc [*2021, April 30th*]. *MATLAB Central File Exchange*.

[124] Desy, A., Bouvet, G. F., Frezza, A., Després, P., & Beauregard, J. M. (2020). Impact of dead time on quantitative ^{177}Lu-SPECT (QSPECT) and kidney dosimetry during PRRT. *EJNMMI physics*, *7*(1), 32.

[125] Levart, D., Kalogianni, E., Corcoran, B., Mulholland, N., & Vivian, G. (2019). Radiation precautions for inpatient and outpatient ^{177}Lu-DOTATATE peptide receptor radionuclide therapy of neuroendocrine tumours. *EJNMMI physics*, *6*(1), 7.

[126] Abuqbeitah, M., Demir, M., Uslu-Beşli, L., Yeyin, N., & Sönmezoğlu, K. (2017). Blood clearance and occupational exposure for ^{177}Lu-DOTATATE compared to ^{177}Lu-PSMA radionuclide therapy. *Radiation and Environmental Biophysics*, *57*(1), 55–61.

[127] Wehrmann, C., Senftleben, S., Zachert, C., Müller, D., & Baum, R. P. (2007). Results of Individual Patient Dosimetry in Peptide Receptor Radionuclide Therapy with ^{177}Lu DOTA-TATE and ^{177}Lu DOTA-NOC. *Cancer Biotherapy and Radiopharmaceuticals*, *22*(3), 406–416.

[128] Brolin, G., Gustafsson, J., Ljungberg, M., & Gleisner, K. S. (2015). Pharmacokinetic digital phantoms for accuracy assessment of image-based dosimetry in (177)Lu-DOTATATE peptide receptor radionuclide therapy. *Phys Med Biol*, *60*(15), 6131–6149.

[129] Gospavic, R., Knoll, P., Mirzaei, S., & Popov, V. (2016). Physiologically Based Pharmacokinetic (PBPK) Model for Biodistribution of Radiolabeled Peptides in Patients with Neuroendocrine Tumours. *Asia Oceania J Nucl Med Biol*, *4*(2), 90–97.

[130] Hänscheid, H., Lapa, C., Buck, A. K., Lassmann, M., & Werner, R. A. (2018). Dose Mapping After Endoradiotherapy with ^{177}Lu-DOTATATE/DOTATOC by a Single Measurement After 4 Days. *J Nucl Med*, *59*(1), 75–81.

[131] Maria, A., & Maria, L. (2019). Monte Carlo Simulation in Radionuclide Therapy Dosimetry. *Biomed J Sci & Tech Res*, *15*(1), 11102–11107.

[132] ICRU Report 10b. (1964). Physical Aspects of Radiation. *Journal of the International Commission on Radiation Units and Measurements*, *6*(1).

[133] Yoriyaz, H., Moralles, M., Siqueira, P., Guimarães, C., Cintra, F. B., & dos Santos, A. (2009). Physical models, cross sections, and numerical approximations used in MCNP and GEANT4 Monte Carlo codes for photon and electron absorbed fraction calculation. *Medical physics*, *36*(11), 5198–5213.

[134] Mikell, J. (2015). Voxel-Level Absorbed Dose Calculations with A Deterministic Grid-Based Boltzmann Solver for Nuclear Medicine and The Clinical Value of Voxel-Level Calculations. [PhD Thesis, The University of Texas].

[135] Lai, P., Cai, Z., Pignol, J. P., Lechtman, E., Mashouf, S., Lu, Y., Winnik, M. A., et al. (2017). Monte Carlo simulation of radiation transport and dose deposition from locally released gold nanoparticles labeled with ^{111}In, ^{177}Lu or ^{90}Y incorporated into tissue implantable depots. *Phys Med Biol*, *62*(22), 8581–8599.

[136] Amato, E., Auditore, L., Italiano, A., Pistone, D., Arce, P., Campenni, A., & Baldari, S. (2020). Full Monte Carlo internal dosimetry in nuclear medicine by means of GAMOS. *Journal of Physics: Conference Series*, *1561*, 012002.

[137] Pistone, D., Auditore, L., Italiano, A., Mandaglio, G., Minutoli, F., Baldari, S., & Amato, E. (2020). Monte Carlo Based Dose-Rate Assessment In ^{18}F-Choline Pet Examination: A Comparison Between Gate and Gamos Codes. *Atti Accad. Pelorit. Pericol. Cl. Sci. Fis. Mat. Nat.*, *98*(1), A5.

[138] Graves, S., Tiwari, A., Kruzer, A., Nelson, A., Mirando, D., Dewaraja, Y., & Sunderland, J. (2020). Monte Carlo validation of convolution-based voxelwise dosimetry. *J Nucl Med*, *61* (supplement 1), 1019.

[139] Marcatili, S., Villoing, D., Mauxion, T., McParland, B. J., & Bardiès, M. (2015). Model-based versus specific dosimetry in diagnostic context: Comparison of three dosimetric approaches. *Medical Physics*, *42*(3), 1288–1296.

[140] Götz, T., Schmidkonz, C., Lang, E. W., Maier, A., Kuwert, T., & Ritt, P. (2019). A comparison of methods for adapting ^{177}Lu dose-voxel-kernels to tissue inhomogeneities. *Phys. Med. Biol.*, *64*(24), 245011.

[141] Thakral, P., Sen, I., Pant, V., Gupta, S. K., Dureja, S., Kumari, J., et al. (2018). Dosimetric analysis of patients with gastro entero pancreatic neuroendocrine tumors (NETs) treated with PRCRT (peptide receptor chemo radionuclide therapy) using Lu-177 DOTATATE and capecitabine/temozolomide (CAP/TEM). *The British journal of radiology*, *91*(1091), 20170172.

[142] Sarikaya, I., Sarikaya, A., Alnafisi, N., & Alenezi, S. (2018). Significance of splenic uptake on somatostatin receptor imaging studies. *Nuclear medicine review. Central & Eastern Europe*, *21*(1), 66–70.

[143] Santoro, L., Mora-Ramirez, E., Trauchessec, D., Chouaf, S., Eustache, P., Pouget, J. P., et al. (2018). Implementation of patient dosimetry in the clinical practice after targeted radiotherapy using [^{177}Lu-[DOTA0, Tyr3]-octreotate. *EJNMMI research*, *8*(1), 103.

[144] Garske, U., Sandström, M., Johansson, S., Sundin, A., Granberg, D., Eriksson, B., & Lundqvist, H. (2012). Minor changes in effective half-life during fractionated 177Lu-octreotate therapy. *Acta oncologica*, *51*(1), 86–96.

[145] Schuchardt, C., Kulkarni, H. R., Prasad, V., Zachert, C., Müller, D., & Baum, R. P. (2012). The Bad Berka Dose Protocol: Comparative Results of Dosimetry in Peptide Receptor Radionuclide Therapy Using ^{177}Lu-DOTATATE, ^{177}Lu-DOTANOC, and ^{177}Lu-DOTATOC. *Theranostics, Gallium-68, and Other Radionuclides*, 519–536.

[146] Abreu, M. C., Matias, L., Peralta, L. F. (1994). Física Experimental: Uma introdução. 1st Edition. Leituras 1 – Aquisição, Análise e Tratamento de Dados, pp. 114 – 117.

Appendix

A. EANM'20 Congress Abstract

^{177}Lu-DOTATATE Quantification for Patient Personalised Dosimetry in Therapy of Neuroendocrine Tumours

C. Rodrigues[1,2,3], P. Ferreira[1], F. P. M. Oliveira[1], Â. Silva[1], L. Peralta[2,3], D. C. Costa[1]

[1] Champalimaud Centre for the Unknown, Champalimaud Foundation, Lisbon, PORTUGAL

[2] Faculdade de Ciências, Universidade de Lisboa, Lisbon, PORTUGAL

[3] Laboratório de Instrumentação e Física Experimental de Partículas, Lisbon, PORTUGAL

Introduction: Peptide Radionuclide Radiotherapy (PRRT) with ^{177}Lu-DOTATATE is a nuclear medicine therapeutic option with increasing interest over the last few years due to its efficacy in the treatment of metastatic and/or inoperable neuroendocrine tumors overexpressing somatostatin receptors. Toxicity may represent a limitation of this therapy. The evaluation of absorbed dose, besides being required by law, is an essential tool for the improvement of treatment plans. Thereby, the present study investigates the average dose absorbed by the liver, kidneys, spleen and bone marrow, for further customization of future treatments. **Materials and Methods:** From August 2017 to March 2019, 4 patients, treated with 7.4±0.3 GBq of ^{177}Lu-DOTATATE per treatment cycle (four cycles/patient), accepted to undertake whole-body planar images, single photon emission computed tomography (SPECT) and X-ray computerized tomography (CT) images of the abdomen, at specific time points (1h, 4h, 24h and 120h), after radiopharmaceutical administration. The data from the patients were retrospectively selected from the database of our institution. After processing, structural images were used to perform manual segmentation of the volume for all organs of interest. For each organ, the radiopharmaceutical kinetic distribution was analysed, the voxel-wise absorbed dose distribution was determined based on SPECT activity images, and the organ toxicity was assessed. **Results:** After completion of the four treatment cycles, the mean absorbed dose, for the 4 patients investigated, was as follows: liver 22±22 Gy; right kidney 20.3±8.6 Gy; left kidney 18±12 Gy; spleen 21.7±6.5 Gy and bone marrow 4.7±5.7 Gy. Additionally, we observed that approximately half of the mean absorbed dose on each cycle has occurred within the first five days after the radiopharmaceutical's administration. **Conclusion:** The mean absorbed doses in the kidneys, after all four therapy cycles, are below the established limits. On the other hand, the average value of the mean absorbed dose by the bone marrow is higher than expected. This indicates that, in an overall analysis, the administered activity could have been altered, not in an attempt to optimize treatment effectiveness, but rather to improve bone marrow toxicity. Despite the reduced number of patients investigated, so far, our results are in agreement with the values presented by others. Ongoing work is designed to measure the absorbed dose by tumour lesions, and to optimize a protocol to implement personalized therapeutic medicine in patients with metastatic neuroendocrine tumours.

B. EANM'21 Congress Abstract

Comparison of Voxel S-values and Monte Carlo Simulation in [^{177}Lu]Lu-DOTA-TATE Quantification for Patient-Specific Dosimetry

C. Rodrigues[1,2,3], P. Ferreira[1], F. P. M. Oliveira[1], Â. Silva[1], L. Peralta[2,3], D. C. Costa[1]

[1] Champalimaud Centre for the Unknown, Champalimaud Foundation, Lisbon, PORTUGAL

[2] Faculdade de Ciências, Universidade de Lisboa, Lisbon, PORTUGAL

[3] Laboratório de Instrumentação e Física Experimental de Partículas, Lisbon, PORTUGAL

Introduction: Peptide receptor radionuclide therapy (PRRT) with [^{177}Lu]Lu-DOTA-TATE is remarkably effective in the treatment of neuroendocrine tumours (NETs) over-expressing somatostatin receptors. Apart from potential renal and/or haematological toxicity, the significant absorbed dose variability among patients requires individual treatment optimisation. Several methods have been used to quantify tissue exposure. This study compares the dosimetry calculated by two computational methods on a retrospective analysis of [^{177}Lu]Lu-DOTA-TATE PRRT clinical cases. **Methods:** Twenty-four treatments from 6 patients with histologically confirmed inoperable and/or metastatic neuroendocrine neoplasia over-expressing somatostatin receptors were retrospectively analysed (4 cycles/patient). A mean activity of 7.2 ± 0.5 GBq/cycle of [^{177}Lu]Lu-DOTA-TATE was administered. For 5 patients, two abdominal SPECT and CT acquisitions (24h and 120h post administration) were performed. For the other patient only one acquisition was performed (24h post administration). These acquisitions were used for absorbed dose quantification based on two methods. Voxel-based dosimetry with pre-calculated voxel S-values (VSV) was performed with an in-house program. Monte Carlo (MC) based dosimetry, with 100 million events, was performed with TOPAS (Geant4) tool. Organ 3D absorbed dose maps were qualitatively compared using dose-volume histograms (DVHs) and mean absorbed doses were quantitatively compared using the intraclass correlation coefficient (ICC) and relative difference (RD), with respect to MC. **Results:** MC based dosimetry entailed a simulation time of around 40 hours/simulation while the VSV method took less than 1 minute/computation, in the same workstation. Very good agreement (ICC > 0.90) was found for organ absorbed dose maps obtained with the two methods, with similar dose distribution given by the DVHs. Mean absorbed dose in the liver, right kidney, left kidney, spleen, bone marrow and NETs showed an ICC of 1.000, 0.992, 0.998, 0.999, 0.999 and 0.999, respectively. The greatest median RD of -3.6% (min = -25.6, max = 3.8) was seen for the bone marrow. Liver, right kidney, left kidney, spleen and NETs presented median RD of -1.0% (-5.5, 0.7), -2.9% (-11.1, 2.6), -1.9% (-15.4, 1.7), 0.2% (-4.3, 4.1) and 0.4% (-10.3, 8.2), respectively. These differences are most likely due to patient morphology considerations in MC simulations. **Conclusion:** This preliminary study reveals similar 3D absorbed dose maps for both VSV and MC methods, with slightly lower VSV than MC dose values. Therefore, the VSV-based method appears to be a reasonable choice for clinical dosimetry calculations in [^{177}Lu]Lu-DOTA-TATE PRRT patients, considering the significantly short computation time and dosimetry accuracy.

C. Dead Time Constant Error Propagation

In order to determine the dead time constant of the imaging system, the graphical approach described in [49] was used. Assuming that the system has a paralyzable behavior and that the true count rate has an exponential decline over time (i.e., decaying source method), a linear model ($y = mx + b$) was fitted to the data to obtain $\ln(R_{obs}) + \lambda t$ (i.e., ordinate) versus $e^{-\lambda t}$ (i.e., abscissa) (Figure C.1), from which $m = -R^0_{true}\tau_p$ and $b = \ln(R^0_{true})$ were extrapolated.

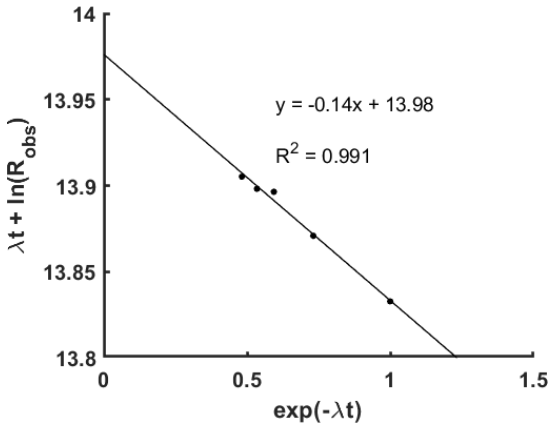

Figure C.1. Linear model fitted to the data according to the graphical method described in [49] to estimate the dead time constant of the imaging system (i.e., decaying source method applied to a paralyzable system).

The standard error (SE) of the coefficients of the linear model was extrapolated from the total least squares algorithm, as described in [146]. Considering Equation (4.4), the dead time constant error was estimated according to

$$\Delta\tau = \sqrt{\left(\frac{\partial\tau}{\partial m}\Delta m\right)^2 + \left(\frac{\partial\tau}{\partial b}\Delta b\right)^2} = \sqrt{\left(-\frac{\Delta m}{e^b}\right)^2 + \left(\frac{m}{e^b}\Delta b\right)^2} = \tau\sqrt{\Delta b^2 + \left(\frac{\Delta m}{m}\right)^2} \qquad \text{(C.1)}$$

where Δm and Δb are the standard error of the fit parameters. Note that the uncertainty of each point was not included in the calculation since it was not available. Thus, the estimated dead time uncertainty is only related with the statistical fluctuations of the data. Nonetheless, it will be at least of the order of magnitude of the determined value.

D. Tracer Kinetics

In this section, additional results concerning the biokinetic analysis performed in this work are made available. The tracer kinetics in the liver, kidneys, spleen and NETs for patients #4 and #6 is presented below. The 3rd cycle of patient #6 is not shown as only two planar imaging acquisitions was performed.

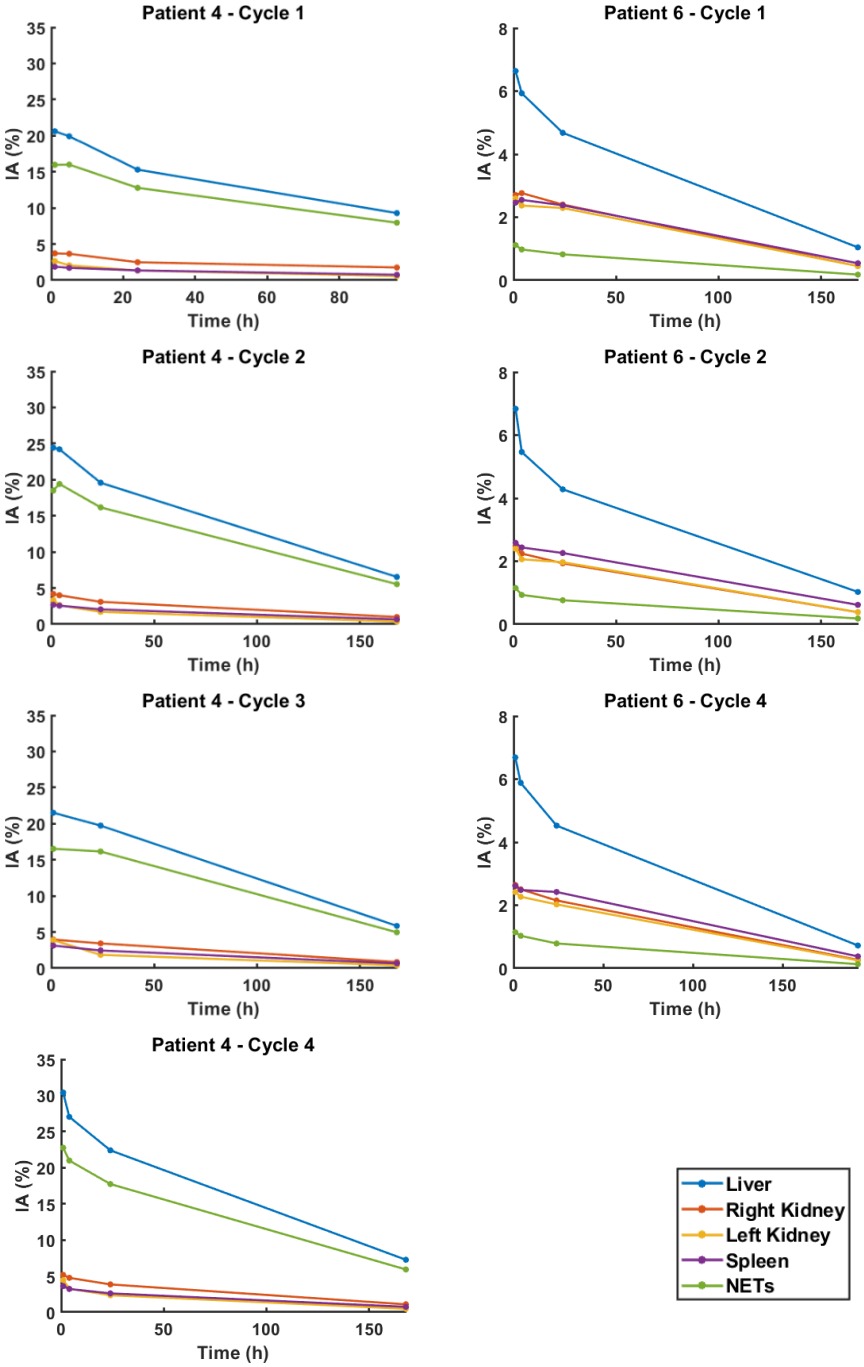

Figure D.1. Time-activity data for the liver, kidneys, spleen and NETs of patients #4 and #6. The lines are for guidance purposes only as no fit to the data is presented. The uptake phase is not clear in all curves due to the absence of quantitative information in the first hour PI. The data were fitted to a mono- or bi-exponential function to determine the tracer's effective half-life in each VOI. Please note the different scales of injected activity and time.

The table presented below exhibits the ^{177}Lu-DOTATATE effective half-life values in organs and NETs estimated by other research groups, which were used to validate the data determined in this work.

Table D.1. Comparison of organ and tumor ^{177}Lu-DOTATATE effective half-life estimates with published data.

Study	Sample Size (# Patients)	Protocol	VOI	Median (h) [range]	Mean ± SD (h)
Present Study	N = 5	Three/four sequential WB scans Bi- or mono-exponential fit	Liver	69.9 [22.9– 152.6]	79.6 ± 31.5
			R Kidney	63.4 [28.2 – 252.5]	81.9 ± 50.2
			L Kidney	62.0 [22 – 170.2]	67.7 ± 33.7
			Spleen	78.5 [47.9 – 167.9]	80.8 ± 25.9
			NETs	79.7 [49.4 – 184.8]	88.4 ± 33.4
Marin et al. [22]	N = 47	Three sequential SPECT/CT scans Bi-exponential fit	Liver*	79 [29 – 129]	---
			Kidneys*	55 [22 – 99]	---
			Spleen*	71 [24 – 114]	---
Hanscheid et al. [130]	N = 22	Single WB scan Bi- or mono-exponential fit	Liver*	67 [55 – 117]	---
			Kidneys*	51 [40 – 68]	---
			Spleen*	68 [52 – 99]	---
			NETs*	77 [56 – 130]	---
Wehrmann et al. [127]	N = 69	Five serial planar WB scans Mono-exponential fit	Kidneys	---	63.3 ± 17.5
			Spleen	---	70.2 ± 16.9
			NETs	---	75.5 ± 20.9

* Data was published as median and range only. No information regarding mean values was available.

E. Additional Dosimetry Results

In this section, additional dosimetry results and raw data are presented. The tables below show the individual organ and NETs mean absorbed dose values, normalized to the injected activity, obtained by VSV dosimetry (Table E.1) and TOPAS-MC simulations (Table E.2) using post-therapeutic ^{177}Lu-DOTATATE SPECT scans.

Table E.1. Normalized individual (n = 6 patients) and global mean absorbed dose (Gy/GBq) in the liver, kidneys, spleen, bone marrow and NETs estimated from post-therapeutic ^{177}Lu-DOTATATE SPECT scans using VSVs. Values are presented as mean ± SD [range].

Patient ID	VSV Absorbed Dose Coefficients (Gy/GBq)					
	Liver	**Right Kidney**	**Left Kidney**	**Spleen**	**Bone Marrow**	**NETs**
1	0.137 ± 0.011 [0.126 – 0.151]	0.399 ± 0.053 [0.333 – 0.463]	0.435 ± 0.071 [0.345 – 0.517]	0.702 ± 0.069 [0.614 – 0.782]	0.038 ± 0.004 [0.033 – 0.043]	0.263 ± 0.129 [0.120 – 0.422]
2	2.109 ± 0.269 [1.921 – 2.507]	0.696 ± 0.192 [0.569 – 0.979]	0.198 ± 0.065 [0.149 – 0.294]	0.572 ± 0.306 [0.310 – 1.013]	0.536 ± 0.057 [0.459 – 0.597]	5.169 ± 0.798 [4.735 – 6.366]
3	0.223 ± 0.061 [0.152– 0.285]	0.543 ± 0.159 [0.326 – 0.682]	0.522 ± 0.159 [0.309 – 0.651]	0.629 ± 0.171 [0.392 – 0.790]	0.041 ± 0.011 [0.027 – 0.053]	2.135 ± 0.779 [1.489 – 3.151]
4	0.739 ± 0.042 [0.688– 0.791]	0.417 ± 0.036 [0.368 – 0.453]	0.342 ± 0.035 [0.290 – 0.370]	0.419 ± 0.094 [0.287 – 0.503]	0.037 ± 0.007 [0.030 – 0.044]	1.264 ± 0.053 [1.193 – 1.136]
5	0.656 ± 0.128 [0.527– 0.811]	0.878 ± 0.068 [0.841 – 0.980]	0.902 ± 0.148 [0.778 – 1.116]	0.813 ± 0.108 [0.708 – 0.963]	0.079 ± 0.006 [0.075 – 0.087]	3.208 ± 0.529 [2.801 – 3.961]
6	0.319 ± 0.143 [0.227– 0.532]	0.728 ± 0.282 [0.508 – 1.141]	0.679 ± 0.236 [0.455 – 1.011]	0.936 ± 0.247 [0.692 – 1.241]	0.107 ± 0.067 [0.047 – 0.203]	0.320 ± 0.141 [0.207 – 0.525]
	0.697 ± 0.693 [0.126 – 2.507]	0.610 ± 0.225 [0.326 – 1.141]	0.513 ± 0.263 [0.148 – 1.116]	0.678 ± 0.237 [0.287 – 1.241]	0.140 ± 0.186 [0.027 – 0.597]	2.060 ± 1.820 [0.120 – 6.366]

Table E.2. Normalized individual (n = 6 patients) and global mean absorbed dose (Gy/GBq) in the liver, kidneys, spleen, bone marrow and NETs estimated from post-therapeutic ^{177}Lu-DOTATATE SPECT scans using TOPAS-MC simulations. Values are presented as mean ± SD [range].

Patient ID	MC Absorbed Dose Coefficients (Gy/GBq)					
	Liver	**Right Kidney**	**Left Kidney**	**Spleen**	**Bone Marrow**	**NETs**
1	0.144 ± 0.012 [0.133 – 0.160]	0.407 ± 0.050 [0.344 – 0.467]	0.445 ± 0.070 [0.355 – 0.526]	0.691 ± 0.077 [0.606 – 0.792]	0.041 ± 0.122 [0.037 – 0.046]	0.272 ± 0.122 [0.134 – 0.416]
2	2.129 ± 0.269 [1.936 – 2.527]	0.749 ± 0.195 [0.632 – 1.039]	0.226 ± 0.071 [0.176 – 0.331]	0.583 ± 0.302 [0.324 – 1.019]	0.531 ± 0.053 [0.461 – 0.588]	5.148 ± 0.800 [4.687 – 6.346]
3	0.226 ± 0.061 [0.154 – 0.285]	0.545 ± 0.159 [0.325 – 0.679]	0.527 ± 0.164 [0.306 – 0.661]	0.622 ± 0.169 [0.389 – 0.781]	0.043 ± 0.012 [0.028 – 0.055]	2.108 ± 0.722 [1.507 – 2.996]
4	0.744 ± 0.042 [0.690 – 0.793]	0.437 ± 0.049 [0.369 – 0.473]	0.350 ± 0.035 [0.298 – 0.375]	0.424 ± 0.097 [0.289 – 0.512]	0.047 ± 0.007 [0.041 – 0.053]	1.244 ± 0.057 [1.166 – 1.288]
5	0.654 ± 0.128 [0.526 – 0.806]	0.891 ± 0.085 [0.824 – 1.015]	0.899 ± 0.168 [0.777 – 1.136]	0.795 ± 0.105 [0.700 – 0.945]	0.082 ± 0.010 [0.073 – 0.097]	3.053 ± 0.437 [2.738 – 3.695]
6	0.326 ± 0.149 [0.229 – 0.548]	0.752 ± 0.295 [0.524 – 1.184]	0.700 ± 0.250 [0.467 – 1.054]	0.935 ± 0.245 [0.695 – 1.239]	0.107 ± 0.068 [0.045 – 0.204]	0.331 ± 0.145 [0.213 – 0.542]
	0.704 ± 0.699 [0.132 – 2.527]	0.630 ± 0.233 [0.325 – 1.184]	0.524 ± 0.261 [0.176 – 1.136]	0.675 ± 0.233 [0.289 – 1.239]	0.142 ± 0.182 [0.028 – 0.588]	2.026 ± 1.789 [0.134 – 6.346]

In the following images, the cDVHs for each VOI of patients #3, #4, #5 and #6 obtained by the two dosimetry methods are presented. VSV and TOPAS-MC show similar absorbed dose distribution in the organs and NETs with almost overlapping curves, which present the expected appearance.

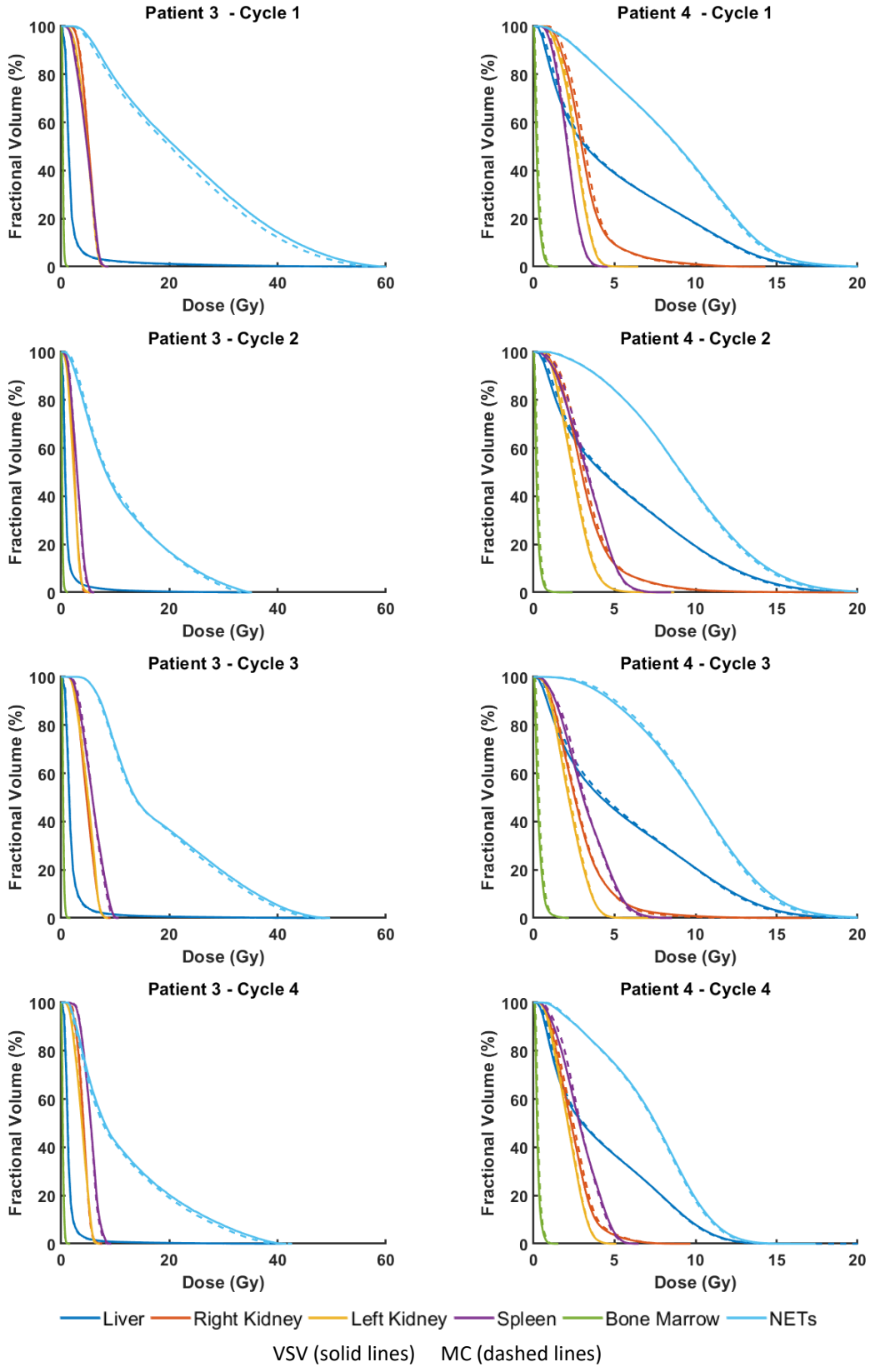

Figure E.1. Cumulative DVHs computed for the liver, right and left kidneys, spleen, bone marrow and NETs by analysis of the voxel-wise absorbed dose distributions obtained with the VSV (solid lines) and MC (dashed lines) methods for patients #3

and #4. The vertical axis represents the fractional volume that received a minimum absorbed dose. For each VOI, cDVHs for the two dosimetry methods are almost identical.

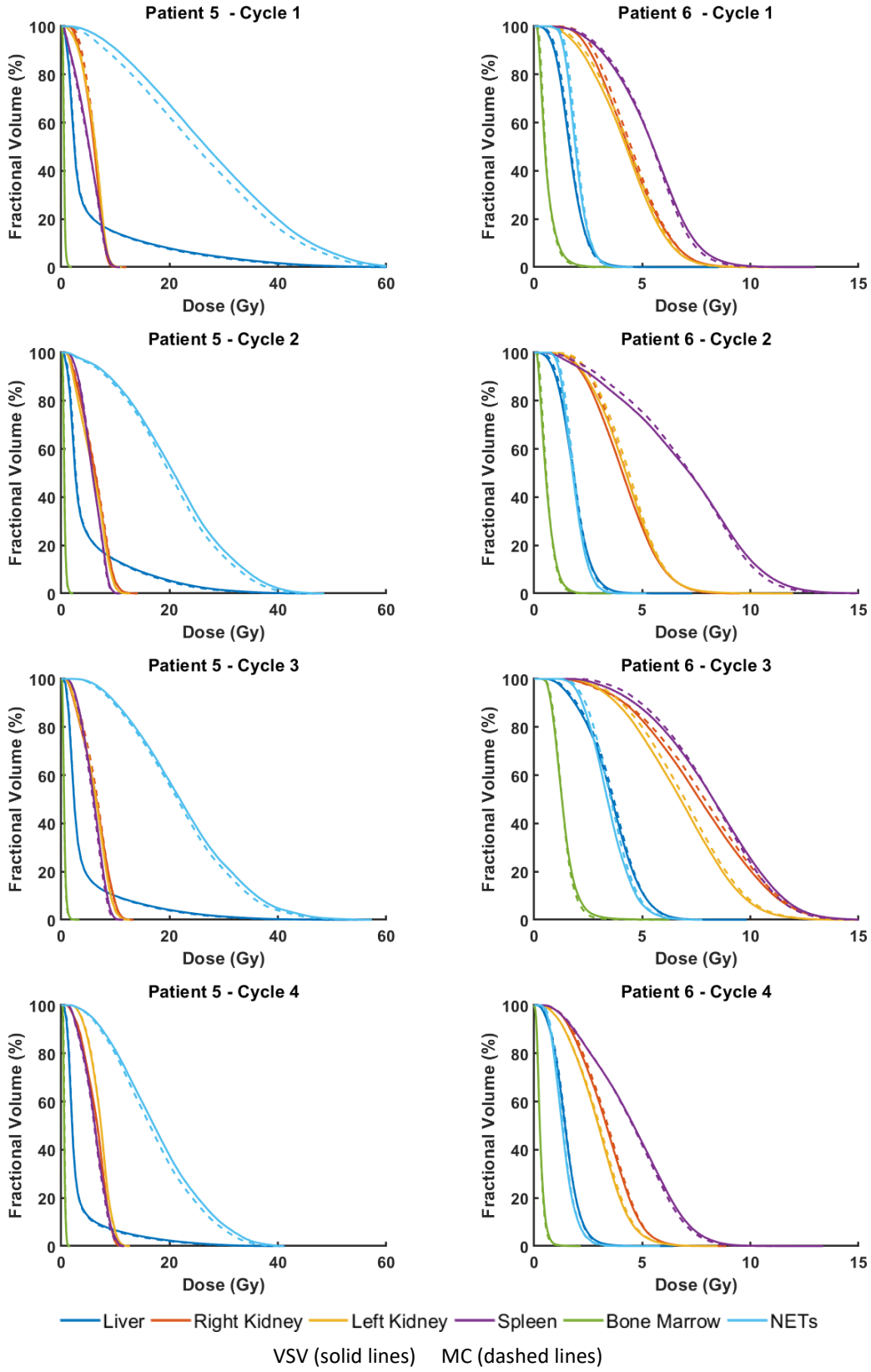

Figure E.2. Cumulative DVHs computed for the liver, right and left kidneys, spleen, bone marrow and NETs by analysis of the voxel-wise absorbed dose distributions obtained with the VSV (solid lines) and MC (dashed lines) methods for patients #5 and #6. The vertical axis represents the fractional volume that received a minimum absorbed dose. For each VOI, cDVHs for the two dosimetry methods are almost identical.